

ABSTRACT

Title of dissertation: IONOSPHERIC TURBULENCE NEAR
THE UPPER HYBRID LAYER:
THEORY AND EXPERIMENT

Amir Christopher Najmi, Doctor of Philosophy, 2016

Dissertation directed by: Professor Dennis Papadopoulos
Department of Physics

The thesis presents experimental results, simulations, and theory on turbulence excited in magnetized plasmas near the ionosphere's upper hybrid layer. The results include:

- The first experimental observations of super small striations (SSS) excited by the High-Frequency Auroral Research Project (HAARP)
- The first detection of high-frequency (HF) waves from the HAARP transmitter over a distance of 16×10^3 km
- The first simulations indicating that upper hybrid (UH) turbulence excites electron Bernstein waves associated with all nearby gyroharmonics
- Simulation results that indicate that the resulting bulk electron heating near the upper hybrid (UH) resonance is caused primarily by electron Bernstein waves parametrically excited near the first gyroharmonic.

On the experimental side we present two sets of experiments performed at the (HAARP) heating facility in Alaska. In the first set of experiments, we present the first detection of super-small (cm scale) striations (SSS) at the HAARP facility. We detected density structures smaller than 30 cm for the first time through a combination of satellite and ground based measurements. In the second set of experiments, we present the results of a novel diagnostic implemented by the Ukrainian Antarctic Station (UAS) in Verdansky. The technique allowed the detection of the HAARP signal at a distance of nearly 16 Mm, and establish that the HAARP signal was injected into the ionospheric waveguide by direct scattering off of dekameter-scale density structures induced by the heater.

On the theoretical side, we present results of Vlasov simulations near the upper hybrid layer. These results are consistent with the bulk heating required by previous work on the theory of the formation of descending artificial ionospheric layers (DAILs), and with the new observations of DAILs at HAARP's upgraded effective radiated power (ERP). The simulations that frequency sweeps, and demonstrate that the heating changes from a bulk heating between gyroharmonics, to a tail acceleration as the pump frequency is swept through the fourth gyroharmonic. These simulations are in good agreement with experiments. We also incorporate test particle simulations that isolate the effects of specific wave modes on heating, and we find important contributions from both electron Bernstein waves and upper hybrid waves, the former of which have not yet been detected by experiments, and have not been previously explored as a driver of heating.

In presenting these results, we analyzed data from HAARP diagnostics and

assisted in planning the second round of experiments. We integrated the data into a picture of experiments that demonstrated the detection of SSS, hysteresis effects in stimulated electromagnetic emission (SEE) features, and the direct scattering of the HF pump into the ionospheric waveguide. We performed simulations and analyzed simulation data to build the understanding of collisionless heating near the upper hybrid layer, and we used these simulations to show that bulk electron heating at the upper hybrid layer is possible, which is required by current theories of DAIL formation. We wrote a test particle simulation to isolate the effects of electron Bernstein waves and upper hybrid waves on collisionless heating, and integrated this code to work with both the output of Vlasov simulations and the input for simulations of DAIL formation.

IONOSPHERIC TURBULENCE NEAR THE UPPER HYBRID
LAYER:
THEORY AND EXPERIMENT

by

Amir Christopher Najmi

Dissertation submitted to the Faculty of the Graduate School of the
University of Maryland, College Park in partial fulfillment
of the requirements for the degree of
Doctor of Philosophy
2016

Advisory Committee:
Professor Dennis Papadopoulos Chair/Advisor
Professor Thomas Antonsen
Professor Roald Sagdeev
Dr. Peter Yoon
Dr. Surja Sharma

© Copyright by
Amir Christopher Najmi
2016

Dedication

To Emma, sharing doors forever.

Acknowledgments

I am deeply thankful for everyone in my life who made my work possible.

Thank you Professor Papadopoulos. You pushed me to work at a high level on interesting problems, and you made me grapple with difficult questions.

Thank you Dr. Surja Sharma. You gave me my first introduction to the UMD SPP group with a project on particle orbit tracing, and I have frequently been pleased to find some parts of that early work pop into something I was working on more recently.

Thank you Dr. Gennady Milikh. When I was not sure what I was interested in, or how I was going to contribute to the group, you brought me in to work on my first experimental project. It has been a pleasure working with you on theory and experimental results from HF heating.

Thank you Dr. Xi Shao. You guided me in tackling my first big problem. When I was treading water you pushed me to teach myself how to swim.

Thank you Dr. Bengt Eliasson. I could not ask for a collaborator who is more knowledgeable and thoughtful both about science, and about presentation. It has been a pleasure working with you.

Thank you to the committee members: Professor Antonsen, Professor Sagdeev, and Dr. Yoon. I am grateful to have such accomplished scientists on my committee, and I am eager to receive your feedback on this dissertation.

Thank you:

My colleagues in the SPP group: Dr. Aram Vartanyan, Dr. Kate Zawdie, and

Erin Lynch.

The wonderful friends I have made at UMD: Ed Behn, Evan Berkowitz, Rangga Budoyo, Andres Cimmarusti, Alex Curtin, Joel Dahlin, Aftaab Dewan, Will Donnelly, David Green, Jeff Grover, Brian Hamilton, John Hoffmann, Anjor Kanekar, Mukul Kulkarni, Eric Kuo, Jessica Lewis, Erin Moody, Josue Morales, Aaron Ostrander, Josh Parker, Lora and Ryan Price, Matt Reed, Matt Severson, Zach Smith, and Kyle Wardlow. I am delighted that I had the chance to get to know you all personally and professionally.

Everyone who has had the patience to live with me while working on this: David and Janet Gers, Robert Hellauer, Patrick Hunt, Michal Krasel, Zach Cummins, Levi DeVries, David Meichle. What a house.

My parents and family: My father Dr. Amir-Homayoon Najmi, my mother Dr. Melinda Johnson, my brothers Jonathan and Jeffrey.

My wife, Emma.

Table of Contents

List of Tables	vii
List of Figures	vii
List of Abbreviations	ix
1 Introduction	1
1.1 Plasma Physics	3
1.2 The Ionosphere	7
1.3 Ionospheric Dynamics and Conductivity	11
1.4 Ionospheric Modification	13
2 Generation of Super Small Striations at HAARP	18
2.1 Overview	18
2.2 Description of Experiment	19
2.3 Experimental Observations	25
2.3.1 Hysteresis Effect	30
2.3.2 Excitation and Relaxation Times	34
2.4 Discussion	35
2.5 Conclusion	39
3 Studies of Ionospheric Turbulence Excited by the Fourth Gyroharmonic	42
3.1 Introduction	42
3.2 Description of Experiments	44
3.3 Experimental Observations	46
3.3.1 GPS Observations	50
3.3.2 SEE Observations	51
3.3.3 Kodiak Radar Observations	52
3.3.4 UAS Signal Observations	53
3.4 Discussion	55
3.5 Conclusions	71

4	Vlasov Simulations Near the Upper Hybrid Layer	76
4.1	Introduction	76
4.2	Simulation Set-up	78
4.3	Results	82
4.4	Off-Resonance Heating	84
4.4.1	Ion Density	84
4.4.2	Electron Heating	84
4.4.3	Observed High-Frequency and Low-Frequency Wave Modes	88
4.4.4	Parametric Decay of Upper Hybrid to Upper Hybrid and Lower Hybrid Waves	96
4.4.5	Parametric Decay of Upper Hybrid to Electron Bernstein and Lower Hybrid Modes	99
4.4.6	Stochastic Heating Mechanism	100
4.4.7	Summary	108
4.5	Resonant Heating	108
4.5.1	Vlasov Simulation	109
4.5.2	Test-Particle Simulation	110
4.5.3	Heating Wave Modes	113
4.5.4	Excitation of Electron Bernstein waves	123
4.5.5	Comparison with Experiments	125
4.5.6	Strong Langmuir Turbulence	128
4.6	Conclusions	129
5	Conclusions	131

List of Tables

2.1	2013-Mar Experiment Overview	24
2.2	BUM DM Excitation Relaxation Times	35
3.1	Beam Angles Jun 2014	46
4.1	Vlasov Simulation Parameters	83
4.2	Upper Hybrid Wavenumber and Wavelengths	100
4.3	Daughter Upper Hybrid Wavenumber and Wavelength	101
4.4	Double Decay Daughter Wavenumber and Wavelength	101

List of Figures

1.1	Ionospheric Profiles	10
2.1	Heater Contours and Satellite Path	21
2.2	HAARP Frequency Sweep	22
2.3	STEC Mar 2013	26
2.4	SEE Spectrogram Mar 2013	28
2.5	SEE/STEC Correlation	29
2.6	Ionograms Mar 2013	31
2.7	MUIR Mar 2013	32
2.8	BUM and DM Hysteresis	33
3.1	Freq Sweep Jun 2014	47

3.2	GPS Track Jun 2014	48
3.3	STEC Jun 2014	56
3.4	STEC S_4 Index Jun 2014	57
3.5	PSD Power Scaling Jun 06 2014	58
3.6	SEE Feature Frequency Scaling Jun 06 2014	59
3.7	STEC S_4 Index Jun 2014	60
3.8	Kodiak Radar Jun 06 2014	61
3.9	UAS Spectrogram Jun 2014	62
3.10	UAS Power Jun 06 2014	63
3.11	UAS Power Scaling Jun 06 2014	64
3.12	UAS Power Scaling with ERP Jun 06 2014	65
3.13	UAS Spectral Width Jun 06 2014	66
3.14	UAS Scintillation Index Jun 06 2014	66
3.15	STEC Power Fitting Jun 06 2014	72
3.16	Joint SEE and UAS Frequency Scaling Jun 06 2014	73
4.1	Vlasov Simulation Density Profile	82
4.2	Ion Density	85
4.3	Electron Temperature	86
4.4	Electron Temperature Snapshots	86
4.5	Electron Velocity Profile	87
4.6	E_x Frequency Spectrum	91
4.7	Separated Components of E_x	92
4.8	E_x Wavenumber Spectrum	92
4.9	E_x $\omega - k$ Spectrum	93
4.10	Bernstein Wave Dispersion Curves	94
4.11	E_x $\omega - k$ Windowed Spectrum	95
4.12	Decay paths to Electron Bernstein Waves	102
4.13	Normalized E_x Gradient $\omega - k$ spectrum	105
4.14	Normalized E_x Gradient	106
4.15	Windowed E_x $\omega - k$ Spectrum	107
4.16	Scaling of Electron Temperature with Pump Field	107
4.17	Ion Density and Electron Temperature - Vlasov	110
4.18	Electric Fields and $\omega - k$ Spectrum	111
4.19	Test-Particle Velocity Distribution - Overall	114
4.20	Test-Particle Velocity Distribution - Filtered	115
4.21	Electric Field Frequency Spectra	116
4.22	Test-Particle Velocity Distributions - Key Freq.	117
4.23	Test-Particle $x - v_{avg}$ Phase Space	119
4.24	Test-Particle $v_x - v_y$ Phase Space and v_{avg} Time Dependence	120
4.25	Initial Electric Field $\omega - k$ Spectrum	121
4.26	Selected Electric Field $\omega - k$ Spectrum	122
4.27	First Bernstein Wave $\omega - k$ Spectrum	125
4.28	Comparison with HAARP SEE Spectrum	127
4.29	Strong Langmuir Turbulence	129

List of Abbreviations

α	alpha
β	beta
AIT	Artificial Ionospheric Turbulence
BUM	Broad Up-Shifted Maximum
DM	Down-Shifted Maximum
EISCAT	European Incoherent Scatter Scientific Association
EUV	Extreme Ultraviolet
ERP	Effective Radiated Power
FAS	Field Aligned Striations
GPS	Global Positioning System
HAARP	High Frequency Active Auroral Research Project
HF	High Frequency
PRN	Pseudorandom Noise Number
PSD	Power Spectral Density
SEE	Stimulated Electromagnetic Emission
SSS	Super-small Scale Striations
STEC	Slant Total Electron Content
TECU	Total Electron Content Units
UAS	Ukrainian Antarctic Station
UV	Ultraviolet

Chapter 1: Introduction

This dissertation explores ionospheric plasmas with focus on the physics of phenomena near the upper hybrid layer. The present chapter provides background on plasma physics, the ionosphere, ionospheric dynamics, and ionospheric modification. It gives an overview of the plasma parameters in the Earth's ionosphere, discusses the composition and location of the many ionospheric layers, and addresses the propagation of high-frequency (HF) waves.

Chapter 2 presents the results of heating experiments at the High-frequency Active Auroral Research Project (HAARP) that resulted in the first detection of super-small striations (SSS). The chapter begins with an overview of previous HF heating experiments relating to the detection and production of field aligned striations (FAS). It provides a description of the experimental procedures and planned diagnostics, which include ground based stimulated electromagnetic emission (SEE) detectors, and measurements of signals transmitted by the PRN 07 GPS satellite. It concludes with an analysis and correlation of several diagnostics consistent with the detection of SSS, and hysteresis effects of SEE features during heating.

Chapter 3 extends the work from chapter 2 by adding modified experiments, and a new set of diagnostics at the Ukrainian Antarctic Station (UAS) in Verdan-

sky and the Kodiak radar system. These experiments were the first to detect the HAARP signal at UAS, nearly 16 Mm away from the HAARP facility. The chapter begins with an overview of experiments relating to artificial ionospheric turbulence (AIT), presents the new experiments and diagnostics, and finally, uses the correlations between these new diagnostics to draw conclusions about the mechanism by which the HAARP signal was injected into the ionospheric wave guide.

In chapter 4 we apply Vlasov simulations to the upper hybrid layer in an effort to establish parameters for the theory of descending artificial ionized layers (DAILs). First, we outline both the experimental observations of DAILs at the HAARP facility, and the theory that requires hot electrons near the critical layer to form them. Next, we present results of these simulations in parameter ranges accessible by HAARP, sweeping the pump field through a range of values consistent with the HAARP power upgrade, and we find collisionless, bulk heating of electrons near the upper hybrid layer for higher powers. We found that not only is the electron heating consistent with requirements of the DAIL formation theory, electron Bernstein waves play an important role in the heating. We then extend these simulations to mirror the parameters of our HF heating experiments described in chapters 2 and 3. We swept the frequency of the pump wave and found that the collisionless heating shifts from a bulk heating to a tail acceleration as the pump wave is swept through the fourth gyroharmonic. We also incorporated test particle simulations that allowed us to isolate wave modes, and correlate the bulk heating with electron Bernstein waves near the first gyroharmonic, and the tail heating with upper hybrid waves. This has given us specific predictions for ground-based obser-

vations in future heating experiments. The chapter concludes with using the output of our Vlasov simulations to feed the inputs to DAIL formation codes which may have applications for DAIL formation experiments at different frequencies.

Finally, chapter 5 presents the summary and overall conclusions of the dissertation.

1.1 Plasma Physics

We define a plasma as a quasineutral gas of charged and neutral particles which exhibits collective behavior [1].

Quasineutral means that particles in a plasma have to interact electromagnetically, but at the same time, the overall dynamics cannot be dominated by a long distance Coulomb interaction. There must be local charge separation, but this separation must be screened out over long distances into an overall charge neutrality. The Debye length

$$\lambda_D = \sqrt{\epsilon_0 k_B T_e / n_e q_e^2} \quad (1.1)$$

where ϵ_0 is the permittivity constant, k_B is Boltzmann's constant, T_e is the temperature of electrons, n_e is the density of electrons, and q_e is the electron charge (there is an additional ion term in the denominator which is typically dropped) measures the distance a charge's electrostatic effects can be experienced and gives the $1/e$ distance to screen the potential of a charge carrier. To be guaranteed that there are sufficient charge carriers to do the screening, we can count the number of charge carriers in a sphere of radius one Debye length, $N_D = n_e(4/3)\pi\lambda_D^3$, and require that

there be many. For a gas of charged particles to be quasineutral, it must have both a large scale size compared to its Debye length

$$L \gg \lambda_D \tag{1.2}$$

and it must have many charge carriers within each Debye sphere

$$N_D \gg 1. \tag{1.3}$$

Collective behavior is to be contrasted with an ordinary gas, where all interactions are mediated by local collisions. For a quasineutral gas to be a plasma, particles need to interact electromagnetically with their neighbors, not just with a hard sphere collision partner. The plasma frequency of electrons is $\omega_{pe} = \sqrt{n_e q_e^2 / m_e \epsilon_0}$ (in SI units) and is the response of electrons to a displacement with a Coulomb restoring force. For example, the electric field of a relatively high frequency electromagnetic passing through a gas might displace electrons, but not ions on the time scale that it passes and set up oscillations at ω_{pe} for electrons being pulled back to their ion counter parts. Gas kinetics for electrons would be dominated by electron-neutral collisions, the collision frequency is ν_{en} . If

$$\omega_{pe} > \nu_{en} \tag{1.4}$$

then electromagnetic interactions with neighbors will dominate the dynamics, and the quasineutral gas will exhibit collective behavior. If a gas of charged and neutral particles satisfies Eqs. 1.2, 1.3, and 1.4, it is a plasma.

The dynamics of the charged particles in a plasma are straightforward to write, but difficult to solve exactly. For a species α , the j^{th} particle's equation of motion

is given by the Lorentz force

$$m_\alpha \frac{d\vec{v}_\alpha^j}{dt} = q_\alpha \left(\vec{E}(\vec{x}, t) + \vec{v}_\alpha^j \times \vec{B}(\vec{x}, t) \right) \quad (1.5)$$

and the electric and magnetic fields \vec{E} and \vec{B} are derived from Maxwell's equations

$$\vec{\nabla} \cdot \vec{E} = \frac{\rho}{\epsilon_0} \quad (1.6)$$

$$\vec{\nabla} \cdot \vec{B} = 0 \quad (1.7)$$

$$\vec{\nabla} \times \vec{E} = -\frac{\partial \vec{B}}{\partial t} \quad (1.8)$$

$$\vec{\nabla} \times \vec{B} = \mu_0 \vec{J} + \frac{1}{c^2} \frac{\partial \vec{E}}{\partial t} \quad (1.9)$$

with ϵ_0 and μ_0 are the permittivity and permeability constants, c is the speed of light, ρ is the charge density, and \vec{J} is the current density. ρ and \vec{J} are related back to the original particle equations of motion from Eq.1.5 by summing over species and particle number

$$\rho(\vec{x}, t) = \sum_\alpha \sum_j q_\alpha \delta^3(\vec{x} - \vec{x}_\alpha^j) \quad (1.10)$$

$$\vec{J}(\vec{x}, t) = \sum_\alpha \sum_j q_\alpha \delta^3(\vec{x} - \vec{x}_\alpha^j) \vec{v}_\alpha^j \quad (1.11)$$

which is accurate, if not directly usable without further integration over ρ and \vec{J} . Typical plasmas have $j \rightarrow \infty$ or at least $j \gg 1$ and the collection of equations above represent a huge number of calculations. By replacing individual particles with macro-particles, and enforcing a grid for the fields and charge densities, these can be made tractable and this is the basis for the particle-in-cell (PIC) approaches to plasma modeling. Another approach is to ignore the computation of particle trajectories, and instead represent the collected particles by a distribution function

in space, velocity phase space, and time. If a species is described by the distribution function $f_\alpha = f_\alpha(\vec{x}, \vec{v}, t)$, the total phase space density of the particles should be conserved up to factors of collisions

$$\frac{df_\alpha}{dt} = \left(\frac{\partial f}{\partial t} \right)_C \quad (1.12)$$

where $(\partial f / \partial t)_C$ is the collision operator which describes the non-conservative effects on phase space density due to collisions. In general, this term can be quite complicated. In Cartesian coordinates, the total derivative of f_α is

$$\frac{df}{dt} = \frac{\partial f}{\partial t} + \frac{\partial f}{\partial x} \frac{dx}{dt} + \frac{\partial f}{\partial y} \frac{dy}{dt} + \frac{\partial f}{\partial z} \frac{dz}{dt} + \frac{\partial f}{\partial v_x} \frac{dv_x}{dt} + \frac{\partial f}{\partial v_y} \frac{dv_y}{dt} + \frac{\partial f}{\partial v_z} \frac{dv_z}{dt} \quad (1.13)$$

which can be further simplified by collecting terms 2-4, and 5-7. Terms 2-4 are the dot product of the velocity with the gradient operator

$$\frac{\partial f}{\partial x} \frac{dx}{dt} + \frac{\partial f}{\partial y} \frac{dy}{dt} + \frac{\partial f}{\partial z} \frac{dz}{dt} = \vec{v} \cdot \vec{\nabla} f \quad (1.14)$$

while terms 5-7 are the dot product of Newton's law $\vec{F}/m = d\vec{v}/dt$ with the $\partial/\partial\vec{v}$ operator

$$\frac{\partial f}{\partial v_x} \frac{dv_x}{dt} + \frac{\partial f}{\partial v_y} \frac{dv_y}{dt} + \frac{\partial f}{\partial v_z} \frac{dv_z}{dt} = \frac{\vec{F}}{m} \cdot \frac{\partial f}{\partial \vec{v}} \quad (1.15)$$

collecting Eqs. 1.13, 1.14, 1.15 and substituting into 1.12 we obtain the Boltzmann equation

$$\frac{\partial f_\alpha}{\partial t} + \vec{v} \cdot \vec{\nabla} f_\alpha + \frac{q_\alpha}{m_\alpha} (\vec{F}) \cdot \frac{\partial f_\alpha}{\partial \vec{v}} = \left(\frac{\partial f}{\partial t} \right)_C \quad (1.16)$$

For plasmas with low collision frequency and dominated by electromagnetic forces, Eq.1.16 can be reduced to the considerably simpler Vlasov equation.

$$\frac{\partial f_\alpha}{\partial t} + \vec{v} \cdot \vec{\nabla} f_\alpha + \frac{q_\alpha}{m_\alpha} (\vec{E} + \vec{v} \times \vec{B}) \cdot \frac{\partial f_\alpha}{\partial \vec{v}} = 0 \quad (1.17)$$

by dropping the collision operator and replacing \vec{F} with the Lorentz force. As with the particle description, the Vlasov equation can be combined with Maxwell's equations and the particle densities

$$\rho(\vec{x}, t) = \sum_{\alpha} q_{\alpha} n_{\alpha}(\vec{x}, t) \quad (1.18)$$

$$\vec{J}(\vec{x}, t) = \sum_{\alpha} q_{\alpha} n_{\alpha}(\vec{x}, t) \vec{v}_{\alpha} \quad (1.19)$$

where the number density and velocity density come from moments of the distribution function f_{α}

$$n_{\alpha}(\vec{x}, t) = \int_{-\infty}^{+\infty} f_{\alpha}(\vec{x}, \vec{v}, t) d^3v \quad (1.20)$$

$$\vec{v}_{\alpha}(\vec{x}, t) = \frac{1}{n_{\alpha}(\vec{x}, t)} \int_{-\infty}^{+\infty} \vec{v} f_{\alpha}(\vec{x}, \vec{v}, t) d^3v \quad (1.21)$$

this combined Vlasov-Maxwell system is an important part of numerical simulations described in chapters 4.

1.2 The Ionosphere

The ionosphere is a partially ionized gas surrounding the Earth from an altitude of about 50-500 km. It co-exists with the many layers of the neutral atmosphere which are in order of ascending altitude, the troposphere, stratosphere, mesosphere, and thermosphere. The neutral atmosphere's mass is concentrated in the troposphere with sharply decreasing neutral density with increasing altitude. There is a nearly uniform mix of neutral species below 100 km, but above 100 km, neutrals are separated by mass. The temperature decreases with altitude in the troposphere up to an altitude of about 10 km, where the absorption of ultraviolet radiation by ozone

[2] marks the transition to the stratosphere. Absorption causes increasing temperature with altitude up to about 50 km, where the temperature becomes dominated by radiative cooling and decreases sharply to about 150 K at 90 km, transitioning to the mesosphere, where absorption of high energy solar photons increases the neutral temperature from 150 K to 1500 K from 100-200 km. This high temperature region above 200 km is the thermosphere.

A large fraction of solar photons have sufficient energy to dissociate neutral atoms. The resulting combination of ions, electrons, and neutrals make up the ionospheric plasma. As solar radiation is absorbed during photoionization, the flux of ionizing radiation decreases with decreasing altitude, while at the same time, the neutral density increases, providing both additional targets to be ionized and an increased recombination rate of ions with free electrons. These factors lead to a series of ionospheric layers analogous to the atmospheric layers. In ascending order, they are the *D*, *E*, and *F* regions. A typical profile of the neutral atmospheric temperature and the ionospheric plasma density is shown in figure 1.1 with the various layers labeled [2].

The *D* region lies between 70-90 km and the primary source of plasma is the photoionization of *NO* molecules by the Lyman α photons with wavelength 120 nm, and secondary contribution from ionization of *N*₂ and *O*₂ by 1 nm x-rays during very high solar activity. The neutral density is high, recombination rates are high, and as a result the *D* region effectively vanishes at night, and during the day, the high neutral density makes the *D* region plasma highly collisional. The *E* region covers the altitude from 90-120 km, where the ionization is dominated by extreme

ultraviolet (EUV) ionization of O_2 and NO .

The F region, spanning 120-1000 km is created primarily by the ionization of atomic oxygen by ultraviolet (UV) and EUV radiation. In the F region, the plasma density is high, and the neutral density is considerably lower, so the plasma is weakly collisional, and on short time scales nearly collisionless. During the day, there is a division of the F region into an F_1 and F_2 region. The F_1 region occupies 120-200 km, and there are ions of atomic oxygen (O^+), molecular oxygen (O_2^+) and nitric oxide (NO^+). The F_2 region covers 200-300 km and is dominated by O^+ . The source of the F region's atomic oxygen is the photodissociation of molecular oxygen at lower altitudes,

The peak ionospheric plasma density occurs at the F_2 peak, and can reach densities of 10^{12} m^{-3} (10^6 cm^{-3}). At night, the F region contracts by approximately a factor of 10, and the F_1 and F_2 regions merge, while the D and E regions nearly vanish. In the D and E regions, recombination is driven by chemical reactions with the abundant neutrals such as



both of which are fast and energetically favored reactions. By contrast, the naive recombination reaction for atomic oxygen might look like



but this reaction is very slow, and so the actual ionospheric process becomes two-

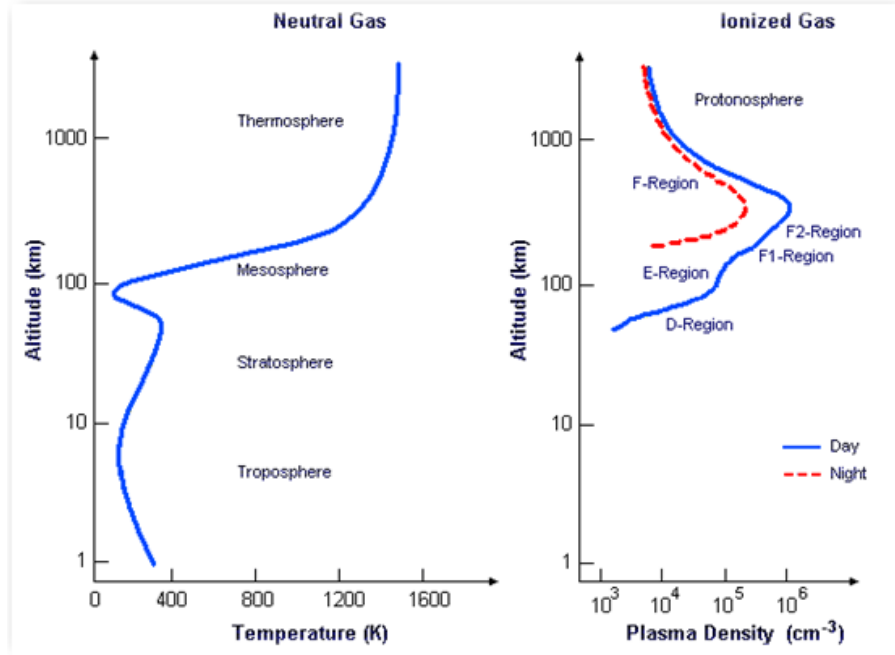


Figure 1.1: Typical altitude profiles the neutral atmosphere temperature and the ionospheric plasma density. Reproduced from Kelley [2]

steps which begins with a charge exchange of O^+ with a neutral



followed by a recombination reaction from Eq.1.23 to eliminate the free electron and ion. This first charge exchange step is slower than the straightforward recombination, and additionally, the F region has a lower neutral density of the reactants, which results in a much slower overall recombination rate that persists the F region into the night.

1.3 Ionospheric Dynamics and Conductivity

The presence of the Earth's geomagnetic field makes the ionosphere a magnetized plasma. Since the ionosphere is only partially ionized, and the ionization, ion species, and neutral density all vary with altitude, there can be distinct responses to applied electric fields at each of the regions discussed above. Ohm's law gives the current density

$$\vec{\mathbf{J}} = \bar{\bar{\sigma}} \cdot \vec{\mathbf{E}} \quad (1.27)$$

in terms of the electric field and the conductivity tensor $\bar{\bar{\sigma}}$, which is

$$\bar{\bar{\sigma}} = \begin{pmatrix} \sigma_P & -\sigma_H & 0 \\ \sigma_H & \sigma_P & 0 \\ 0 & 0 & \sigma_{\parallel} \end{pmatrix} \quad (1.28)$$

in terms of the Pedersen (σ_P), Hall (σ_H) and parallel (σ_{\parallel}) conductivities. The Pedersen conductivity gives the plasma response in the direction of an applied electric field, the parallel conductivity gives the response parallel to the magnetic field, while the Hall conductivity gives the response in the direction perpendicular to both the magnetic field and the electric field.

The parallel conductivity is [3]

$$\sigma_{\parallel} = \sum_{\alpha} \frac{q_{\alpha} n_{\alpha} \omega_{c\alpha}}{B_0 \nu_{\alpha n}} \quad (1.29)$$

where α represents the species, B_0 is the local geomagnetic field, $\omega_{c\alpha}$ is the cyclotron frequency $q_{\alpha} B_0 / m_{\alpha}$, and $\nu_{\alpha n}$ is the α -neutral collision frequency. The ratio $\omega_{c\alpha} / \nu_{\alpha n}$ is often expressed as $1/\Gamma_{\alpha n}$ which defines the magnetization for a species, with

$\Gamma < 1$ indicating that the species is magnetized, and $\Gamma > 1$ indicating that they are unmagnetized. At an altitude of about 65-70 km, the bottom of the D region, the electrons become magnetized and for all altitudes in the F region they have $\Gamma_{en} \ll 1$. At the bottom of the F region, at an altitude of about 120 km, $\Gamma_{in} \approx 1$ and the ions are only fully magnetized ($\Gamma_{in} \approx 0.1$) from 150 km and higher. In the F region, the parallel conductivity is large, indicating that a magnetic field line is an equipotential and particles may travel almost freely along it.

The Hall conductivity is [3]

$$\sigma_H = \sum_{\alpha} \frac{q_{\alpha} n_{\alpha}}{B_0} \frac{\omega_{c\alpha}^2}{\omega_{c\alpha}^2 + \nu_{\alpha n}^2} = \sum_{\alpha} \frac{q_{\alpha} n_{\alpha}}{B_0} \frac{1}{1 + \Gamma_{\alpha n}^2} \quad (1.30)$$

In the E region (90-120 km), the Hall conductivity can be significant since the electrons are magnetized, but the ions are not. At these altitudes, the ionosphere supports only electron waves such as whistlers, while in the F region, with both electrons and ions magnetized the Hall conductivity is small. The Pedersen conductivity is [4, 3]

$$\sigma_P = \sum_{\alpha} \frac{q_{\alpha} n_{\alpha}}{B_0} \frac{\nu_{\alpha n} \omega_{c\alpha}}{\omega_{c\alpha}^2 + \nu_{\alpha n}^2} = \sum_{\alpha} \frac{q_{\alpha} n_{\alpha}}{B_0} \frac{\Gamma_{\alpha n}}{1 + \Gamma_{\alpha n}^2} \quad (1.31)$$

in the F region, the Pedersen conductivity is the dominant conductivity due to the magnetization of both the ions and electrons, and the greatly increased plasma density. The primary response to electric fields will be perpendicular to the magnetic field, and parallel to the electric field, with both ion and electron waves supported.

1.4 Ionospheric Modification

The High-frequency Active Auroral Research Project (HAARP) is a leading ionospheric research facility near Gakona, Alaska and the location of all experiments described in this thesis in chapters 2 and 3. Using a 12x15 array of crossed dipole antennas, its transmitter is capable of up to 3.6 MW of power, which is amplified up to 5 GW Effective Radiated Power (ERP). Maximum ERP is frequency dependent, but HAARP can produce nearly its maximum ERP at any frequency from 2-10 MHz. Antennas can be independently phased allowing for simple "pencil" beams, or more exotic beams that have angular momentum, holes, etc. [5]. Propagation of HF waves from HAARP below the ionosphere is effectively propagation in free space, but as the waves approach the ionosphere, their propagation becomes more complicated as the ionospheric plasma is both nonuniform and anisotropic. The plasma density, composition, and as a result the index of refraction, are all altitude dependent and the index of refraction depends on the relative orientation of the wavevector, the wave electric field, and the geomagnetic field.

The Appleton-Hartree-Lassen equation [6] gives the index of refraction $\eta = ck_0/\omega_0$ for an electromagnetic wave propagating through a cold, magnetized plasma

$$\eta^2 = 1 - \frac{X}{U - \frac{1}{2} \frac{Y^2(1-\hat{k}\cdot\hat{b})^2}{U-X} \pm \sqrt{\left(\frac{1}{2} \frac{Y^2(1-\hat{k}\cdot\hat{b})^2}{U-X}\right)^2 + Y^2(\hat{k}\cdot\hat{b})^2}} \quad (1.32)$$

where \hat{k} and \hat{b} are unit vectors along the wavevector and magnetic field, $\hat{k}\cdot\hat{b} = \cos\theta$, $X = \omega_{pe}^2/\omega_0^2$, $\omega_{pe} = n_e q_e^2/m_e \epsilon_0$, $Y = \omega_{ce}/\omega_0$, $\omega_{ce} = q_e B_0/m_e$ $U = 1 - iZ$, and $Z = \nu/\omega_0$. The positive root corresponds to the ordinary (O) mode, waves that

are left-hand circularly polarized relative to B_0 (LHCP), while the negative root corresponds to the extraordinary (X) mode, right-hand circularly polarized (RHCP) with respect to B_0 . The simplest case of the Appleton-Hartree equation is if both magnetization ($Y = 0$) and collisions ($Z = 0$) are ignored. In this case, Eq.1.32 becomes

$$\begin{aligned}\eta^2 &= 1 - X & (1.33) \\ &= 1 - \omega_{pe}^2/\omega_0^2 \\ &\rightarrow \omega_0^2 = \omega_{pe}^2 + c^2 k_0^2\end{aligned}$$

showing identical behavior for the O- and X-modes under these assumptions. The reflection point for a wave, called a cutoff, is where $\eta = 0$. The cutoff for both the O- and X-modes are at the altitude z_R (reflection height) that satisfies $\omega_0 = \omega_{pe}(z_R)$.

While the F region is nearly collisionless, it is strongly magnetized. If we approach Eq.1.32 this time leaving the magnetization ($Y > 0$), ignoring collisions ($Z = 0$) while further assuming that a wave is injected at small angle relative to the magnetic field, so $\sin \theta \approx \theta$ and $\cos \theta \approx 1$, then Eq.1.32 reduces to

$$\eta^2 = 1 - \frac{X}{1 - \frac{1}{2} \frac{Y^2 \theta^2}{1-X} \pm Y} \quad (1.34)$$

and the cutoff can again be found by setting $\eta = 0$

$$\begin{aligned}0 &= 1 - \frac{1}{2} \frac{Y^2 \theta^2}{1-X} \pm Y - X & (1.35) \\ 0 &= X^2 + X(\mp Y - 2) + (1 - \frac{1}{2} Y^2 \theta^2 \pm Y)\end{aligned}$$

which is quadratic in X and can be solved by

$$X = -\frac{1}{2}(\mp Y - 2) \pm \frac{1}{2} \sqrt{(\mp Y - 2)^2 - (4)(1)(1 - \frac{1}{2} Y^2 \theta^2 \pm Y)} \quad (1.36)$$

simplifying and carefully separating the \pm arising from the two roots of the quadratic as a $(-1)^n$ from the \pm relating to the O/X mode wave

$$X = \frac{1}{2} \left[2 \pm Y + (-1)^n Y \sqrt{1 \mp} \right] \quad (1.37)$$

finally letting $\theta \rightarrow 0$ and choosing the $n = 0$ mode ($n = 1$ has other physical significance that is discussed in [7])

$$X = 1 \pm Y \left(\frac{1 \mp 1}{2} \right) \quad (1.38)$$

for the O-mode, $X = 1$ and the cutoff is at the O-mode reflection altitude given by $\omega_0 = \omega_{pe}(z_{O,R})$. For the X-mode, $X = 1 - Y$ and for the F region, $Y < 1$,

$$\begin{aligned} \frac{\omega_{pe}}{\omega_0} &= \sqrt{1 - \frac{\omega_{ce}}{\omega_0}} \approx 1 - \frac{\omega_{ce}}{2\omega_0} \\ &\rightarrow \omega_0 = \omega_{pe}(z_{X,R}) + \frac{1}{2}\omega_{ce} \end{aligned} \quad (1.39)$$

with $z_{O,R} > z_{X,R}$. As the O-mode wave approaches the reflection altitude, it transforms from an electromagnetic to an electrostatic wave, and the perpendicular electric fields decay while the parallel electric fields are enhanced in an Airy pattern [8] of large enough amplitude to drive Langmuir waves. These waves and the resulting turbulence are relevant to the results of chapter 4.

As waves pass through the ionospheric plasma to their reflection point, their electric field induces oscillations in the electrons and ions as they pass. The oscillating particles can collide with neutrals, extracting energy from the wave to thermal energy of the particles. This process is called collisional absorption, and this type of absorption is dominant in the D and E regions where the neutral density and collision frequencies are high.

Under typical ionospheric conditions an HF wave transmitted into the F-region of the ionosphere will undergo collisional absorption, transferring about 5% of its total energy into heating of the plasma. Experiments performed by Cohen and Whitehead [9], Stubbe et al. [10], Jones et al. [11] demonstrated that under certain conditions, the HF wave can be anomalously absorbed, converting between 95-99% of its energy into the plasma. This effect occurs only for O-mode waves between the upper hybrid resonance and the O-mode reflection point, and is caused by the mode conversion of the O-mode wave to upper hybrid waves trapped in density striations near the upper hybrid layer.

The upper hybrid layer is a part of the F region where the local plasma density causes the pump wave frequency to match the upper hybrid frequency, $\omega_0 = \omega_{UH} = \sqrt{\omega_{pe}(z_{UH})^2 + \omega_{ce}^2}$. As above, in the F region, $\omega_{ce}/\omega_{pe} < 1$ so this can be estimated by $\omega_0 \approx \omega_{pe}(z_{UH}) + \frac{1}{2}\omega_{ce}(\omega_{ce}/\omega_{pe})$ which gives a comparison with the reflection height of O/X mode waves

$$z_{0,R} > z_{UH} > z_{X,R}. \quad (1.40)$$

This upper hybrid layer lies between the reflection point of the O/X mode waves, which explains why the anomalous absorption effect is only reported for O-mode waves. In experiments, it is typically found between 3-10 km below the O-mode reflection height. At the upper hybrid layer, the large Pedersen conductivity, as well as the fact that $\hat{k} \cdot \hat{b}$ is typically small at HAARP, gives a displacement of electrons nearly perpendicularly to the magnetic field. The displaced electrons experience not only a restoring force from the Coulomb force (ω_{pe}) but from the Lorentz force as well

(ω_{ce}) and so they oscillate at the upper hybrid frequency $\omega_{UH} = \sqrt{\omega_{pe}(z_{UH})^2 + \omega_{ce}^2}$. Since the collision frequency is low in this region, upper hybrid oscillations can continue without collisional absorption and damping. The plasma density is not uniform, and experiments by Kelley et al. [12] with in situ rocket measurements over the Arecibo heating facility indicated that there are magnetic field-aligned striations (FAS) of 5-10 m width, and 15 m separation across the field line. In the presence of these background density striations, the upper hybrid oscillations induced by the pump wave can be trapped [13, 14] if the pump wave matches the upper hybrid frequency inside the striation but not immediately outside. Continued pumping can amplify the field of the trapped waves, to allow parametric instabilities, and create a broad wavenumber spectrum of upper hybrid turbulence inside the density striations, heating the electrons, increasing pressure along the field line, and reinforcing the striation by transporting plasma along the field line (large σ_{\parallel}). Additional experiments performed by Rietveld et al. [15], Honary et al. [16] showed that the temperature of the electrons is increased when the heater beam is moved from the vertical to the magnetic zenith (MZ). In this situation, the O-mode wave propagates nearly parallel to the magnetic field lines near the upper hybrid layer, and the electric field of the wave is oriented perpendicularly to the field lines. Anomalous absorption, the formation of striations, and the excitation of waves at the upper hybrid layer will be key points of all subsequent chapters.

Chapter 2: Generation of Super Small Striations at HAARP

2.1 Overview

Generation of artificial Field-Aligned Striations (FAS) of the ionospheric plasma due to F region O-mode HF heating was first discovered in experiments conducted by the Platteville HF heater [17, 18] and subsequently confirmed in numerous experiments [19, 12, 20, 21]. These studies demonstrated that FAS could be used as a scattering cloud for ground-to-ground VHF communications. A key parameter required to design such communications systems is the total radar scattering cross section (SCS) per unit volume [22]. One of the factors that determines the SCS is the wave number spectrum of artificial fluctuations of the electron density. According to Rao and Thome [23], at Platteville, the value of SCS was measured to decrease by 5 orders of magnitude when the radar frequency is swept from 20 MHz to 1 GHz. This implies that the scattering of a probe signal in the GHz frequency range is expected to be negligible, which further indicates that the spectrum of density fluctuations quickly decays for wavelengths smaller than 30 cm. However, following a suggestion of Gurevich and Zybin [24], Milikh et al. [25] recently observed strong perturbations of GPS signals by FAS generated by the High Frequency Active Auroral Research Program (HAARP) heater operating at 92 dBW Effective Radiated Power. These

perturbations are indicative of excitation of super small striations (SSS) on the order of 10 cm. The observations of Milikh et al. [25] were performed using O-mode HF F region heating with a frequency ω that satisfied the so-called double resonance condition, namely ω resonated at the upper hybrid height with a multiple of the electron cyclotron frequency ($\omega_{UH} \approx n\Omega_e$). Ground measurements of the differential phase of GPS signals traversing the heated region indicated high level of SSS. However, the nonlinear physics that allows generation of such SSS and its relationship to Artificial Ionospheric Turbulence (AIT) was unclear. The present set of experiments coordinate GPS and Stimulated Electromagnetic Emission (SEE) observations, and include complementary diagnostics by HAARPs Digisonde and Modular UHF Ionospheric Radar (MUIR), in an effort to study the properties of SSS generated by the HAARP heater.

2.2 Description of Experiment

We report below observations from six daytime experiments, conducted during the March 2013 HAARP campaign. In the experiments, the HAARP heater operated at its maximum 3.6 MW power, O mode, and the HF beam was directed toward the PRN 07 satellite at 15° off zenith and 180° azimuth. PRN 07 is a GPS satellite on a geocentric orbit with inclination 55.1° to the equator, having perigee 20 143 km and apogee 20 222 km. During the experiments, PRN 07 overflew the HAARP site daily and the signals at both the L1 ($f_1 = 1.575$ GHz) and L2 ($f_2 = 1.227$ GHz) were measured on the ground after traversing the HF heated region (see figure 2.1)

2) with one Hz sampling rate. The measured differential carrier phase was used to estimate the relative Slant Total Electron Content (STEC) and the value of $\delta n/n$ at 20 – 30 cm scale length that corresponds to the Bragg condition at the GPS frequency range. Stimulated Electromagnetic Emission (SEE) signals were measured simultaneously using an HF detector operated by the Naval Research Laboratory 15 km away from the HAARP site. Data acquisition techniques have been described previously by Bernhardt et al. [26, 27]. The SEE signals are driven by the nonlinear interaction of the injected HF wave with the ionospheric plasma that results in broadband emissions at frequencies different from the injected HF frequencies [28]. They are usually upshifted or downshifted from the heater frequency within a range of 100 kHz. All the experiments were also diagnosed by the HAARP ionosonde and when the geometry permitted by the on-site Modular UHF Ionospheric Radar (MUIR).

The experiments were conducted using square pulse HF heating with 10 s pulse width and 10 s interpulse period. To determine the turn-on and decay times of the excited striations, a train of short, square, 20 ms pulses, at the heating frequency of the preceding 10 s pulse, and with an interpulse time 1 s was applied between the long, 10 s pulses as shown schematically in figure 2.2.

The HF frequency selection was constrained by two requirements: First, to maintain the HF frequency f_0 below the F_2 layer critical frequency ($f_0 < f_{O}F_2$), and second, to operate in the vicinity of the double resonance condition ($f_{UH} \approx n f_{ce}$). During the experiments, the $f_{O}F_2$ was approximately 6 – 7 MHz. As a result, the double resonance could be satisfied in the vicinity of the fourth electron gyrohar-

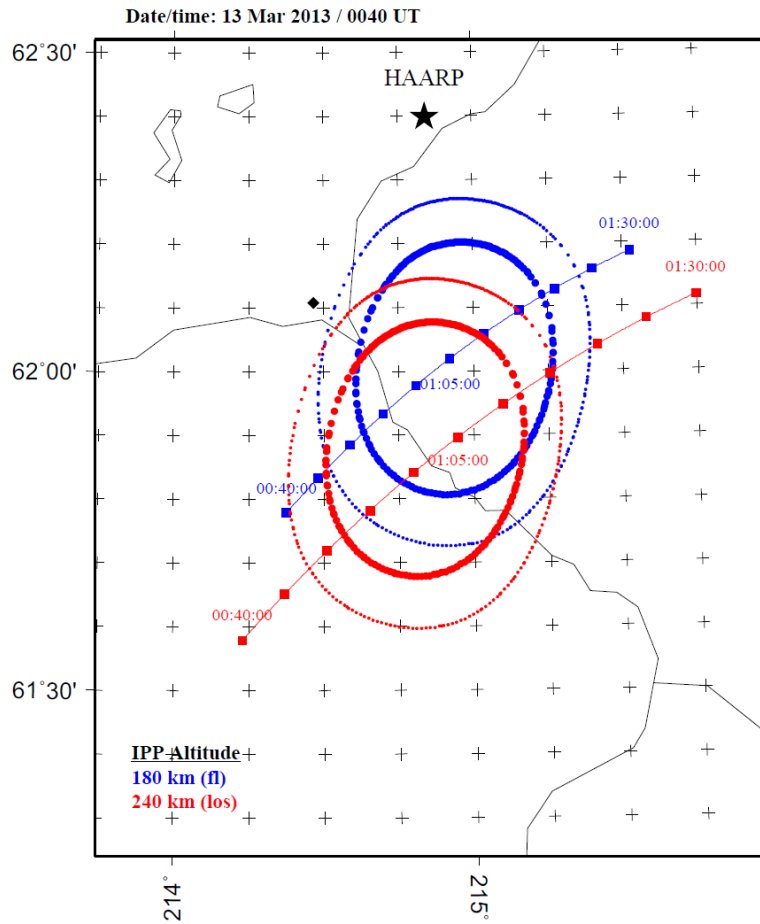


Figure 2.1: Heater contours and satellite tracking on 13-Mar-2013. HAARP HF heating contours of 3 and 6 dB at altitudes of 180 and 240 km are shown in red and blue ovals. Crossing position of a microwave beam from PRN 07 directed toward the HAARP receiver, at altitudes of 180 and 240 km, are indicated on the red and blue lines.

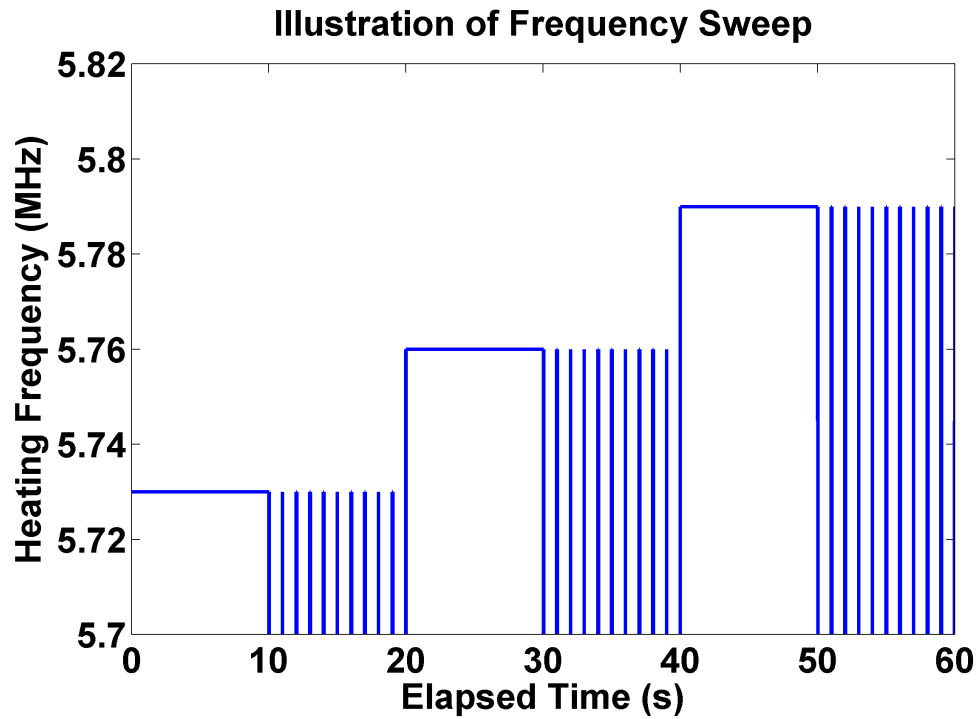


Figure 2.2: Illustration of frequency sweep. Heater alternates 10 s, square pulses with a train of 20 ms, square pulses with interarrival time of 1 s. After a cycle, the heating frequency is stepped up or down by 30 kHz.

monic close to 5.8 MHz. The heater operation was as follows: Starting at 300 – 500 kHz below the fourth gyroharmonic, the heating frequency was stepped up by 30 kHz every 20 s until it reached 5.9 – 6.0 MHz. On 11 March 2013, the heating was terminated after reaching ≈ 6.0 MHz. On subsequent days, the frequency was cycled back after reaching 6 MHz in 30 kHz steps every 20 s, thereby crossing the expected gyroharmonic from above and below.

The critical diagnostic instrument is a GPS receiver located at HAARP that detects the changes in the phase of the GPS signals sent from the PRN 07 satellite crossing the heated region and received at HAARP. Other important diagnostic instruments were a broadband HF receiver operated by the Naval Research Laboratory that measured SEE signals, the ionosonde that measured the plasma density profile above the site and the MUIR radar that measured plasma waves excited by the heater.

Table 2.1 lists the key parameters of the experiments, including experiment times and ionospheric conditions. During all the experiments, the on-site diagnostics indicated a smooth F region layer, weak to moderate D and E region absorption, and the absence of electrojet current. Moreover, the HAARP magnetometer showed small variations of the geomagnetic fields ($\delta B < 20$ nT) , indicating a quiet ionosphere.

Table 2.1: Key experimental information, including the experiment times, heating regime, HF frequency (f_0), and the critical frequency (f_oF_2). These experiments were performed during the March 2013 HAARP Campaign, and used 30 kHz steps between heating frequencies.

Expt.	UTC	Pattern	Freq. (MHz)	f_oF_2 (MHz)	notes
11-Mar	01:05:00- 01:14:30	10s/10s	5.3-5.9	5.7-6.8	N/A
12-Mar	01:00:00- 01:09:30	10s/10s	5.5-5.9, 6.8-7.0	6.7-7.8	N/A
13-Mar	00:55:00- 01:04:10	10s/10s	5.3-5.9, 5.9-5.3	6.1-7.7	Overshoot in STEC
14-Mar	00:50:00- 00:59:40	10s/10s	5.5-6.0, 6.0-5.5	7.3-7.6	Overshoot in STEC
15-Mar	00:50:00- 00:59:10	10s/10s	5.5-6.0, 6.0-5.5	6.3-7.4	Overshoot in STEC
16-Mar	00:45:00- 00:54:00	10s/10s	5.5-6.0, 6.0-5.5	6.4-6.6	N/A

2.3 Experimental Observations

As mentioned above, figure 2.1 presents an overview of the GPS experiment and the HAARP heated regions. The figure shows the tracking of PRN 07 relative to the HAARP heated region, with the red and blue ovals outlining the 3 and 6 dB contours of the heated region at altitudes of 180 and 240 km on 13 March 2013 with HAARP indicated by a star. The colored lines are the projection of points where a microwave beam from the satellite directed toward the HAARP receiver, crosses a surface at the given altitude. PRN 07 was chosen for this experiment because it crosses almost directly over the center of the heated region. It takes 10 min for the GPS satellite to fully cross the heated region, and this sets the time scale of our GPS diagnostics.

The processing of the received GPS signals was described in detail in Milikh et al. [25]. It uses the observed phase ϕ_1 and ϕ_2 of both the L_1 ($f_1 = 1.575$ GHz) and L_2 ($f_2 = 1.227$ GHz) GPS frequencies and estimates the differential carrier phase $\Delta\phi_{1,2}$. The latter then was converted to relative Slant Total Electron Content (STEC) using

$$\Delta(STEC) = \frac{0.75 f_1 \Delta\phi_{1,2}}{f_1^2 / f_2^2 - 1}. \quad (2.1)$$

The STEC is measured in TEC units with 1 TEC unit equivalent to 10^{16} electrons per square meter, the frequencies are in GHz, and the differential carrier phase is in radians. Further analysis and description of GPS phase differences caused by ionospheric scintillation is described by Pelgrum et al. [29].

Figures 2.3(a) and 2.3(b) show the absolute STEC versus the observational

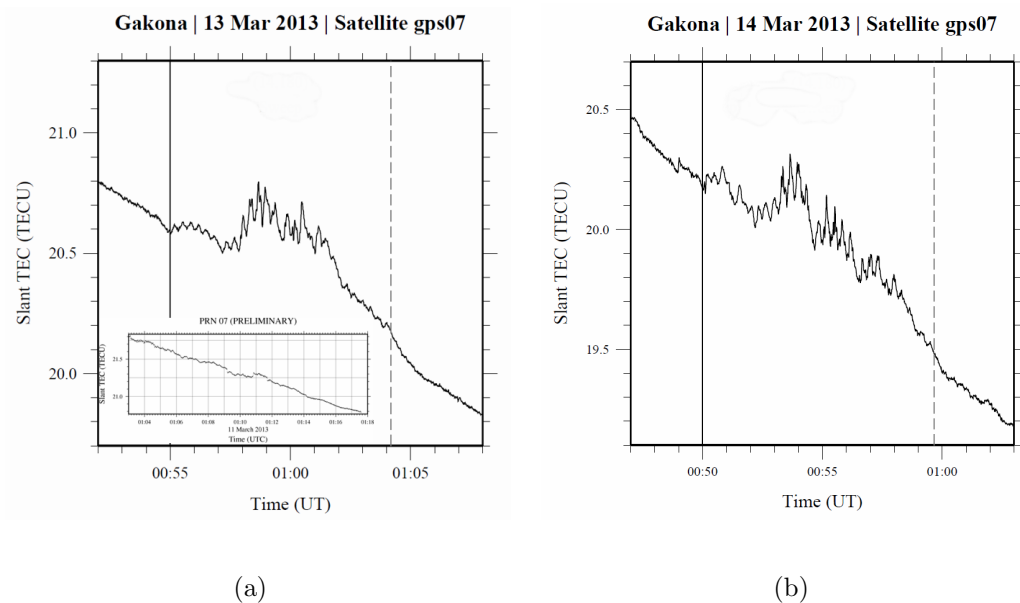


Figure 2.3: STEC observations made on (a) 13 March 2013 and (b) 14 March 2013. Unpertrubed STEC from 11 March 2013 is included for reference in (a). The beginning and end of HF heating is indicated with solid and dashed lines, respectively.

time measured during experiments 3 and 4, with the beginning and end of the HF heating shown by the two vertical lines. The STEC of the probe GPS signals changes abruptly in about 35 s following turn-on of the HF heating, and then oscillates with the 20 s heating period. As mentioned above, within minutes, PRN 07 moves from the center of the heated region, where the HF heating effect is strongest, to its periphery, producing an approximately linear decay of STEC. For comparison, the STEC obtained in the absence of HF heating was inserted in figure 2.3(a).

Figure 2.4 shows dynamic SEE spectra observed during experiment 4. The x-axis shows the varying frequency in a bandwidth of 200 kHz centered about 5.82 MHz, while the y-axis shows the elapsed time from 00:52:03 UT. The intensity

of the observed signal is color coded. The 10 s long pulses are characterized by the pump wave: a bright, narrow line of constant frequency. The 10 s and +30 kHz separate successive long pulses. Between these long pulses, the short 20 ms pulses mentioned above (2.2) are also shown. During the first long pulse (lower left), the SEE shows two spectral lines downshifted from the pump, known as the first and second downshifted maximum (DM). The next long pulse is dominated by the pump wave with faint evidence of a transient DM, indicative of the well-known DM suppression near the gyrofrequency [30]. The third long pulse shows a broad region of lower amplitude, but higher frequency than the pump. This is the Broad Upshifted Maximum (BUM), indicating that we have exceeded a multiple of the gyroresonance. The relative amplitude and frequency shift of the BUM relative to the pump wave vary with the pump frequency.

Figure 2.5 reveals one of the most important results of the experiment, the correlation between STEC amplitude fluctuations and the power spectral density (PSD) of the SEE spectra for experiment 4. During the first 3 min of the HF heating, the peaks of the STEC are associated with the presence of DM on the SEE spectrum. The BUM first appears at 00:53:16 UT, approximately 3 min from the beginning of heating and remains for ≈ 2 min which corresponds to a shift in the heating frequency of ≈ 150 kHz. During that time, the STEC shows large-amplitude oscillations, by up to 4 dB larger than during the first 3 min. The BUM is associated with a rising amplitude of the STEC and is coincident with the first of two overshoots (or humps). The first hump lasts for ≈ 1.5 min and the second starts at $\approx 00:55:06$ UT and lasts for ≈ 1 min. In these humps, the value of the STEC changes by up to

Spectrogram of Data Collected on 2013-03-14 at 00:52:03

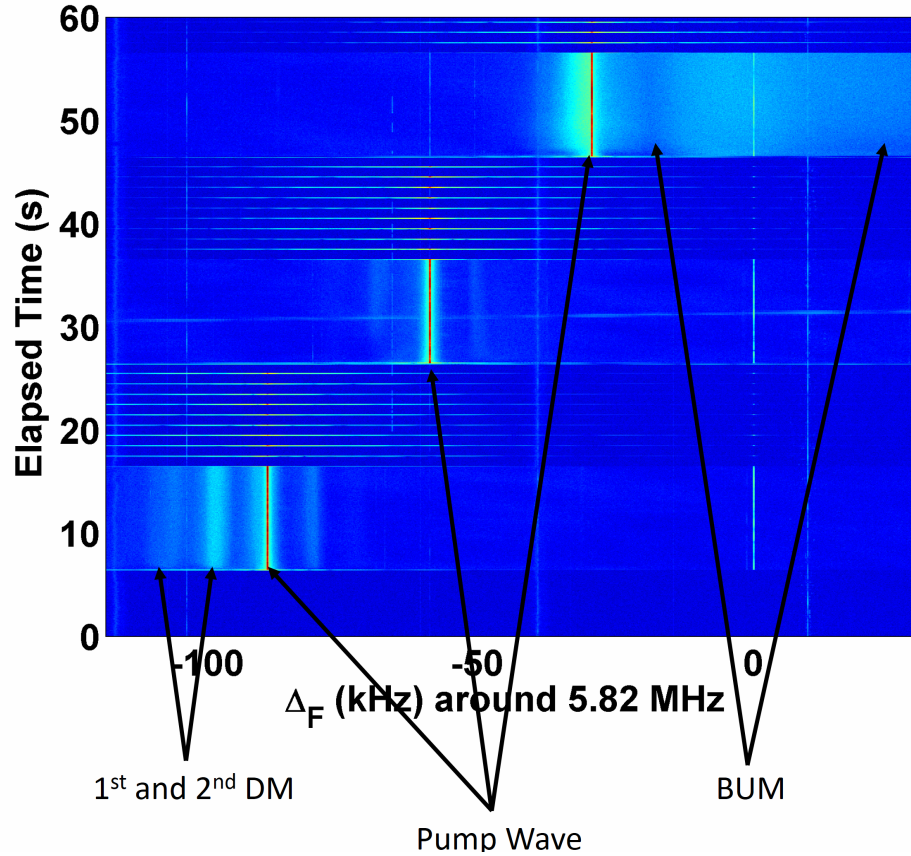


Figure 2.4: SEE Spectrogram from 14 March 2013. Frequency axis is centered on 5.82 MHz, and indicated pump waves are from bottom to top: 5.73, 5.76 and 5.79 MHz. For the pump at 5.73 MHz (lower left), the first and second DM are present and shifted by ≈ -10 kHz and ≈ -20 kHz, respectively, from the pump frequency. For the pump at 5.79 MHz (upper right), BUM is evident in the range of +10 to +50 kHz from pump frequency. The pump at 5.76 MHz (center) appears to be very close to a gyroresonance as DM is suppressed and BUM is not yet visible.

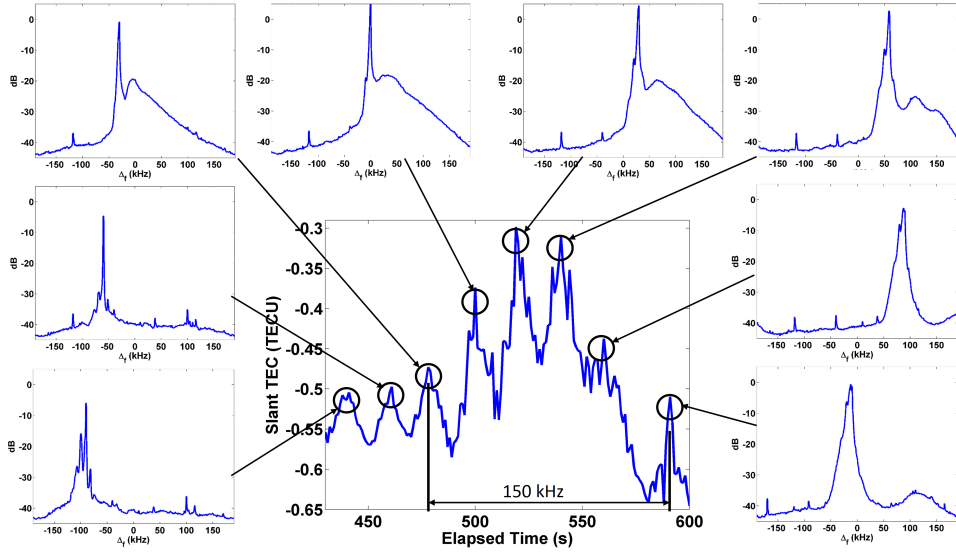


Figure 2.5: STEC observations near the first hump or overshoot made on 14 March 2013 with selected PSDs. First BUM indicated. PSDs progress in time clockwise starting from the lower left, and UT are indicated. STEC hump covers an HF heating frequency range of 150 kHz.

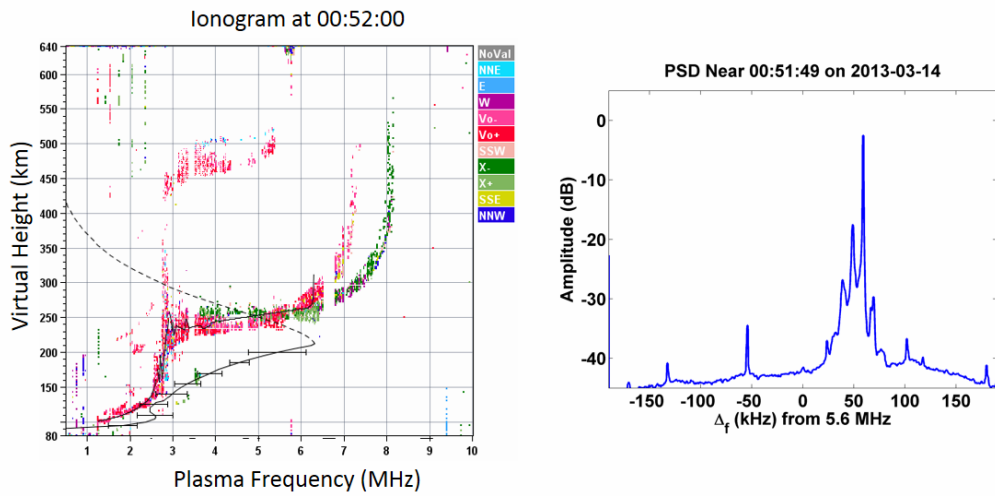
0.3 TECU and the SEE spectrum shows that a BUM is being excited.

Figures 2.6(a) and 2.6(b) show ionograms made at 2 and 4 min during the HF heating on 14 March 2013, along with the PSD of the nearest long pulse heating cycle. We found that in the first case, the SEE spectrum shows a DM, while in the latter case, the BUM has developed. At the same time, the latter ionogram indicates a spread F layer. In addition, during these times, the STEC transitions from small ($\approx 0.05 - 0.07$ TECU) near 00:52:00 UT to larger ($\approx 0.15 - 0.20$ TECU) near 00:54:00 UT. Due to angular limitations of HAARPs MUIR instrument, it is difficult to detect this turbulence directly. In spite of this difficulty, a single successful MUIR measurement was made on 14 March 2013 during the period 00 : 52 : 10 – 00 : 52 : 20

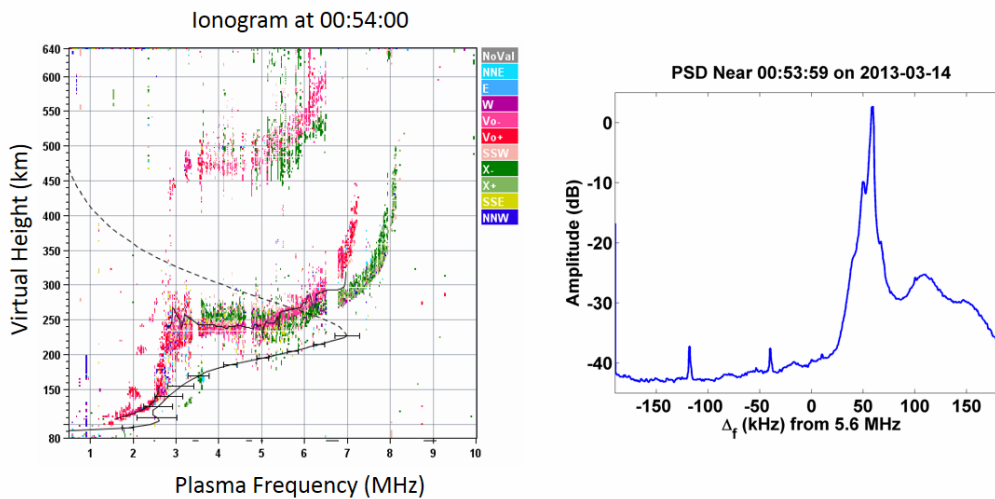
during which time $f_0 < 4f_{ce}$. It shows strong reflection in 200 – 203 km range (illustrated in figure 2.7) that lasted for over 2 s followed by a faint signal that lasted for 8 s. During that time, the SEE spectrum reveals the DM, 2DM, 3DM, and upshifted maximum features although the BUM was absent. GPS measurements indicated small STEC (0.05 – -0.07 TECU) oscillations during this time. We will discuss these findings further in subsequent sections.

2.3.1 Hysteresis Effect

In four of the experiments (3-6), the heating frequency was swept from $f_0 = 5.5$ MHz corresponding to $4f_{ce}$ in increments of 30 kHz up to $f_0 = 6$ MHz, which is 100150 kHz above the BUM pumping frequency, and then cycled down to 5.5 MHz. Detailed comparison revealed a difference between the PSDs recorded during up and down frequency sweeps. This is shown in figure 2.8 for experiments 3 and 4. Figure 2.8(a) shows the amplitude of the peak of the BUM taken from PSDs at different pumping frequencies. During the upward sweep, the BUM peak has higher amplitude than the downward sweep. By contrast, the peak of the first DM (figure 2.8(b)) shows hysteresis behavior but with the up sweep having lower amplitude than the down sweep. Hysteresis of the BUM is consistent with the observations of Carozzi et al. [31]. Hysteresis of the DM is consistent in magnitude, but we observe a switch in the relative amplitude of the up and down sweeps.



(a)



(b)

Figure 2.6: Ionograms taken at HAARP 14 March 2013 at (a) 00:52:00 and (b) 00:54:00 UT by the Digisonde, with associated SEE PSD. Note the broadening of ionogram in the presence of BUM. First ionogram indicates a compact F layer and is correlated with a DM in the SEE spectrum, while the second ionogram indicates a spread F layer and is correlated with a BUM in the SEE spectrum.

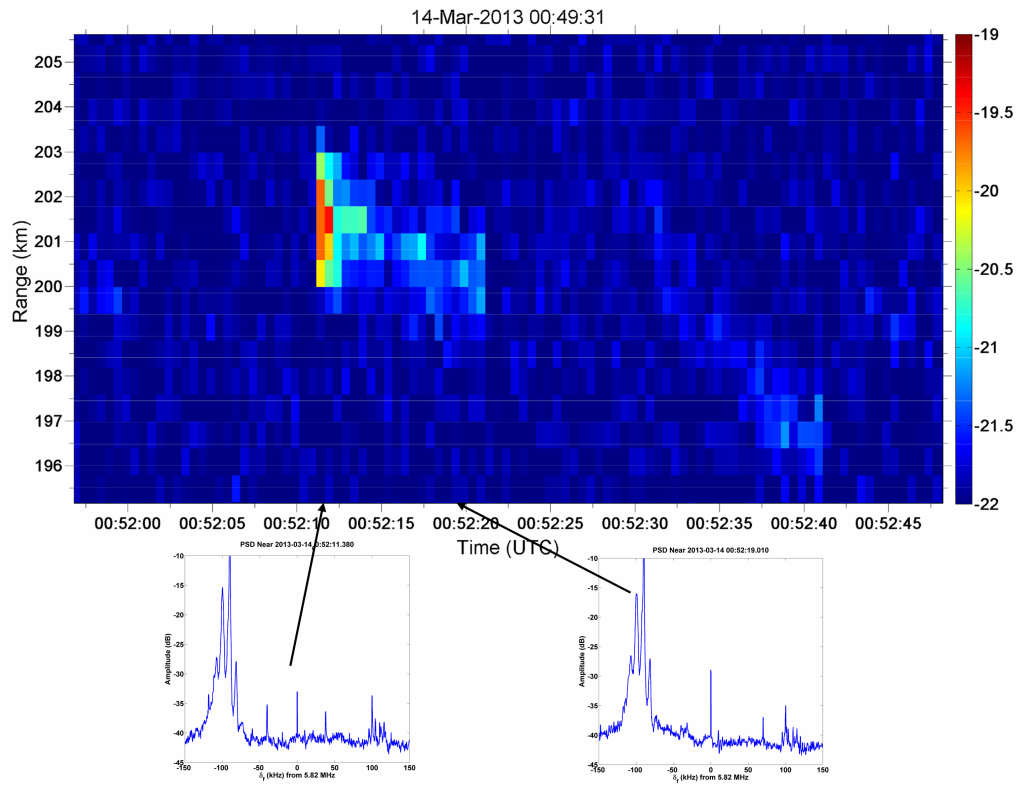
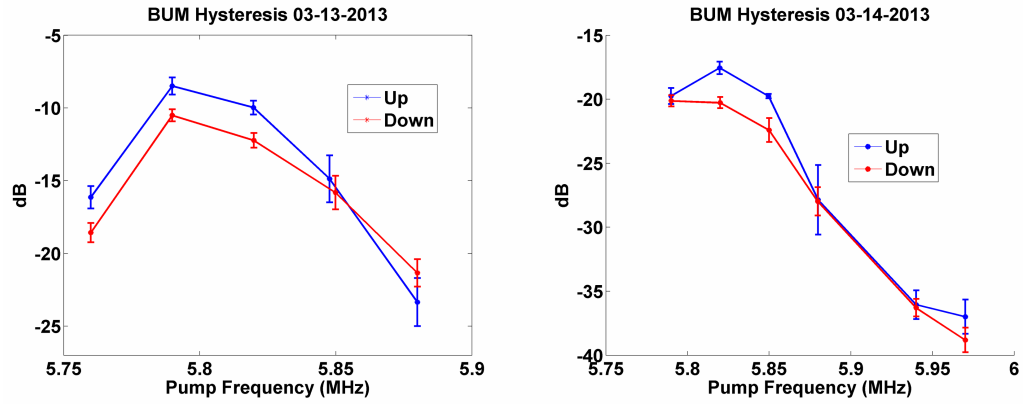
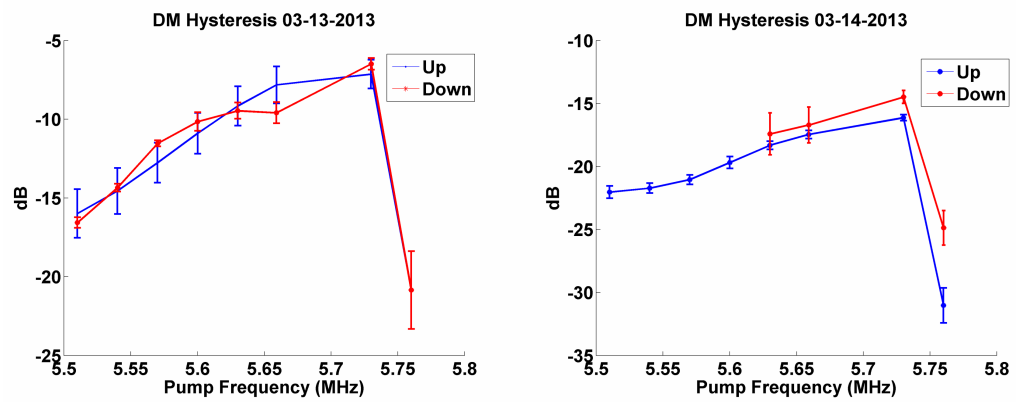


Figure 2.7: MUIR measurements taken at HAARP 14 March 2013 at 00:52:00-00:52:45 with selected SEE PSDs. Width of heated region is 34 km. SEE spectrum indicates the presence of only DM during this measurement.



(a)



(b)

Figure 2.8: Hysteresis of (a) BUM, (b) DM, measured on 13 March and 14 March.

In all plots, forward or up sweep is indicated in blue, backward or down sweep is indicated in red.

2.3.2 Excitation and Relaxation Times

During various experiments, we operated with the heater off during selected periods. This gave us an opportunity to investigate the excitation and relaxation times of both the BUM and the DM. Our results are summarized in Table 2.2. For the DM excitation, we sliced the spectrograms of the SEE data along constant time and inspected the resulting frequency spectrum for DM features. We found that the DM took ≈ 7 ms to excite with error bars from analyzing statistics of the experiment. We employed the identical procedure for the BUM, restricting our inspection to long pulse heating cycles when it became evident that the BUM was not excited by the short pulses. We found that the BUM took ≈ 200 ms to excite. To measure the relaxation times, we examined the transition between long and short pulse heating. Again, slicing the spectrograms along constant time, we examined the frequency spectrum during a short pulse heating for persistent features of the DM and BUM that were previously excited during long pulsed heating. We found no evidence of persistent features, indicating that the DM and BUM both relax in under 1 s. Our excitation and relaxation times are consistent with the results presented by Sergeev et al. [32] who found that the excitation time for the DM is under 20 ms, while that for the BUM is much longer. After noting the hysteresis effect discussed above, we also sought to observe the characteristic hysteresis time scale. To compute this, for the DM and the BUM separately, we tracked the time taken to return to the frequency corresponding to the maximum SEE amplitude on the forward sweep to the maximum amplitude of the backward sweep. We found the BUM hysteresis

Table 2.2: Summary of time scales for the excitation, relaxation, and hysteresis-return for the BUM and DM features.

Time Scale	BUM	DM
Excitation	200 ± 80 ms	6.5 ± 1.3 ms
Relaxation	< 1 s	< 1 s
Hysteresis	≈ 200 s	≈ 300 s

return time was ≈ 200 s, while the DM return time was ≈ 300 s.

2.4 Discussion

The phase change of a GPS signal of frequency ω passing through the perturbed region of the ionosphere is given by Milikh et al. [25]

$$\Delta\phi = \frac{\omega}{c} \int \epsilon dz \approx \frac{\omega \omega_e^2}{c \omega^2} \frac{\delta n_e l}{n_e} \quad (2.2)$$

where ϵ is the refractive index, $\omega_e = \sqrt{4\pi e^2 n_e / m_e}$ is the electron plasma frequency, δn is the electron density perturbations due to HF heating, and l is the length of the ray in the perturbed region. The differential carrier phase $\Delta\phi_{1,2}$ of two rays with frequencies f_1 and f_2 crossing the perturbed region is given by

$$\Delta\phi_{1,2} = \frac{2\pi f_2 f_{ep}^2}{c f_2^2} \left(1 - \frac{f_2}{f_1}\right) \frac{\delta n_e l}{n_e} \quad (2.3)$$

Applying this to the L_1 and L_2 frequencies for the experiment 4 on 14 March 2013 with f_{ep} close to 5.8 MHz, we obtain

$$\Delta\phi_{1,2} \simeq 0.13 \frac{\delta n_e l}{n_e} \quad (2.4)$$

with $\Delta\phi_{1,2}$ given in radians and l in km. Combining Eq. 2.2 with Eq. 2.4, we estimate the relative perturbations of the electron density leading to GPS scattering to be

$$\frac{\delta n_e}{n_e} \simeq 4.37 \frac{\Delta(STEC)}{l(km)} \quad (2.5)$$

We find that our ionograms from experiment 4 (Figure 2.6) combined with the known GPS frequencies indicate the width of the heated region to be $\approx 3 - 4$ km, and this is consistent with MUIRs measurements (Figure 2.7). Combining the size of the turbulent region with STEC fluctuations mentioned above, we found that during the HF heating that excited a DM in the SEE, $\delta n/n = 5 - 7\%$, while during heating which excited a BUM, $\delta n/n = 20 - 30\%$. The strong scattering of the GPS in the presence of the BUM in the SEE spectrum indicates that SSS are connected to electron Bernstein modes, as predicted by Gurevich and Zybin [24]. Note that in this experiment, $\delta n/n$ was measured indirectly through differential phase measurements of the GPS signal from PRN 07. It may be useful in the future to confirm these results, such as through direct measurements of the amplitude of the scattered signal.

A likely mechanism for the relaxation of striations is ambipolar diffusion. For a long cylindrical plasma column, the coefficient of ambipolar diffusion can be approximated by the electron diffusion across the geomagnetic field [1].

$$D_a = \frac{T_e \nu_{ei}}{m \omega_{ce}^2} = \frac{v_{th}^2 \nu_{ei}}{2 \omega_{ce}^2} \quad (2.6)$$

where v_{th} is the electron thermal velocity and ν_{ei} is the electron-ion collision frequency given by

$$\nu_{ei} = 2.9 \times 10^{-6} n_e \log \Lambda / T_e^{3/2} \quad (2.7)$$

with the coulomb logarithm $\log \Lambda = 23 - \log \left(n_e^{1/2} T_e^{3/2} \right)$, the electron temperature is in eV, and the electron density is in cm^{-3} . For the ambient $T_e = 0.15$ eV, and $n_e = 4.5 \times 10^5 \text{ cm}^{-3}$, which corresponds to the plasma density that reflects 6 MHz heating radio waves, we obtain $\nu_{ei} = 300 \text{ s}^{-1}$ and $D_a = 0.1 \text{ m}^2/\text{s}$, respectively.

Furthermore, the characteristic time scale of the SSS relaxation $\tau^1 = (a_{\perp}^{sss})^2 / D_a \simeq 0.4 \text{ s}$ since the typical spatial scale of Bernstein waves is $a_{\perp}^{sss} = 0.2 \text{ m}$. The value $\tau^{(1)}$ is consistent with the relaxation time of BUM that is less than 1 s detected from our experiments (see Table 2.2).

The experimental observations verify that striations of various length scales are being excited; there remains a question as to why their features, either from the SEE or STEC observations, exhibit hysteresis under a frequency sweep. The persistence of striations through cycles of HF heating could provide a mechanism for hysteresis.

We consider next the hysteresis related to the DM. According to Figure 2.8(b), the up sweep frequency has lower amplitude than that of down sweep frequency, obtained at later times. A possible explanation can be that the system memory is long enough; thus, when revisiting the same heating frequency, some striations still exist and combined with the newly born striations magnify the SEE. Norin et al. [33] estimated the transverse length of the striations involved in generation of the DM, as 730 m. Their relaxation time is $\tau^{(2)} = (a_{\perp}^{DM})^2 / D_a > 500 \text{ s}$. Thus, the ambipolar diffusion in our experiment cannot wash out the striations in 300 s (see Table 2.2), which could cause the DM-related hysteresis.

We consider next the hysteresis related to the BUM. According to Figure 2.8(a), the up sweep frequency has higher amplitude than that of down sweep frequency, obtained at later times. This requires different mechanism than above for the DM hysteresis. We suggest that the BUM-related hysteresis is due to the large scale striations that are scattering the pumping HF waves. The system memory is long enough; thus, those striations will survive during the time between two consecutive frequency sweeps.

We can estimate these effects following a similar process to Gurevich et al. [34] starting from the scattering off a rough surface. The power scattered in a solid angle is given by

$$P/P_0 = \int f_{dif} d\Omega \simeq \frac{16\pi^2 a_{\perp}^2}{\lambda^2} \left(\frac{\Delta n_e}{n_e} \right)^2 \quad (2.8)$$

Figure 2.8(a) shows that the BUM hysteresis produces 2-3 dB of the amplitude reduction on the difference between the up and down frequency sweeps. Assuming linear dependence of the SEE amplitude from the amplitude of the pumping wave, we find that

$$\frac{a_{\perp}}{\lambda} \frac{\Delta n_e}{n_e} \simeq 0.5 - 0.6 \quad (2.9)$$

Consider that an average density perturbation due to HF heating is about a few percent and that the wavelength of the pump wave is 50 m, we find that the most scattering effect is due to the long-scale striations having λ of the order of 1 km. Moreover, the ambipolar diffusion time for these kilometer-scale striations is ≈ 1500 s, which is much longer than our hysteresis time scale for the BUM.

2.5 Conclusion

The key correlation that we noted in these experiments relates these various features

1. DM correlates with a weak to moderate STEC fluctuations (Figure 2.5) and with compact F layer (Figure 2.6(a)).
2. BUM correlates with a strong STEC fluctuations (Figure 2.5) and with spread F layer (Figure 2.6(b)).

In the first case, the DM indicates that no SSS are formed, while in the second case, the BUM indicates the formation of SSS through the four wave process followed by generation of strong turbulence. It is expected that the strong turbulence leads to the electron acceleration that ionizes the neutral atmosphere and thus forms the spread F.

This is similar to the phenomenon known as descending artificial ionized layer (DAIL) [35] that begins with the strong Langmuir turbulence; pumped by HF heating, the turbulence accelerates electrons that in turn form new ionized layers below the original [36]. In this multi-step process, the DAIL starting from 200 to 210 km descends to 150 to 130 km height. In fact, ionograms made during the DAIL appearance show spread F gradually descending to the low altitudes [35]. However, DAIL is formed only when the HF beam is directed along the magnetic zenith and the beam intersects the newly ionized layer, perturbing it, and producing additional hot electrons. In our observations, the beam was 20 off magnetic zenith (MZ); thus,

we see the initial ionization, or starter of the DAIL, but the ionized region cannot propagate downward as it is not intersected by the HF beam.

In conclusion, two different diagnostic techniques, one measuring the differential phase of GPS signals, while another measuring the SEE response, were used simultaneously to study small-scale striations generated by the HAARP heater. These diagnostics were complemented by ionograms and UHF radar data.

We found that:

1. In all cases that were examined, STEC begins fluctuating at the period of heating cycles (20 s) within $\approx 30 - 35$ s after heating commences.
2. STEC measurements indicate that density perturbations vary from 5% below gyroresonance, to 20–30% above, when BUM appears. Such striations can also affect UHF signals including GPS communications, and thus can be important in other applications.
3. Ionograms indicate that the presence of a BUM in the SEE spectrum is associated with strong ionospheric turbulence.
4. Of the six experiments performed, three have been examined in close detail, and all three indicated the presence of strong turbulence, similar to that observed in DAIL experiments [35] This turbulence is capable of accelerating bulk electrons, and in one of the experiments, the presence of these fast electrons was confirmed by MUIR.
5. We detected hysteresis and found that it is different for the BUM and the DM

frequency ranges, indicating that the hysteresis may have two distinct mechanisms. We propose that the DM hysteresis is caused by persistent medium-scale striations (730 m) which combine with the newly excited striations to amplify the SEE. By contrast, the BUM hysteresis is due to persistent larger scale (km) striations which scatter the pump wave, reducing the efficiency of further heating.

Chapter 3: Studies of Ionospheric Turbulence Excited by the Fourth Gyroharmonic

3.1 Introduction

The study of Artificial Ionospheric Turbulence (AIT) generated by high-frequency (HF) heating facilities such as EISCAT and the High-frequency Active Auroral Research Program (HAARP) has a 40-year history. Diagnostic tools to study AIT included: coherent and incoherent scattering radars to detect the formation and propagation of artificial striations, ground based electromagnetic receivers to detect Stimulated Electromagnetic Emission (SEE), scintillations of GPS signal, and detection of narrow band electromagnetic emissions via radio telescopes. At the Sura facility, Ponomarenko et al. [37], utilized a distant broadcast station as radar while the scattered signal was received and analyzed by the UTR-2 HF Kharkov Telescope. They found that when the heating frequency exceeded a multiple of the electron gyro resonance the scattered signal underwent strong broadening (5-10 Hz), and connected it to the excitation of Super Small Striations (SSS). The experiment stimulated theoretical studies which led to the development of the SSS model [24].

Bernhardt et al. [26, 27], Carozzi et al. [31], Thidé et al. [38] and Norin et al. [33, 39], used SEE to probe the AIT. The broadband SEE spectra include features such as the downshifted maximum (DM) and broad upshifted maximum (BUM), both of which are indicators of the processes which occur in the ionospheric plasma during HF heating [40, 41, 42, 43]. The DM is thought to be a signature of the parametric decay of a mode converted upper hybrid wave into another upper hybrid wave and a lower hybrid wave, while the BUM is thought to be produced by a four-wave interaction that includes upper and lower hybrid, as well as electron Bernstein modes. Recently, Bernhardt et al. [26] and Mahmoudian et al. [44] have used the narrow band SEE to estimate the bulk electron temperature while Najmi et al. [45] correlated SEE measurements with analysis of GPS signals and found that the excitation of SSS coincided with the highest amplitude BUM. Additionally, Zalizovski et al. [46] performed O-mode heating at the EISCAT heater and were able to detect HF signals at the Ukrainian Antarctic Station (UAS) located 16.3 Mm away.

We report the results of experiments conducted during the HAARP June 2014 campaign, whose objective was to study the development of artificial ionospheric turbulence. Data collected from different diagnostic tools were analyzed, and the main features detected in the experiments are discussed and explained. In section 3.2, we give an overview of the experiments including the location, timing, and heating patterns. In section 3.3, we present experimental observations and diagnostics including measurements of phase-derived Slant Total Electron Content (STEC) using the L_1 and L_2 GPS signals received at HAARP; measurements of SEE conducted 15 km

away from the HAARP site; ionograms from the HAARP digisonde, reflectance data from the Kodiak radar and detection of the HAARP HF radiation scattered into the ionospheric channel and propagated to the receiver at the UAS in the Antarctic Peninsula. In section 3.4, we present a discussion of the integrated experimental results relating to the nonlinear mechanisms of pumping AIT. Finally, in section 3.5 we give our concluding remarks.

3.2 Description of Experiments

We report below observations from two daytime experiments conducted in June 6 and 7 2014, during the HAARP BRIOCHE campaign. The HAARP heater operated in the 0.9-3.6 MW, power range and used O-mode polarization. The HF frequency selected near the 4th gyroharmonic, was stepped up from 5.67 to 5.94 MHz, subject to constraints of the authorized bands during the experiment, in 30 kHz increments. The HAARP antenna array consisting of 360 crossed dipoles each fed by a 10 kW transmitter produced a total effective radiated power (ERP) of approximately 2.5 GW. Figure 3.1 is a schematic of the experiment, with two of ten heating cycles shown. The heating at each frequency lasted 100 s, with 20 s interpulse period, during which time an ionogram was made. Heating consisted of 10 power steps of 10 s each. The power per transmitter at each of the steps was: 2.50, 3.33, 4.17, 5.0, 5.83, 6.67, 7.5, 8.33, 9.17 and 10.0 kW, with 20 s off. In addition after the 2nd, 5th, and 7th heating cycle the heating beam direction was adjusted to track the path of the moving PRN25 GPS satellite.

The HF beam was directed toward the USA-213 GPS satellite broadcasting the PRN 25 signal, which is in a nearly circular geocentric orbit with inclination 55.0° to the equator, and radius 20.46 Mm. During the experiment, PRN 25 flew over the HAARP site daily, and the signals at both the L_1 ($f_1 = 1.575$ GHz) and L_2 ($f_2 = 1.227$ GHz) were measured on the ground at HAARP after traversing the HF heated region at 1 Hz sampling rate. As discussed in detail in Najmi et al. [45], the measured differential carrier phase was used to estimate the relative STEC. To increase the observational time from 10 min per flyover as in our 2013 experiments to 20 minutes, we adjusted the heating beam direction toward the moving PRN 25 every 5 minutes, illustrated in figure 3.2. The corresponding zenith and azimuth angles are listed in Table 3.1. SEE signals were measured simultaneously using an HF detector operated by the Naval Research Laboratory 15 km away from the HAARP site. The data acquisition techniques have been previously described by Bernhardt et al. [26, 27].

We implemented a new diagnostic technique during this campaign. The HF signals radiated by HAARP were scattered into the ionospheric waveguide by the excited artificial irregularities. This waveguide is formed between the electron density peaks of the E-region and F-region, and since the channel is above the E-region, it is nearly collisionless, and waves in the channel are subjected to low attenuation, allowing them to be channeled to very long distances. The signal trapping and channeling is described by Erukhimov et al. [47] and is believed to be the mechanism of very long distance propagation of EISCAT heater signals previously observed by Zalizovski et al. [46]. At the time of the experiment, the waveguide was oriented along

the Earth's terminator and simultaneously passing over both the transmitting and receiving sites. These signals were detected on the ground at the UAS (coordinates 65.25° S, 64.25° W) 15.6 Mm away from HAARP. The HF signals were recorded within a 500 Hz frequency band centered at the carrier frequency of the HAARP signal. The data acquisition system collected records of the intensity and the Doppler spectra of the signal with time resolution 1 s and 5 s. This chapter introduces a method to use the effect of long distance HF propagation for diagnostic of the AIT spectra. All the experiments were diagnosed by the HAARP ionosonde, and by the Kodiak coherent radar located 670 km SW of HAARP.

Table 3.1: Summary of Experiment beam angles. The listed initial zenith and azimuth angles are updated every five minutes to track the path of PRN 25.

Date	Start	End	Init.	+5 min	+10 min	+15 min
06/06/14	02:55	03:15	$15.8^\circ, 220.9^\circ$	$16.1^\circ, 212.2^\circ$	$16.8^\circ, 204.1^\circ$	$17.4^\circ, 199.6^\circ$
06/07/14	02:50	03:10	$15.8^\circ, 222.4^\circ$	$16.0^\circ, 213.6^\circ$	$16.7^\circ, 205.4^\circ$	$17.2^\circ, 200.8^\circ$

3.3 Experimental Observations

Each of the two experiments discussed here lasted 20 minutes, starting at about 03:00 UT, i.e 7 p.m. local time. During the first day (06/06/14) the ionosphere was slightly disturbed ($\delta B \approx 50$ nT); a noticeable sporadic E-layer existed ($f_0E_s \approx 4.5$ MHz); f_0F_2 was in the frequency range 5.6-5.7 MHz while the F_2

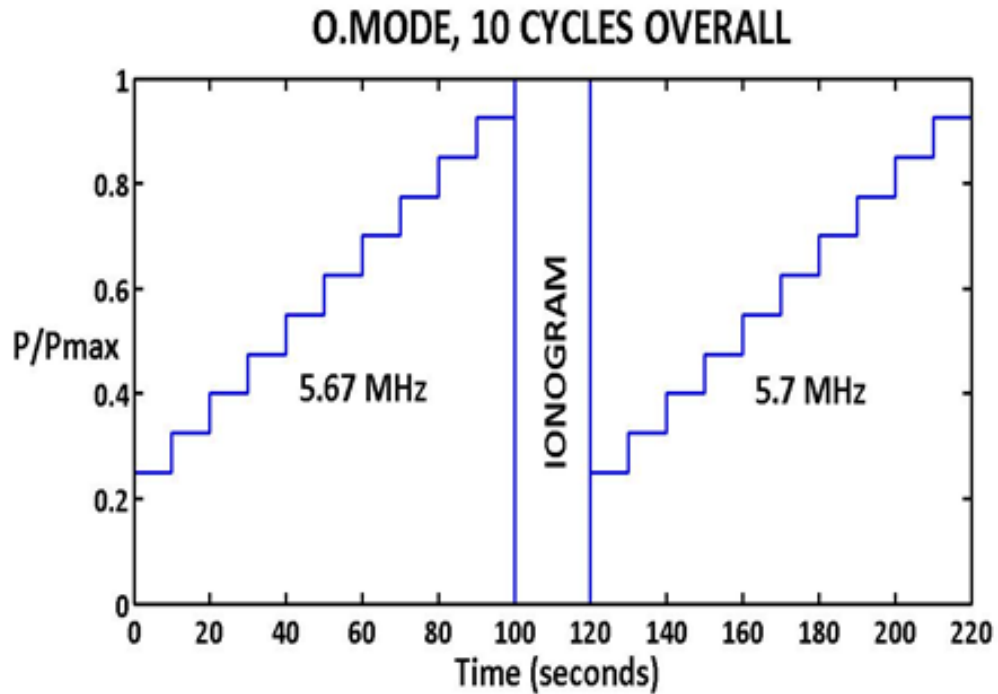


Figure 3.1: Schematic of HF heating. The HAARP heater operated in the 0.9-3.6 MW, power range, used O-mode heating. The HF frequency was near the 4th gyroharmonic, and was stepped up from 5.67 to 5.94 MHz in 30 kHz increments. Here two of ten heating cycles are shown. The heating at each frequency lasted 100 s, with 20 s interpulse period, during which time an ionogram was made. Heating consisted of 10 power steps of 10 s each. The power per transmitter up from 2.5 kW to 10 kW with 0.83 kW incremental.

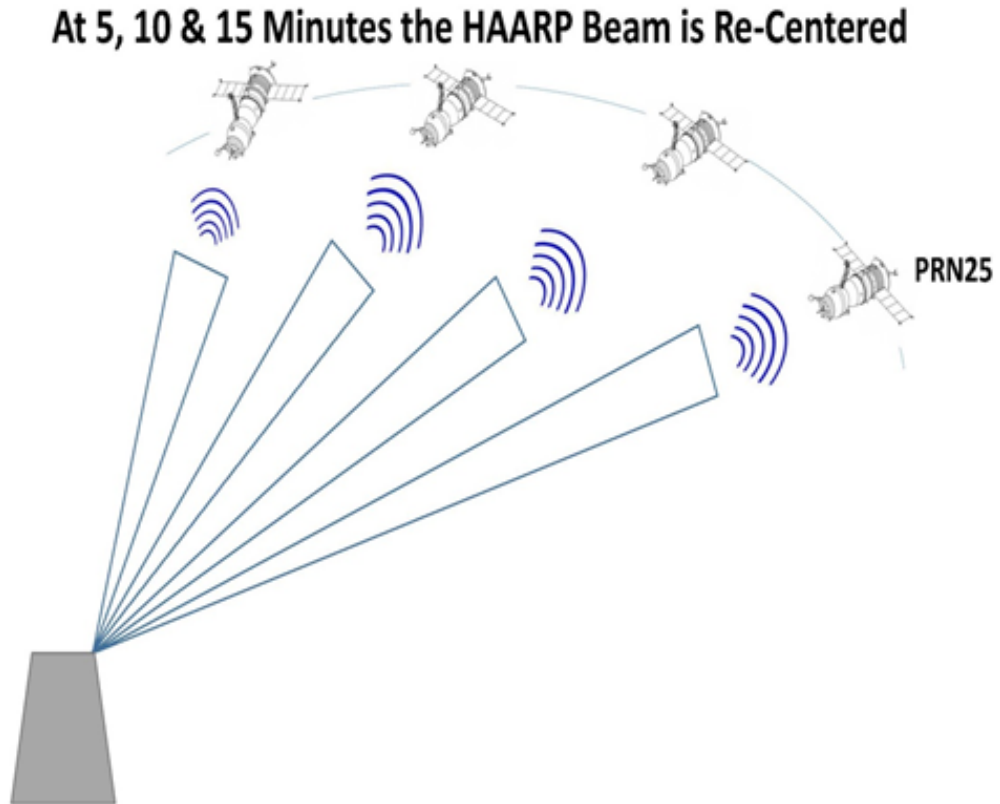


Figure 3.2: The HF beam was directed toward the PRN GPS 25 satellite on a geocentric orbit. To increase the observational time we adjusted the heating beam direction toward the moving PRN 25 every 5 minutes. The corresponding zenith and azimuthal angles are listed in Table 1

peak was located at $h_m F_2 = 270$ km. Considering the oblique propagation of the heating wave, its frequency was reflected from the F_2 peak, thus, for the majority of the experiment, the heating wave was strongly absorbed in the ionosphere due to anomalous absorption. An exception was the time around 3:04 UT when the ionogram revealed that $f_o F_2$ dropped below 5.4 MHz, so that the heating frequency exceeded the critical frequency, and the ionosphere became transparent to the HF wave. During the second day (06/07/14) the ionosphere was also quiet ($\delta B \approx 30$ nT) with E_s layer present. However, the ionosphere was unstable. Fully half of the ionograms show that the $f_o F_2$ fell to 4.05-4.5 MHz, resulting in low absorption and absence of any heater generated AIT. The remaining ionograms show $f_o F_2 > 5.7$ MHz and $h_m F_2 = 270$ km, and resulted in some AIT excitation.

Due to federal regulatory frequency constraints, the minimum heating frequency was 5.67 MHz which was above the 4th gyro resonance. In our March 2013 experiment [45] we obtained the resonance frequency 5.76 MHz from the SEE spectrum, at which frequency the DM disappeared. Concurrent ionograms show that 5.76 MHz waves are reflected at an altitude of 190 km. An estimate based on the dipole model of the geomagnetic field shows that in the June 2014 experiments the 4th gyro resonance occurs at 5.6 MHz, with $5.6 \approx 4f_{ce} = f_{pump} \left(\frac{R_e + 190}{R_e + 250} \right)^3$, where $f_{pump} = 5.76$ MHz, and $R_e = 6371$ is the Earth radius in km. 190 km represents the reflection altitude at f_{pump} during our previous experiments, and 250 km is the reflection altitude of 5.6 MHz waves shown in ionograms taken from the June 2014 campaign. Thus the lowest heating frequency of 5.76 MHz is close to, but above the BUM cutoff of 5.68 MHz estimated by Leyser et al. [42].

3.3.1 GPS Observations

Data collected by the HAARP GPS detector during HF heating experiments on June 6th and 7th are presented in figures 3.3 and 3.4. Figures 3.3(a) and 3.3(b) show STEC data in Total Electron Content Units (TECU) during heating experiments with heater on-off times indicated by solid vertical lines, as a function of the elapsed time and heating frequency on June 6th (figure 3.3(a)) and June 7th (figure 3.3(b)). The heating at each frequency lasted 100 s while each 10 s the power was stepped up. As a result, figure 3.3 shows STEC amplitude as a function of heating power for each of the heating frequencies. The STEC amplitude immediately increases after the heater is turned on, but after several seconds, the amplitude decays. There is additional snap-back after the heater is turned off. The mechanism for this behavior is discussed in detail in section 3.4.

Figure 3.4 shows the scintillation index (S_4) of the L_1 and L_2 Carrier-Noise-Ratio (CNR) on June 6th (figure 3.4(a)) and June 7th (figure 3.4(b)). Heater on-off times are indicated by solid vertical lines. Although we collect CNR, we assume that in our frequency range noise does not change greatly over our S_4 intervals, and thus the CNR is proportional to the signal intensity. In figure 3.4 the highest values of the S_4 index were detected between 900 and 1100 s into the heating for both L_1 and L_2 corresponding to frequencies near 5.88-5.91 MHz. The extrema of the S_4 index are known to correspond to changes in the length scale of the underlying physical processes [48]. The mechanism of the change in length scales is discussed in section 3.4.

3.3.2 SEE Observations

Stimulated Electromagnetic Emission (SEE) signals were measured simultaneously with the STEC using an HF detector operated by the Naval Research Laboratory 15 km away from the HAARP site and shown in Figures 3.5, 3.6, and 3.7. Figure 3.5 shows the power spectral density (PSD) of the SEE emission at the selected frequency 5.76 MHz. The traces are averaged over a 10 s portion of the heating period with constant ERP. The heating frequency is shown by the highest peak in the center at $\Delta f = 0$, the down-shifted maximum (DM) is on the left side of the heating frequency at $\Delta f = -10$ kHz, while the broad up-shifted maximum (BUM) is on the right side of the plots in the range $\Delta f = 50 - 150$ kHz. Each are indicated by arrows. The blue trace corresponds to the per transmitter power of 2.5 kW, green to 5.0 kW, and red to 10 kW (25, 50, and 100% respectively). We see that the peak amplitude of the SEE signal is saturated at 50% power.

In figures 3.6 and 3.7, the traces are independently normalized, but typically the intensity of the DM is comparable to the BUM at frequencies close to the gyroresonance and up to 25 dB stronger than the BUM at higher frequencies. Figure 3.6 shows the amplitude of the DM and BUM as a function of the pump frequency. The red and blue traces in figure 3.6 show the amplitude of the BUM and DM respectively, both normalized by their peak values. The BUM reaches its peak at $f_h = 5.67$ MHz which is close to the BUM cutoff, and reduces with f_h . The DM reaches its peak at $f_h = 5.79$ MHz, stays at nearly its maximum amplitude up to 5.85 MHz, and then rolls off for $f_h > 5.85$ MHz. The amplitude of the BUM is

observed to decay by ≈ 10 dB / 100 kHz while the DM both initially increases by ≈ 12 dB / 100 kHz, saturates, then decays at 12 dB / 100 kHz. Figure 3.7 shows the amplitude of the PSDs normalized by their peak value as a function of the heating power for frequencies 5.67 (figure 3.7(a)) and 5.79 (figure 3.7(b)) MHz. These frequencies were chosen to demonstrate the strongest values of the BUM and DM amplitude. For both the DM and the BUM, we see 90% saturation occurs by 50% of full power.

3.3.3 Kodiak Radar Observations

Figure 3.8 shows data measured by the Kodiak radar during the experiments on June 6th. Top trace shows the SNR time series of the Kodiak radar backscattered signals. Beam 9 of the radar was directed towards the heated region at frequency of about 12 MHz. The signal reflected by the AIT is centered at 700 km slant range. During the 10th cycle at 03:12:00-03:14:30, the SNR was strongly reduced because the Kodiak beam 09 was almost outside of the HF heating spot. This was a geometric effect of the angular adjustments of the beam to track PRN 25 and this final heating cycle was picked up by beam 10. The HF heating was switched on at 02:55 followed by the buildup of the reflected radar signal over 25 s. Then a strong SNR of more than 50 dB was detected. The reflection increased by ≈ 10 dB around 02:57 then reduced around 03:00 and 03:04 due to decrease in the ionospheric plasma density. The second dip was discussed above in section 3.3, while the first dip occurred at a time not covered by the ionograms at HAARP. Between 03:11:30 and 03:13:30

the SNR decreased, and at 03:14:30 the heater was switched off and the reflection gradually disappeared. The lower plot shows time series of the velocity of the ionospheric irregularities. Starting at 02:55:00, the irregularities quickly accelerate to 35-40 m/s, peak at ≈ 60 m/s near 02:57:00-02:59:00, when the heating frequency $f_h = 5.70$ MHz was close to the value of $f_O F_2$ obtained from ionograms and the double resonance, where the pump frequency matches both the local upper hybrid frequency and an integer multiple of the electron cyclotron frequency, condition was fulfilled, then gradually reduces to ≈ 30 m/s at later times. During June 7th, radar reflection was weak and is not shown.

3.3.4 UAS Signal Observations

Monitoring of the HAARP HF signals was carried out at the UAS Academician Vernadsky. Figure 3.9(a) and 3.9(b) show the spectrogram of the received signal for June 6th and June 7th, while figure 3.10 shows the signal-to-noise-ratio of the signal as a function of time detected on June 6th. The 8th ($f_h = 5850$ kHz) and 9th ($f_h = 5910$ kHz) heating cycles, indicated by black arrows at the spectrograms, were contaminated by interference signals and therefore were not processed in figure 3.10. The blue trace shows the measured data while the red trace is the 10s moving average. The intensity of detected signal strongly depends on the heating frequency f_h . For f_h slightly above the 4th gyro-frequency the intensity of the detected signal was very low, barely above the noise level. The intensity of the detected signal increased with f_h and peaks at 5.79 MHz. We were unable to detect scattered HAARP

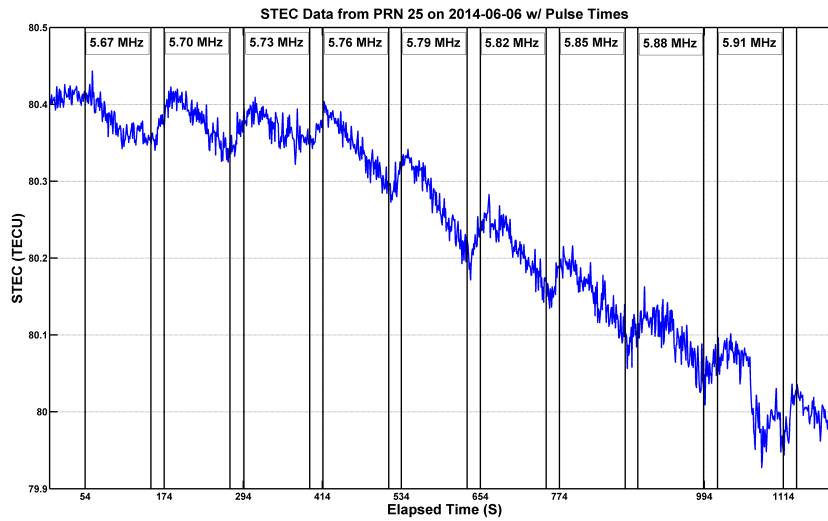
HF signals from similar detectors in Ukraine and Scandinavia, thus verifying the role played by Earth's terminator in the formation of the waveguide. Figure 3.11 shows that for frequencies 5.67-5.73 MHz, the signal intensity is approximately linear in HAARPs ERP, where for frequencies 5.76-5.88 MHz the signal intensity is nonlinear. The blue trace in figure 3.11 shows the time dependent received signal intensity, the red trace shows the linear fit, and the green trace shows a reference linear fit with a four times increase in the received signal. Similar results were obtained on June 7 except that the signal-to-noise ratio was by 5-10 dB less than that on June 6 (see figures 3.9(a) and 3.9(b)). In figure 3.12, we show a close-up of the received signal at two different frequencies, in blue, 5.70 MHz where the received signal is linear in HAARPs ERP, and in red, 5.79 MHz, where the received signal is non-linear. The error bars are the standard deviation of the mean of the SNR detected at UAS.

The spectral width as a function of the heating frequency is shown in figure 3.13 for each of 100 s time interval which correspond to the heating by a chosen frequency on June 6th. The spectral width at half power was obtained by using smoothed spectral curves, and the average spectral width is 1.1 Hz, and in all cases is below 1.5 Hz. Finally, figure 3.14 presents the S_4 scintillation index as a function of the heating frequency over each 100 s time interval. The extrema of the S_4 index are known to indicate changes in the scales of the underlying causes of turbulence, and the first peak at $f_h = 5.73$ MHz corresponds to when the SSS, indicated by the BUM (see figure 3.6), begin to be suppressed by the longer scale striations indicated by the presence of the DM which can scatter the HF waves. The second peak at 5.82 MHz is isolated due to signal interference, and it is not

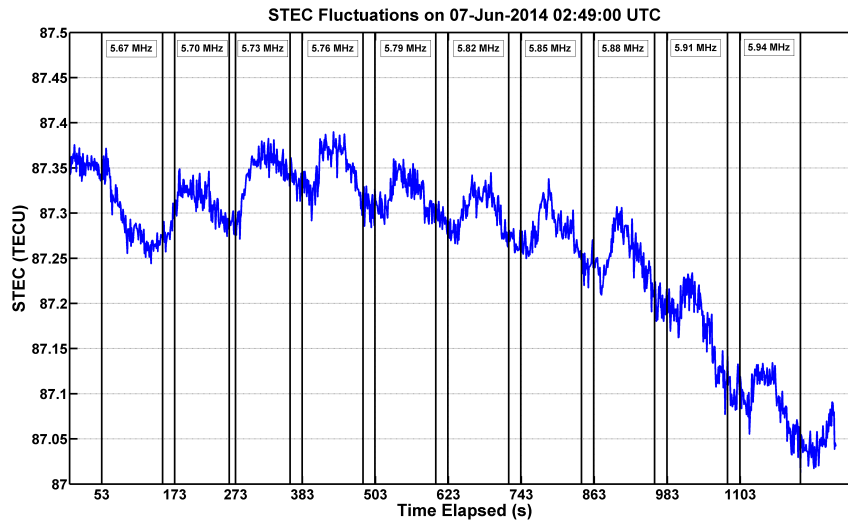
clear if it is a local extrema, but we speculate that it is both a local extrema and that it corresponds to the pump frequency at which dekameter scale striations are no longer efficiently excited.

3.4 Discussion

The main features detected in the experiments including theoretical considerations are discussed below. In figure 3.3, we showed the dependence of the STEC amplitude in TECU with radiated HF power for the June 6th and June 7th experiments. We expected that the STEC amplitude would increase with ERP because larger ERP can lead to production of additional SSS which modulate the GPS signal. Instead, we found that the STEC amplitude initially increased with HF power, but then at each frequency it decayed with power for power levels above $\approx 40\text{-}50\%$. A possible explanation for the nonlinear effect in the STEC amplitude is a competition between processes that form SSS, which modulate the GPS signal, and those that form dekameter scale striations which control the anomalous absorption and are detected by Kodiak. A competition between process that form different scale striations was observed by Frolov et al. [49] when probing the region of the ionosphere heated by the Sura facility with two radars of different frequencies. The radars detected the temporal evolution of striations of size 3 and 13 m perpendicular to the geomagnetic field. The 3 m scale striations experienced fast rise, reaching a peak in 3 s, and then become suppressed by the rising 13 m scale striations, which gradually saturate over about 10 s.

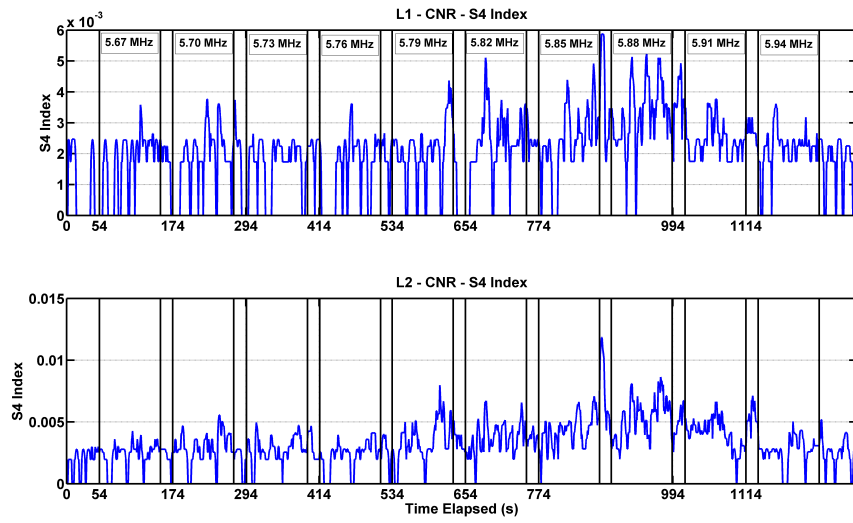


(a)

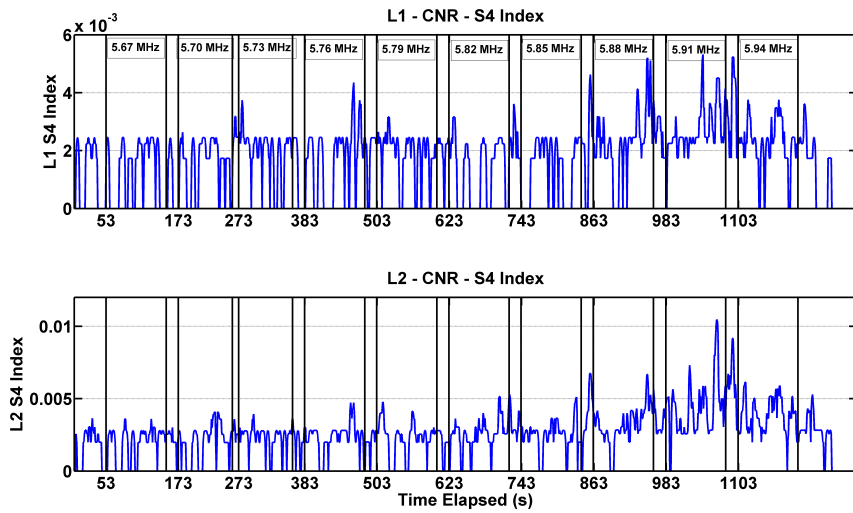


(b)

Figure 3.3: STEC data (in TECU) during heating experiments on June 6th (a) and June 7th (b) with heated on-off times indicated by solid vertical lines. The heater is first turned on around 20s (a) and 50 s (b) elapsed. Since the heating at each frequency lasted 100 s and each 10s the power was stepped up, the figure reveals STEC amplitude vs. power for each of the heating frequencies.



(a)



(b)

Figure 3.4: Scintillation index S_4 of the L_1 and L_2 Carrier-Noise-Ratio (CNR) vs. time elapsed and heating frequency on (a) June 6th and (b) June 7th. Heater on-off times indicated by solid vertical lines.

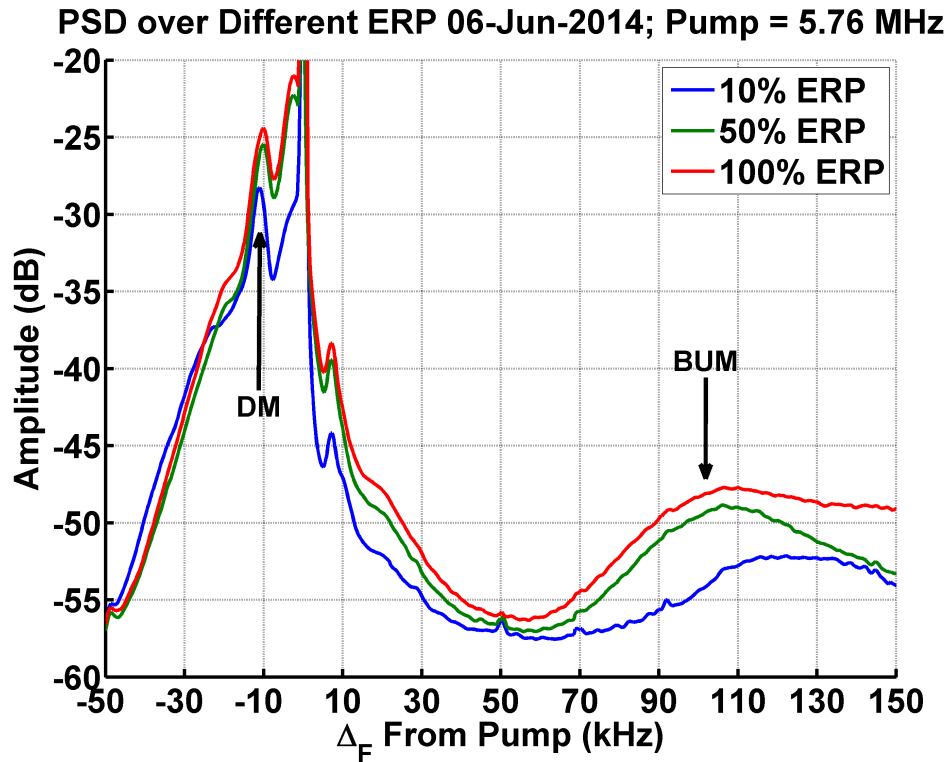


Figure 3.5: Power spectral densities (PSD) of broadband SEE from 06-Jun-2014 computed for the selected frequency 5.76 MHz. The traces are averaged over a 10s portion of the heating period with constant effective radiated power (ERP). The heating frequency is shown by the highest peak in the center at $\Delta F = 0$, the down shifted maximum (DM) is on the left side of the heating frequency while the broad up shifted maximum (BUM) is on the right side of the plots, both are indicated by arrows. The blue trace corresponds to the power 2.5 kW, green to 5.0 kW and red to 10 kW per transmitter (the power level 25, 50, and 100% respectively).

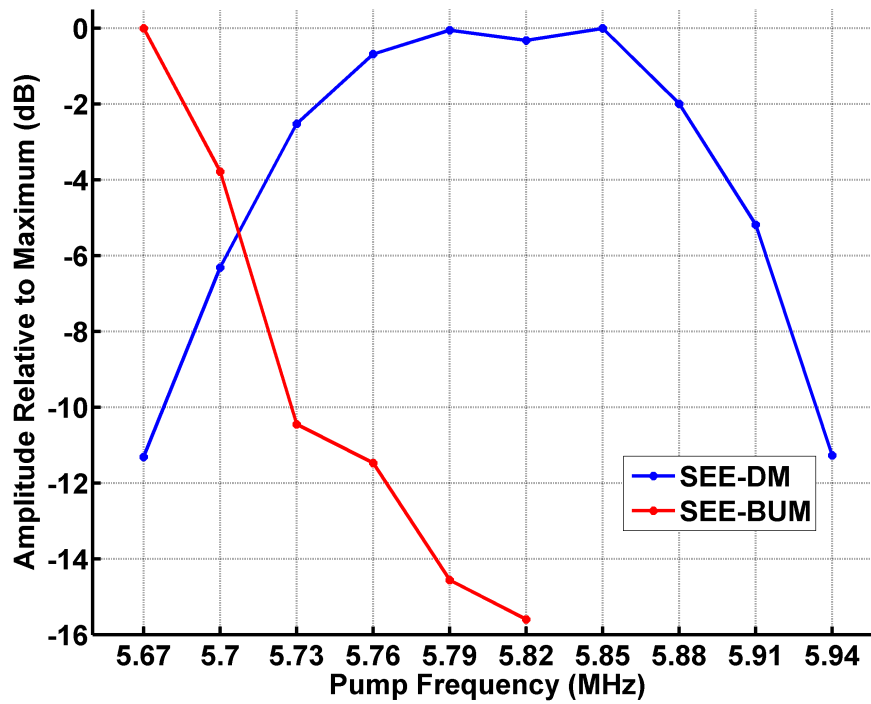
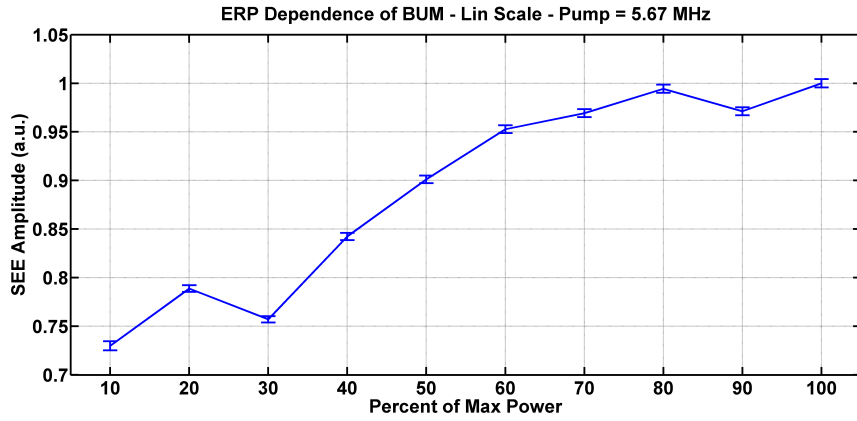
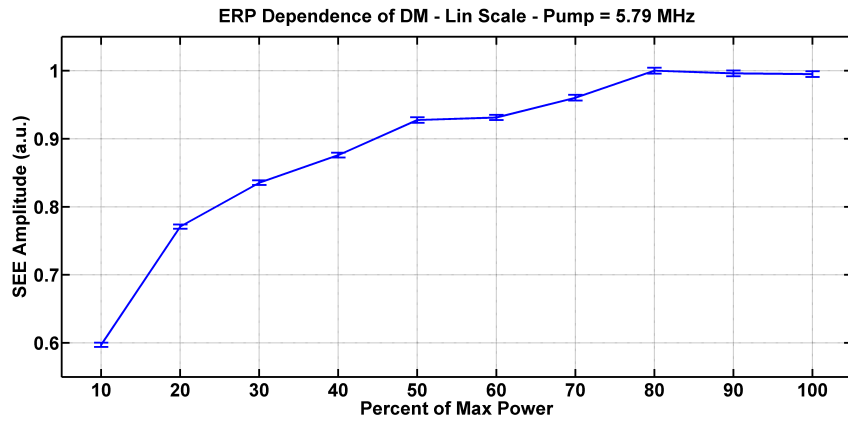


Figure 3.6: The red and blue traces show the amplitude of the BUM and DM respectively, both normalized by their peak values, as a function of the pump frequency.



(a)



(b)

Figure 3.7: BUM (a) and DM (b) amplitude dependence on power. We chose the strongest values of the BUM and DM amplitude which are reached at 5.67 and 5.79 MHz respectively.

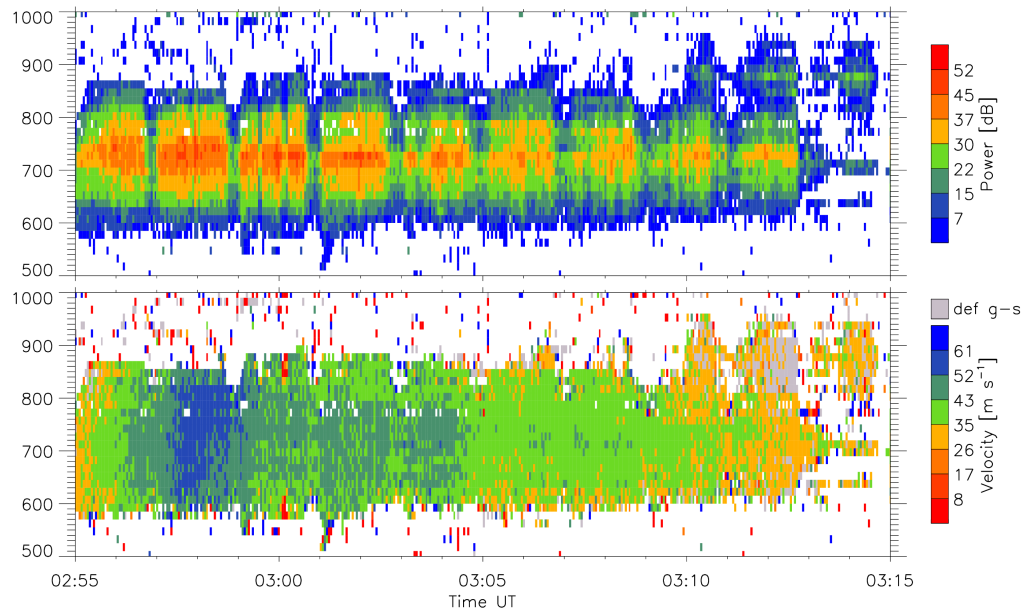
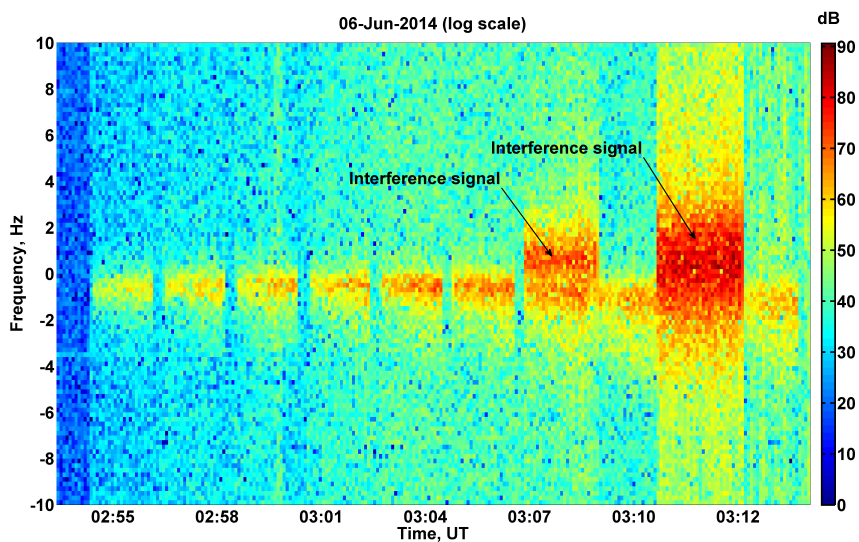
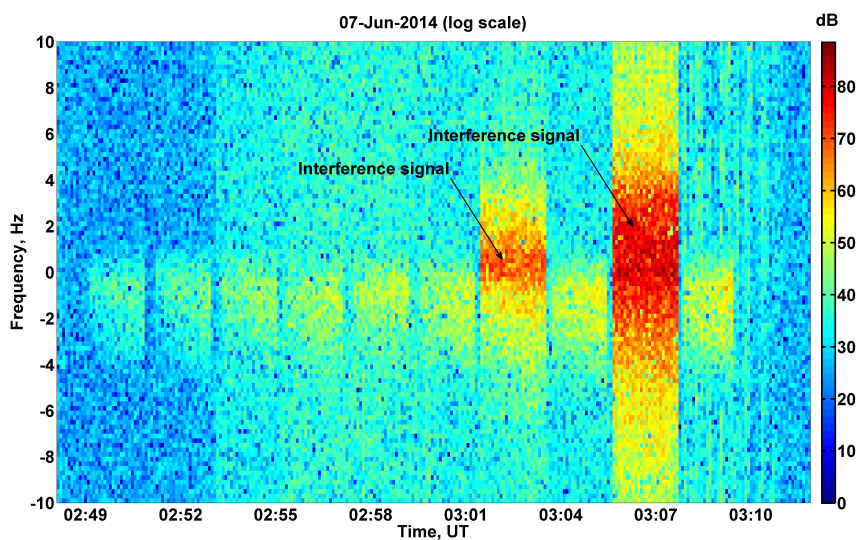


Figure 3.8: Diagnostics from Kodiak Radar Beam 09. Top plot is SNR, lower plot is velocity of plasma irregularities, all detected on June 6th. Slant range is approximate distance from Kodiak to an ionospheric reflector.



(a)



(b)

Figure 3.9: Spectrogram of received HF signal at UAS (a) June 6th, (b) June 7th. The 8th ($f_h = 5850$ kHz) and 9th $f_h = 5910$ kHz heating cycles, indicated by black arrows at the spectrograms, were contaminated by interference signals and therefore not processed.

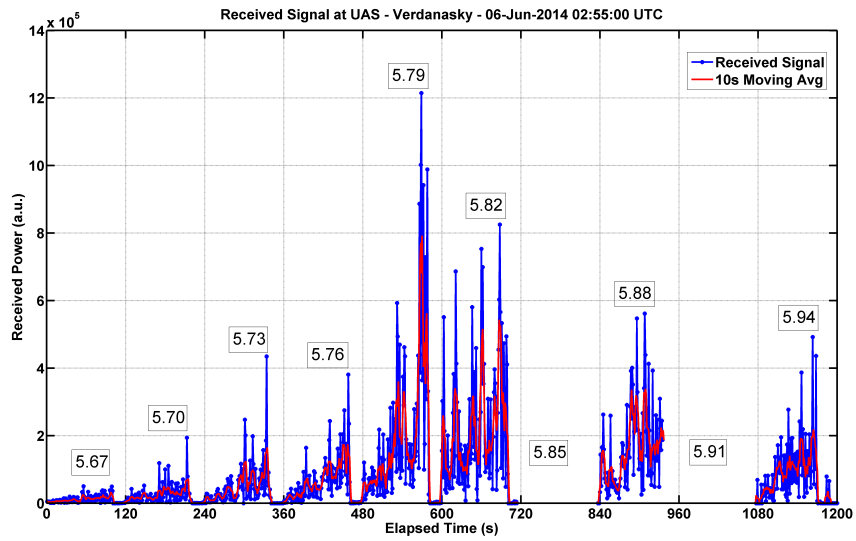


Figure 3.10: Time series of Received Power at UAS on June 6th with HF heating frequencies indicated. The intensity of the HAARP signals at the different heating frequencies is shown by the blue lines with the linear interpolation shown by the red lines.

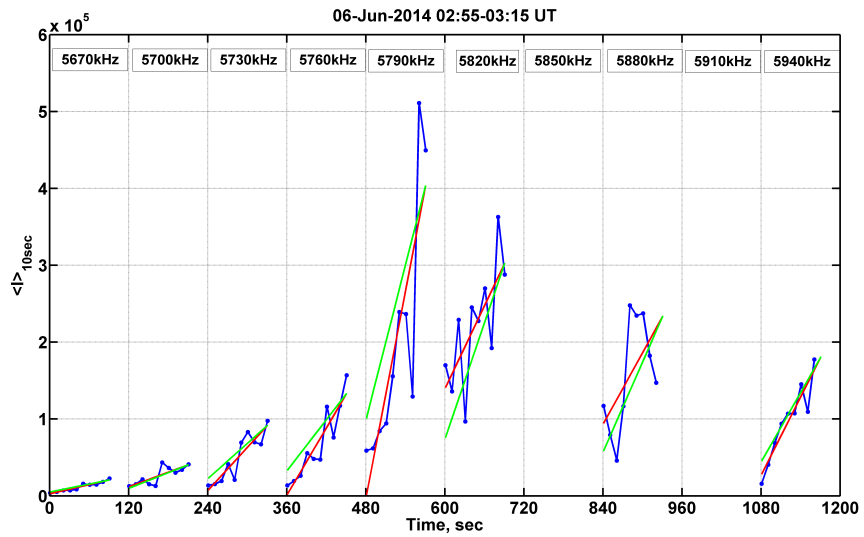


Figure 3.11: Scaling of Received Power at UAS with ERP. The intensity of the received signals at the different heating frequencies is shown by the blue lines. The green lines correspond to 4 times increase of the heating power, with the linear interpolation shown by the red lines.

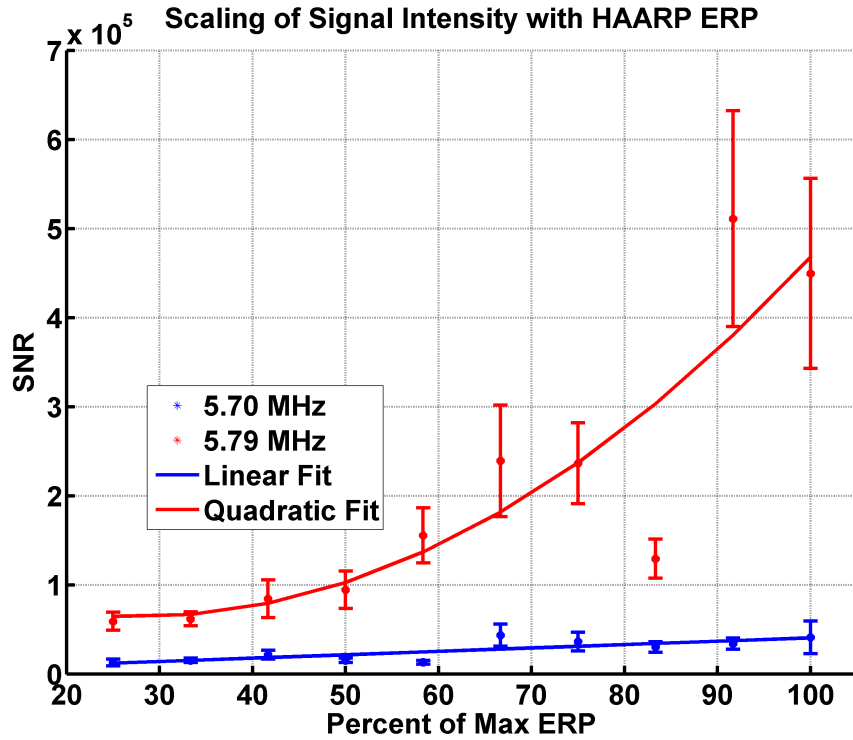


Figure 3.12: Scaling of the Signal-to-noise-ratio at UAS with ERP for two different pump frequencies. In blue, 5.70 MHz which is linear in HAARPs ERP, and in red, 5.79 MHz, which is non-linear in HAARPs ERP. Error bars are the standard deviation of the mean of SNR measured at UAS during heating at the given ERP and frequency.

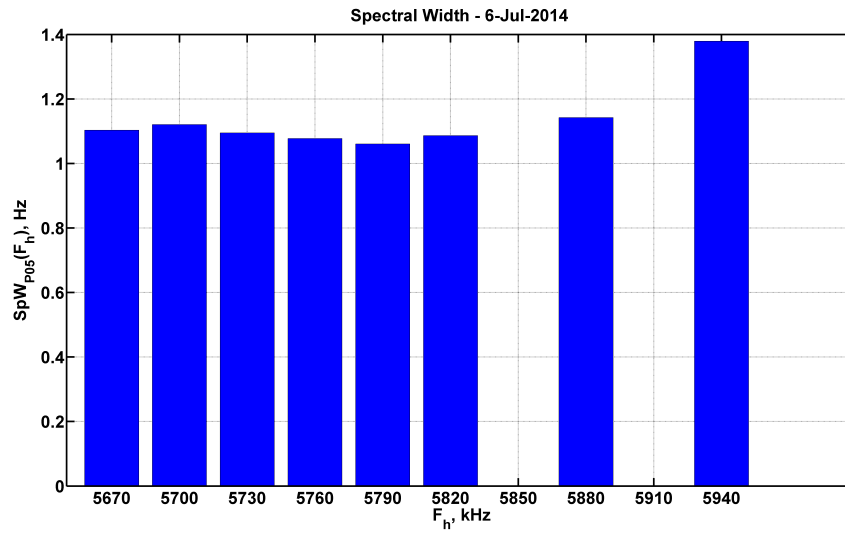


Figure 3.13: Spectral width of received signal at half-max power at UAS vs. heating frequency measured on June 6th.

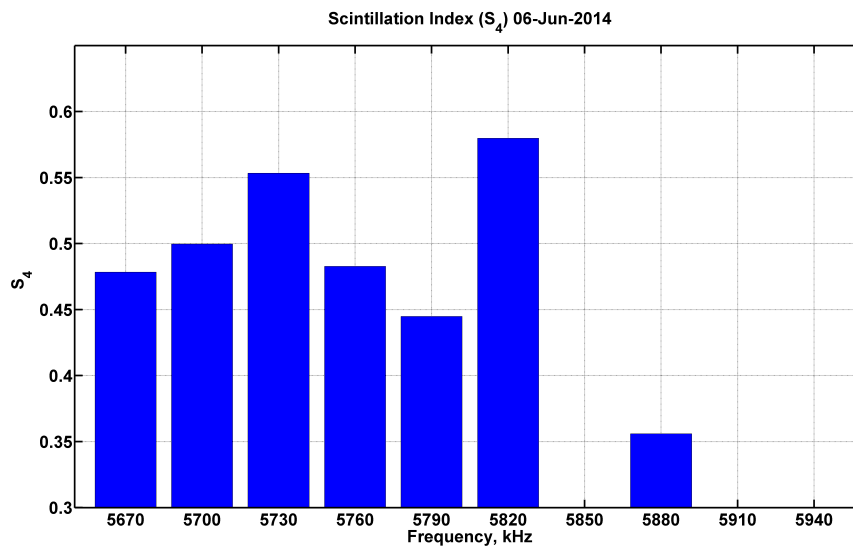


Figure 3.14: Scintillation Index (S₄) of Received Power at UAS as a function of heating frequency measured on June 6th.

Consider the following physical argument as given by Najmi et al. [45]. The STEC value is proportional to the amplitude of super small striations $(\delta n_e/n_e)_{SSS}$ which in turn is proportional to the pumping power P of the heating wave [24].

$$STEC \propto \left(\frac{\delta n_e}{n_e} \right)_{SSS} \propto P \quad (3.1)$$

In the presence of dekameter scale striations produced by anomalous absorption of the heating wave, the pump power is reduced by

$$P = P_0 \exp^{-\beta(\delta n_e/n_e)_{DM}^2} \quad (3.2)$$

where β is a coefficient and $(\delta n_e/n_e)_{DM}$ indicated the magnitude of the dekameter scale striations. Frolov et al. [49] obtained that $(\delta n_e/n_e)_{DM}^2 \propto P$ for striations with scale size close to 10 m, and in our experiments, the pumping power was varied in the range $P_{min} < P < P_{max}$ where P_{max} is the maximum ERP of HAARP. We transitively obtain the following STEC dependence upon the varying power:

$$STEC \propto \frac{P}{P_{max}} \exp^{-\alpha P/P_{max}} \quad (3.3)$$

We found our STEC data fit this product of a linear and exponential function, with the STEC data from June 6th and least-squares fit shown in figure 3.15, and the parameter α is determined from the power that corresponds to the STEC peak value. At the STEC peak, we have $\frac{d}{dP}(STEC) = 0$, thus $\alpha = (P_{peak}/P_{max})^{-1} = (34/100)^{-1} = 2.94$.

A separate effect of interest comes from the SEE observations. In figure 3.16, we show the peak amplitudes of PSDs as a function of the heating frequency f_h .

The BUM amplitude, indicated in red, decays rapidly as f_h increases, while the DM amplitude, shown in blue, rises, saturates, then decays for much larger f_h .

Since the work by Huang and Kuo [43], it is known that the growth rate of the BUM induced instability is $\gamma = 1/\sqrt{f_{UH}^2 - f_{EB}^2}$. Where f_{UH} is the upper hybrid frequency and f_{EB} is the electron Bernstein frequency which for larger wave numbers is a multiple of the electron gyro frequency. We estimate that $\gamma \propto 1/\sqrt{f_h - 4f_{ce}}$ where $f_h > 4f_{ce}$, and since the ionospheric conditions indicate $4f_{ce} = 5.6$ MHz, as the heating frequency increases past the resonance, the growth rate of the BUM related instability is squelched. By contrast, it is known that the DM disappears at a multiple of the electron gyro resonance. The DM amplitude increases when f_h rises above $4f_{ce}$ and eventually saturates [50]. However, at higher frequencies the value f_h could exceed f_oF_2 , thus the ionosphere becomes transparent. Since the HF beam is directed at about 16° to MZ, and the beam has a conical shape some fraction of the beam could be still absorbed while the other become transparent which reduces the overall heating effect, which can explain why we see a decay of the DM amplitude with f_h rather than a sharp cutoff.

Previous work by Carozzi et al. [31], Wagner et al. [51], Frolov et al. [49] have also made SEE observations of heating with varying ERP near the fourth gyroharmonic. Our experiments operated at 10 dBW higher ERP than that available at Sura, and probed a frequency range of 270 kHz, as opposed to 60 kHz at Sura. At Sura, the SEE showed linear dependence of the amplitude of the BUM peak with varying ERP [51] while our experiments showed a nonlinear saturation of both the BUM and DM peaks with varying ERP, this can be seen in figure 3.7. We

estimated $\approx 90\%$ saturation of the DM and BUM amplitudes occurs at $\approx 50\%$ of HAARPs maximum ERP. We also detected the shift of the BUM peak towards lower frequencies at higher ERP. In figure 3.7, the peak of the BUM is seen to shift-down by ≈ 25 kHz as the ERP increases from 25% to 50%, and does not appear to shift further as the ERP is increased to 100%. Neither the saturation of the BUM and DM amplitudes, nor the frequency shift of the BUM peak, are well understood, and are subjects of future studies.

Finally, we discuss and analyze the physical processes underlying the scattering of the HAARP HF waves by the AIT into the ionospheric waveguide. These waves were detected and processed at the UAS located 16.3 Mm from the heater. Previously, Zalizovski et al. [46] detected HF signals from the EISCAT facility at the UAS. The received HF signal had two different components, one was a narrowband mirror-reflected signal, while the other was a scattered signal with a much wider spectrum. Zalizovski et al. [46] found that although both components propagate along the ionospheric channel, the mirror-reflected signal is associated with the side lobe radiation of the transmitting HF antenna, which bypasses the modified volume, while the scattered signal was radiated through the main antenna beam and then scattered by pump-induced plasma striations. In order to establish which of the two mechanisms is dominant one needs to sweep the heating frequency around a multiple of the electron gyro resonance. While the side lobe radiation is not sensitive to small frequency variations, the spectrum of the pumped striations, and thus the scattered signal, strongly depends on f_h .

Figure 3.16 shows amplitudes of PSDs obtained from the SEE spectrum com-

bined with the intensity of the HAARP signal measured at UAS taken from the Doppler spectrum on June 6th (figure 3.11) as a function of the heating frequency. As we discussed above, the red and blue traces in figure 3.16 show the amplitude of the BUM and DM respectively at maximum heater power, both normalized by their peak values. The black trace shows the intensity of the detected HAARP signal at UAS first smoothed by moving average (red trace in figure 3.11) and then normalized by its peak value. All data points are time averages over measurements taken at maximum ERP at the listed frequency, and are normalized independently such that the maximum of each trace maps to 0 dB. The error bars of the black trace are the standard deviation of the mean of the SNR at UAS at maximum heater power. We found that the intensity of the signal detected at UAS during the experiments on June 6th strongly depends on the heating frequency f_h . Figure 3.16 reveals that when the BUM is dominant in the SEE spectrum, it suppresses the HF signal. The stronger the BUM is, the weaker the HF signal. By contrast, when the DM dominates in the SEE spectrum, the intensity of the detected signal increases with f_h and peaks at 5.79 MHz. Thus the DM and HF peaks occur at the same frequency.

Furthermore, it is known that the BUM is associated with the pumping of 10 cm SSS while the DM is associated with the 7-30 m scale striations [33]. Since SSS inefficiently scatter the HF waves compared to the dekameter striations related to the DM, this implies that the HAARP signal detected at UAS could be due to the scattering of HF radiation with half wavelength of 25 m by the dekameter size artificial striations into the ionospheric channel. The Kodiak radar is sensitive to striations in this range, since its half wavelength is ≈ 10 m, and it detected strong

scattering in slant ranges corresponding to the HAARP facility, and simultaneously detected striation velocity of ≈ 30 m/s (shown in figure 3.8). This is consistent with the striation velocity calculated by the Doppler broadening at UAS, that can be seen in figure 3.13, $\Delta f_D = 1.15 - 1.40$ Hz, with corresponding velocity of irregularities $v = \frac{c\Delta f_D}{2f_h} = 30 - 35$ m/s.

The analysis shows that the origin of the signal detected at UAS is scattering of HAARPs HF radiation off of artificially pumped striations and into the ionospheric waveguide. In this process, mirror reflection does not appear to play an important role, as indicated by the low amplitude of received signal at 5.67 and 5.70 MHz. Since the amplitude of the signal varied nonlinearly with the HF power at 5.76, 5.79 and 5.82 MHz, the signal cannot be induced by sidelobe radiation which is known to be linear in the radiated power.

3.5 Conclusions

We have presented a study of the AIT induced at HAARP by sweeping frequencies near the fourth gyro harmonic. Our study included a number of diagnostics, such as: SEE, STEC and Kodiak radar, to both verify the presence of AIT and confirm nonlinear effects related to the variation of the pump intensity and frequency. Moreover, we added the novel diagnostic of received signal at the UAS 15.6Mm away.

The AIT has a broad wavelength spectrum, and within it, we studied striations of the 10 cm (SSS) and dekameter scale. These striations are indicated by the

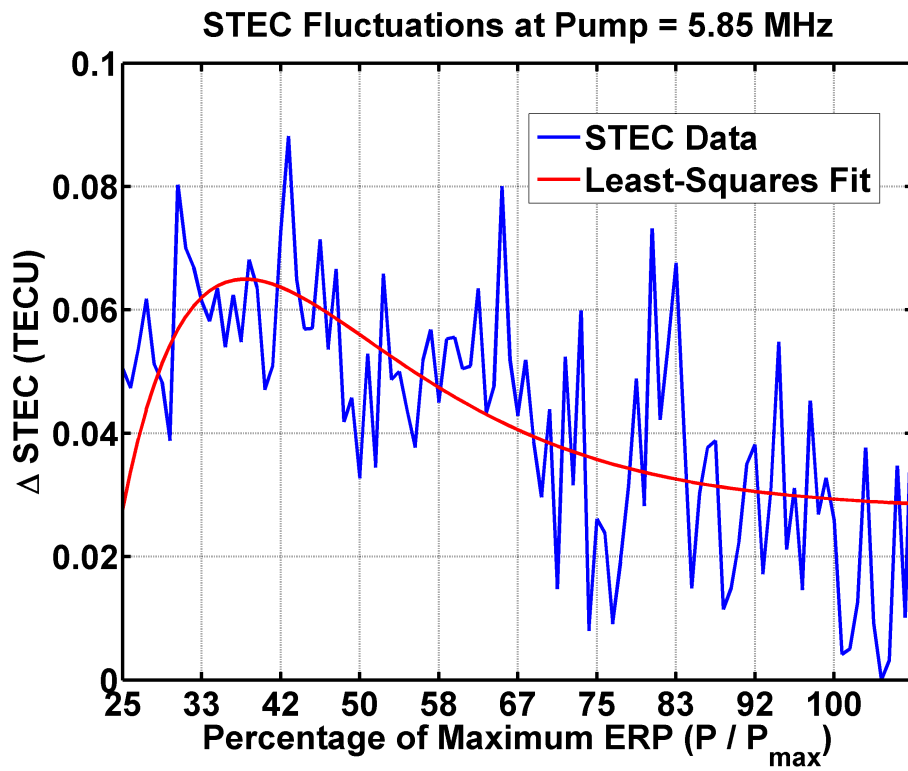


Figure 3.15: STEC fluctuations as a function of ERP with least-squares fit to $x \exp -\alpha x$, where x is the ratio of the HAARP ERP to its maximum ERP.

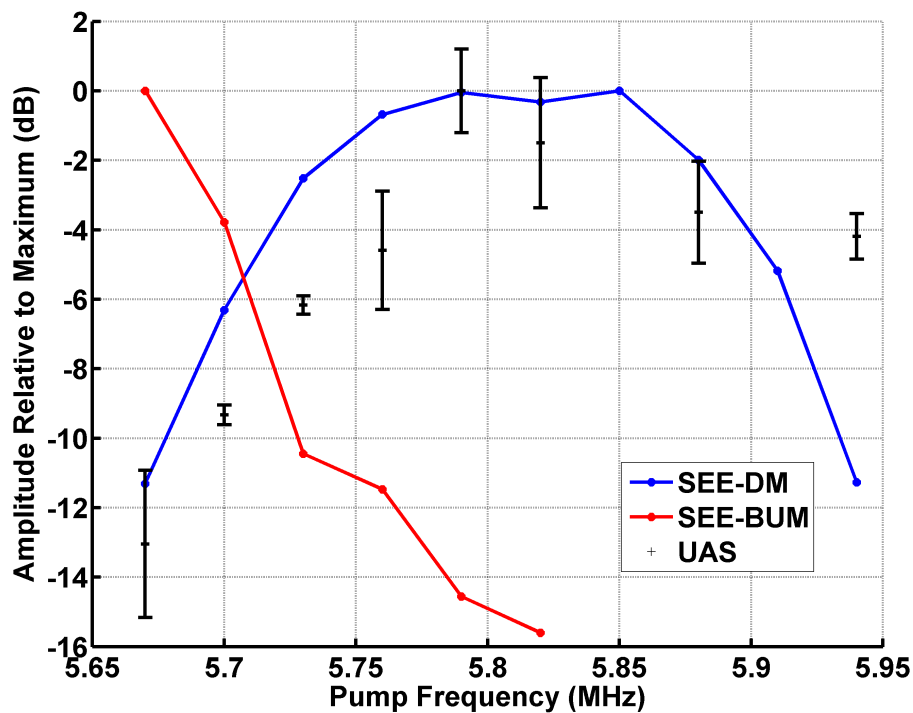


Figure 3.16: Amplitudes of DM (blue trace), BUM (red trace), and received power at UAS (black, with bars) relative to maximum values, as a function of the pump frequency. All data points are time averages over measurements taken at maximum ERP at the listed frequency and are normalized independently so that the maximum of each trace maps to 0 dB. All measurements taken on June 6th. Error bars of the black trace are the standard deviation of the mean of SNR measured at UAS during maximum ERP.

BUM and DM features respectively in the SEE spectrum. The SSS were also directly studied with GPS signals. We observed a nonlinear dependence of the STEC amplitude on the power of the HF heater. At any heating frequency the STEC amplitude first increases with ERP until it reaches a peak and then decays. This effect is due to competition between anomalous absorption, which controls the formation of dekameter striations, and instabilities which form SSS.

The SEE measurements show 90% saturation of the DM and BUM amplitude at $\approx 50\%$ of HAARPs maximum ERP. This is the first time this saturation has been observed, since similar previous experiments at the Sura facility were limited by a maximum ERP of 25% of HAARPs. We also observed the nonlinear dependence of the BUM and DM amplitude on the heating frequency and found that the BUM amplitude decayed by ≈ 10 dB / 100 kHz, while the DM amplitude first increased by 12 dB / 100 kHz, saturated, then decayed at 12 dB / 100 kHz.

We found that HF waves from HAARP were scattered by the AIT into the ionospheric waveguide oriented along Earth's terminator, analogous to a whispering gallery mode that allows the long distance propagation of waves around concave surfaces, guided in this case by the curvature of the channel between the E- and F-region electron density peaks [52, 53], and were subsequently detected at UAS. Simultaneous attempts to measure the scattered HF signal in Ukraine and Scandinavia were unsuccessful, demonstrating the critical role played by the terminator. The intensity of the received signal at UAS also has a frequency dependence, with the maximum occurring at the same frequency as the DM peak in the SEE and the minimum correlating with the BUM peak in the SEE. We also found that the

signal at UAS was Doppler broadened by $\Delta f_D = 1.15 - 1.40$ Hz, which corresponds to a velocity of ionospheric irregularities of 30-35 m/s, which is consistent with our direct measurements from the Kodiak radar.

The combination of the strong frequency dependence of the received signal at UAS, the presence of ionospheric dekameter scale striations shown indirectly by SEE and directly by Kodiak, all of which are consistent with scattering off of striations, leads us to conclude that the signal detected at UAS was generated by direct scattering of the HF signal into the ionospheric waveguide by the dekameter scale artificial striations pumped by AIT, and not by mirror reflection of the sidelobe radiation.

Chapter 4: Vlasov Simulations Near the Upper Hybrid Layer

4.1 Introduction

Magnetic field-aligned striations (FAS) are plasma density depletions which are frequently produced by electrostatic processes during high-frequency (HF) ordinary (O) mode heating of the ionosphere. Small-scale FAS have transverse sizes of a few meters [54, 55], while their sizes along the magnetic field are several tens of kilometers [13, 14]. Striations typically form on time-scales of the order of seconds after the heating beam is switched on, and similarly, they dissipate on the order of seconds after the heating is switched off. Once formed, an incident electromagnetic wave is mode-converted to upper hybrid waves trapped in the striation, heating the electrons, and further increasing the density depletion. The mode conversion leads to anomalous absorption of the O-mode wave near the altitude of the ionospheric upper hybrid resonance [30].

Following the upgrade of the High Frequency Active Auroral Research Program (HAARP) heater to Effective Radiated Powers (ERPs) up to 5 GW, Pedersen et al. [56] observed descending artificial ionospheric layers (DAILs). The DAILs are believed to be formed due to the ionization of the neutral gas by suprathermal electrons accelerated by the induced ionospheric turbulence [57]. Once the layer reaches

sufficient density to reflect the pump wave, the interaction region shifts downwards, creating the DAILs. Eliasson et al. [36] employed a multi-scale numerical model of the generation and descent of DAILs and found that the bulk electron temperature needs to exceed 4000K for a significant fraction of the electrons in the tail of the distribution function to be efficiently accelerated by the turbulence. A possible scenario is that the bulk electrons are first heated at the upper hybrid layer, and as the hot electrons reach the critical layer, they are further accelerated by strong Langmuir turbulence to form high energy tails.

The commonly discussed mechanism of electron heating near the upper hybrid layer involves collisional Ohmic heating by mode converted upper hybrid waves trapped in FAS [13, 14]. In the weakly collisional plasma of the F-region ionosphere, the Ohmic heating of electrons takes place on time-scales of the order of seconds. However, a potentially faster and more efficient mechanism is stochastic heating, which takes place in the presence of large amplitude electric field gradients [58, 59, 60, 61, 62]. As the amplitude exceeds a threshold for stochasticity, the particle orbits become unstable and diverge in time, leading to a very rapid heating of the plasma. Stochastic heating is favored by small-scale turbulence involving large amplitude, short wavelength electrostatic waves.

The aim of this chapter is to investigate stochastic electron heating near the upper hybrid layer, by means of Vlasov simulations relevant to ionospheric heating experiments. The chapter is organized as follows: In section 4.2, we describe the simulation model and numerical parameters. We present simulation results between the second and third gyroharmonic, including analysis of ion density fluctuations,

electron heating, and analysis of wave modes, parametric decay processes, and potential heating mechanism in section 4.4. In section 4.5 we present simulation results directly applicable to ionospheric heating experiments, and employ our test particle simulations to isolate effects of specific wave modes on electron heating. Finally, we present summary and conclusions of this work in section 4.6.

4.2 Simulation Set-up

To study the collisionless heating of electrons in small-scale FAS, we have carried out electrostatic Vlasov simulations in one spatial and two velocity dimensions. To eliminate the effects of numerical noise in the simulations, we solve the Vlasov equation in position and velocity space using a Fourier method in velocity space [63]. The simulation domain is along the x -axis while the velocity is in the (v_x, v_y) space. The Vlasov equation describes the evolution of the distribution function f_α of charged particles of species α (where α equals i and e for ions and electrons, respectively) in position and velocity space,

$$\frac{\partial f_\alpha}{\partial t} + v_x \frac{\partial f_\alpha}{\partial x} + \frac{\vec{F}_\alpha}{m_\alpha} \cdot \nabla_v f_\alpha = 0, \quad (4.1)$$

where

$$\vec{F}_\alpha = q_\alpha \left(\vec{E} + \vec{E}_{ext} + \vec{v} \times \vec{B}_0 \right) \quad (4.2)$$

is the Lorentz force, q_α and m_α are the particle's charge and mass, $q_e = -e$ and $q_i = e$, and e is the magnitude of the electron charge. The constant magnetic field $\vec{B}_0 = \hat{z}B_0$ is directed along the z -axis. The O-mode pump wave is represented by an external oscillating dipole electric field $\vec{E}_{ext} = \hat{x}E_0 \sin(\omega_0 t)$ directed along the x -axis

at frequency ω_0 and with amplitude E_0 . The most common ion species at the F_2 layer is atomic oxygen, but for numerical efficiency, we use the proton-to-electron mass ratio $m_i/m_e = 1836$, which gives a sufficient separation between high-frequency and low-frequency wave dynamics.

We use the electrostatic approximation $\vec{E} = -\hat{x}\partial\phi/\partial x$ for the electric field, where the electrostatic potential is obtained from the Poisson equation

$$-\frac{\partial^2\phi}{\partial x^2} = \frac{\rho}{\epsilon_0}. \quad (4.3)$$

Here, the electron charge density is

$$\rho = \sum_{\alpha=i,e} q_\alpha n_\alpha, \quad (4.4)$$

and the particle number density

$$n_\alpha(\vec{x}, t) = \int \int f_\alpha(\vec{x}, \vec{v}, t) dv_x dv_y. \quad (4.5)$$

The size of the one-dimensional spatial simulation domain is 9 m resolved by 600 points, giving a grid spacing of 1.5 cm, and the simulation time is about 300 μ s over a total of 84000 time steps that are dynamically chosen during the simulation to maintain numerical stability, resulting in an average time-step of about 4 ns. The initial electron and ion temperatures are set to $T_{e0} = 1500$ K and $T_{i0} = 1000$ K, consistent with measurements of ionospheric temperatures before heating using incoherent scatter radars [64, 65], using Maxwellian electron and ion velocity distributions. In velocity space, we chose a two-dimensional grid of 160x160 points for both the electrons and ions. For the electrons, the velocity space covers the range $\pm 25v_{Te0}$ in the v_x and v_y directions, while for the ions it covers the range $\pm 17.6v_{Ti0}$

where $v_{Te0} = \sqrt{k_B T_{e0}/m_e} = 1.508 \times 10^5$ m/s is the electron thermal speed and $v_{Ti0} = \sqrt{k_B T_{i0}/m_i} = 2.873 \times 10^3$ m/s is the ion thermal speed.

As initial conditions for the electron and ion number densities, a Gaussian density striation superimposed on a background plasma density,

$$n_i(x) = n_e(x) = n_0 [1 - \alpha \exp(-x^2/R^2)], \quad (4.6)$$

with a relative density depletion of $\alpha = 0.1$ and transverse size of $R = 1.5$ m. A schematic of the simulation set-up is shown in Figure 4.1. The external magnetic field $B_0 = 5.17 \times 10^{-5}$ T corresponds to the background field at a mid-latitude HF heating facility like HAARP and has associated cyclotron frequencies of $\omega_{ce} = eB_0/m_e = 9.09 \times 10^6$ s⁻¹ (1.447 MHz), and $\omega_{ci} = eB_0/m_i = 4.952 \times 10^3$ s⁻¹ (0.788 kHz). The combination of the ambient electron density $n_e = n_0$ and the pump wave frequency ω_0 are chosen such that the pump frequency matches the local upper hybrid frequency $\omega_{UH}(x) = \sqrt{\omega_{pe}^2(x) + \omega_{ce}^2}$ at the edges of the striation where $n_e = 0.95n_0$, where $\omega_{pe}(x) = \sqrt{n_e(x)e^2/(\epsilon_0 m_e)}$ is the local electron plasma frequency. We consider two cases, the first is *off-resonance* where the pump frequency is between the second and third gyroharmonics, and *on-resonance* where we consider the pump frequency close to the fourth gyroharmonic, consistent with HAARP experiments described in previous chapters. A summary of the physical parameters is shown in Table 4.1.

For heating off resonance, the background plasma density is $n_0 = 1.27 \times 10^{11}$ m⁻³ with corresponding plasma frequencies of the electrons $\omega_{pe} = 20.09 \times 10^6$ s⁻¹ (3.197 MHz), and ions $\omega_{pi} = 4.691 \times 10^5$ s⁻¹ (74.66 kHz). The pump frequency

is $\omega_0 = 21.59 \times 10^6 \text{ s}^{-1}$ (3.436 MHz), the pump amplitude is $E_0 = 2.0 \text{ V/m}$, and $\omega_0/\omega_{ce} = 2.37$. The lower hybrid frequency is $\omega_{LH} = 1.95 \times 10^5 \text{ s}^{-1}$ (31.04 kHz)

For heating on resonance, we consider two sub-cases, the first with ω_0 below the fourth gyroharmonic, and the second with ω_0 very close to the fourth gyroharmonic, $\omega_0/\omega_{ce} = 3.80$ and 4.01 . The ambient density n_0 is $3.67 \times 10^{11} \text{ m}^{-3}$ and $4.12 \times 10^{11} \text{ m}^{-3}$ with corresponding plasma frequencies of the electrons $\omega_{pe} = 34.20 \times 10^6$ and $36.23 \times 10^6 \text{ s}^{-1}$ (5.443 and 5.766 MHz) and of the ions $\omega_{pi} = 7.982 \times 10^5$ and $8.455 \times 10^5 \text{ s}^{-1}$ (127.03 and 134.57 kHz) chosen to maintain $\omega_0 = \omega_{UH}$ at $0.95n_0$ as ω_0 is moved through the gyroharmonic, simulating increasing interaction altitude of higher frequency waves. The pump frequency is $\omega_0 = 34.55 \times 10^6$ and $36.46 \times 10^6 \text{ s}^{-1}$ (5.499 and 5.803 MHz). The pump amplitude is $E_0 = 2.0 \text{ V/m}$, and the lower hybrid frequencies are $\omega_{LH} = 2.051 \times 10^5$ and $2.058 \times 10^5 \text{ s}^{-1}$ (32.64 and 32.76 kHz).

For test particle simulations, we use the explicit Beeman predictor-corrector algorithm [66]

$$x_{i+1} = x_i + \Delta t (v_i) + \Delta t^2 \left(\frac{2}{3}a_i - \frac{1}{6}a_{i-1} \right) + O(\Delta t^4) \quad (4.7)$$

$$v_{i+1,p} = v_i + \Delta t \left(\frac{3}{2}a_i - \frac{1}{2}a_{i-1} \right) + O(\Delta t^3) \quad (4.8)$$

$$v_{i+1,c} = v_i + \Delta t \left(\frac{5}{12}a_{i+1} + \frac{8}{12}a_i - \frac{1}{12}a_{i-1} \right) + O(\Delta t^3) \quad (4.9)$$

the time step is identical to the Vlasov simulations, and accelerations are computed from the Lorentz force given in equation 4.2 with the magnetic field B_0 and the electric fields interpolated from the self-consistent Vlasov simulation. At each time step, the particle positions at the next time step are computed, the velocities are predicted, the velocity dependent acceleration is computed, and the velocity is cor-

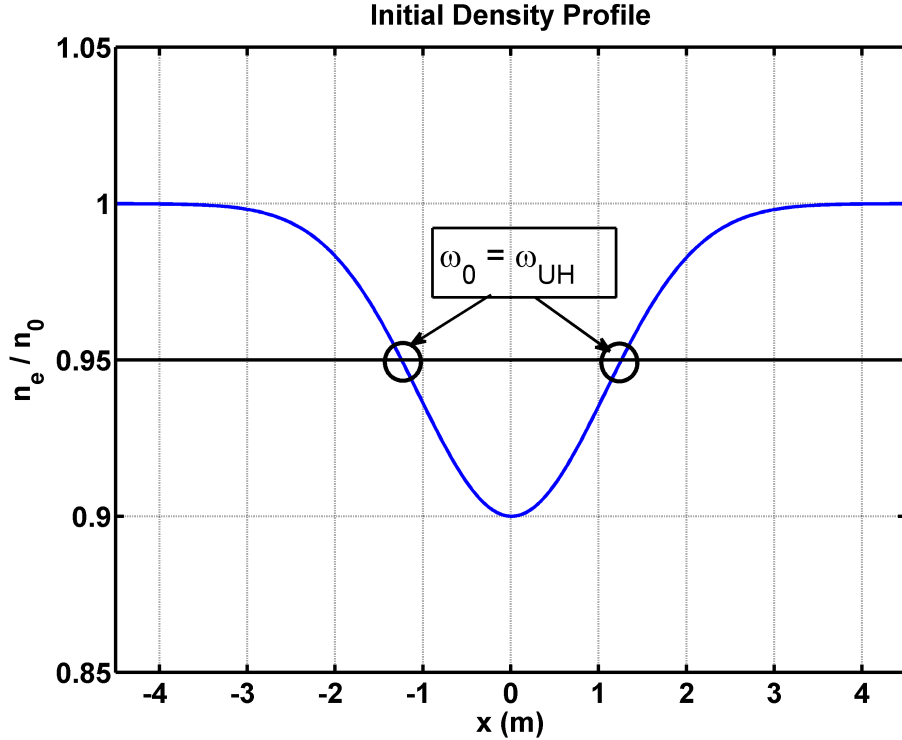


Figure 4.1: Simulation overview: The profile of the initial density striation with the density at $\omega_0 = \omega_{UH}$ indicated.

rected using the computed accelerations. The Beeman algorithm combines a fast solver with energy drift over our simulation of $\approx 7\%$. Convergence was tested over $10^3 - 10^6$ particles with test particles assigned initial velocities from the 2D Maxwell distribution corresponding to T_{e0} and initial positions drawn from the distribution given in equation 4.6.

4.3 Results

Here we present the results of simulations for both off-resonance and on-resonance heating. For off-resonant heating with $\omega_0/\omega_{ce} = 2.37$, we present only

ω_0/ω_{ce}	2.37	3.80	4.01
n_0 (m^{-3})	1.27×10^{11}	3.67×10^{11}	4.12×10^{11}
ω_{pe} (s^{-1}) (MHz)	20.09×10^6 (3.20)	34.20×10^6 (5.44)	36.23×10^6 (5.77)
ω_{pi} (s^{-1}) (kHz)	4.691×10^5 (74.7)	7.982×10^5 (127)	8.455×10^5 (134)
ω_0 (s^{-1}) (MHz)	21.59×10^6 (3.44)	34.55×10^6 (5.50)	36.46×10^6 (5.80)
E_0 (V/m)	2.0		
B_0 (T)	5.17×10^{-5}		
w_{ce} (s^{-1}) (MHz)	9.09×10^6 (1.45)		
w_{ci} (s^{-1}) (kHz)	4.952×10^3 (0.79)		
ω_{LH} (s^{-1}) (kHz)	1.95×10^5 (31.0)	2.051×10^5 (32.6)	2.058×10^5 (32.8)
T_{e0} (K)	1500		
T_{i0} (K)	1000		
v_{Te} (m/s)	1.508×10^5		
v_{Ti} (m/s)	2.873×10^3		

Table 4.1: Summary of physical parameters used in the Vlasov simulations, for off-resonant (first column) and on-resonant (second and third columns) heating, and some derived plasma parameters.

Vlasov simulation results, while for the on-resonant heating with $\omega_0/\omega_{ce} = 3.80$ and 4.01, we include both Vlasov and test-particle simulations.

4.4 Off-Resonance Heating

4.4.1 Ion Density

A plot of the time evolution of the ion density in space and Fourier space is shown in figure 4.2.

The seeded density striation shown in figure 4.1 is visible in figure 4.2(a) for $-1.5 \leq x \leq 1.5$ m. Large amplitude ion density fluctuations appear after about 0.05 ms, in the form of a standing wave pattern oscillating in time with a frequency close to the lower hybrid frequency. The wavenumber spectrum of the ion density in figure 4.2(b) shows notable features: a consistent component near $k = 10 - 20$ m^{-1} and another peak near $k = 40 - 60$ m^{-1} , corresponding to wavelengths of $\lambda = 0.30 - 0.60$ m and $\lambda = 0.10 - 0.15$ m respectively. Wave components below $k = 3$ m^{-1} have been trimmed as they correspond to the time-stationary density striation seen in figure 4.2(a).

4.4.2 Electron Heating

The evolution of the electron temperature in space and time is shown in figure 4.3.

The electron heating is significant, with a rise of the electron temperature by several thousands of Kelvin, which is correlated with the onset of lower hybrid

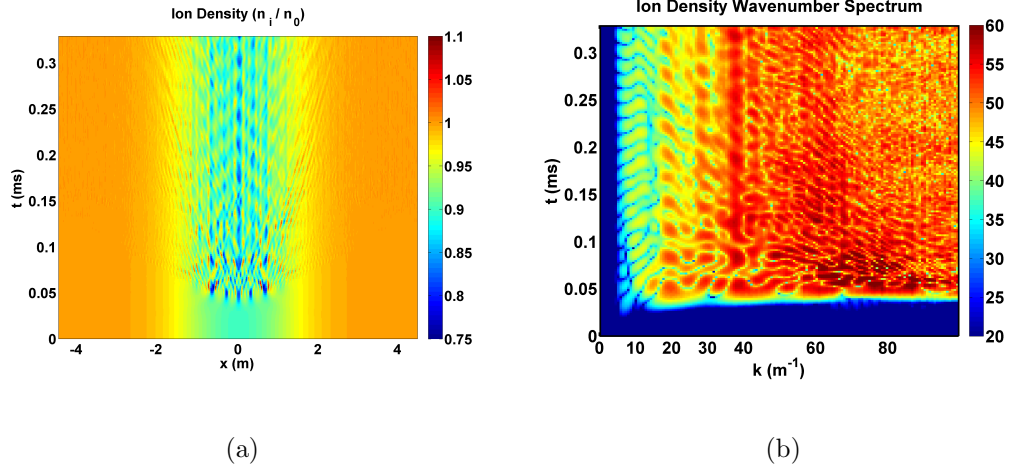


Figure 4.2: Time evolution of the normalized ion density n_i/n_0 in (a) space and (b) wavenumber space.

oscillations seen in figure 4.2. From figure 4.3 and the snapshots of the spatial temperature profiles in figure 4.4(a) we see that the most efficient heating occurs near the center of the striation, while the electron temperature outside the central cavity rises more slowly. The time evolution of the electron temperature, spatially averaged over the center of the striation is shown in figure 4.4(b). After the initial 0.05 ms turn-on time, the electrons are heated rapidly to $T_e \approx 4000$ K over the next 0.05 ms, after which they heat more slowly up to $T_e \approx 6000$ K over the remaining 0.20 ms to the end of the simulation.

The heating gives rise to an electron distribution function which is gyrotropic in (v_x, v_y) space. A cut of the electron distribution along v_x is shown in figure 4.5. The initially Maxwellian velocity distribution widens and develops into a more flat-topped distribution as the bulk electrons are accelerated by the turbulence.

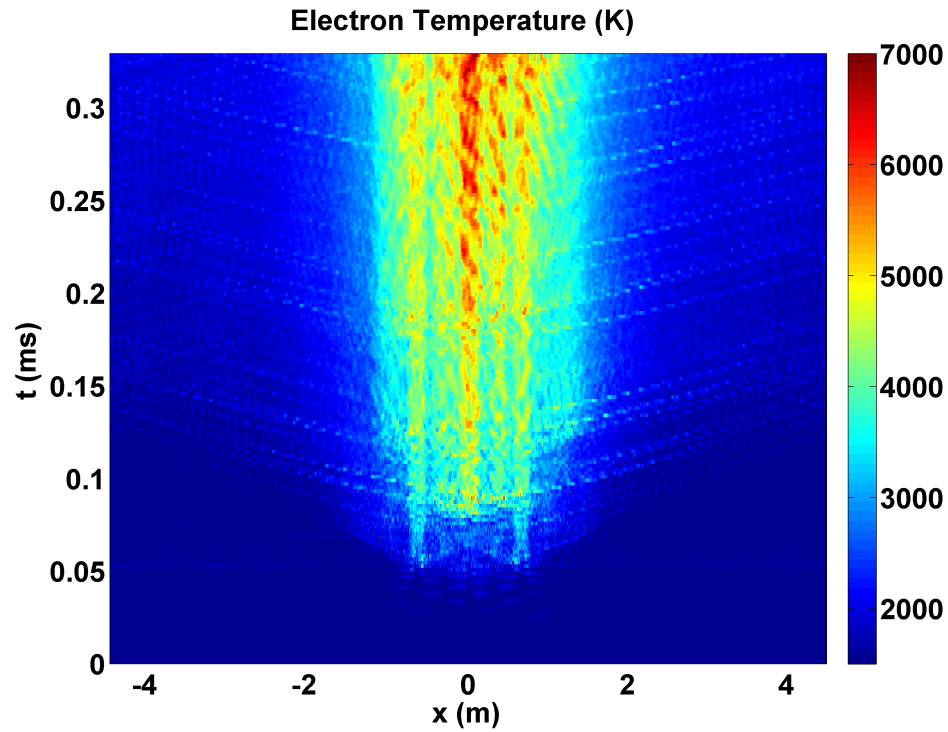


Figure 4.3: Evolution of the electron temperature T_e (K) in time and space.

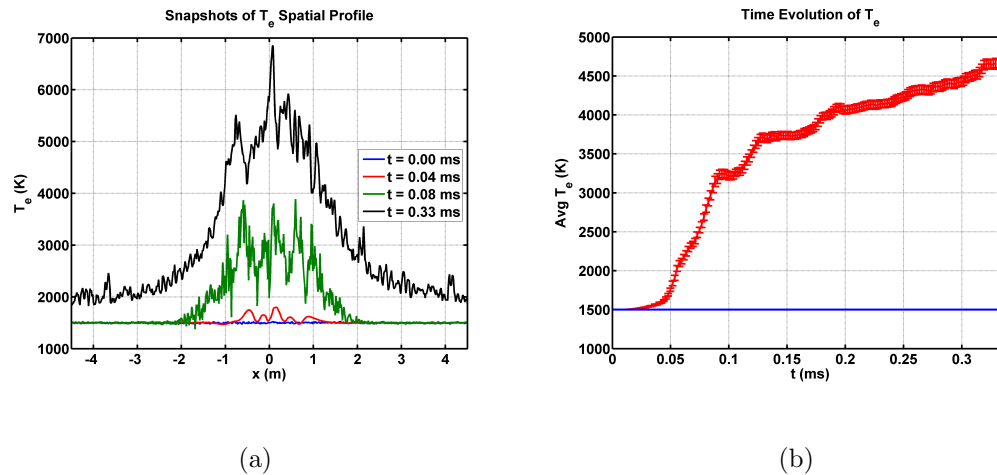


Figure 4.4: (a) Spatial profiles of T_e at different times, and (b) the time evolution of T_e averaged over space $-1.5 \text{ m} \leq x \leq 1.5 \text{ m}$ at the center of the striation.

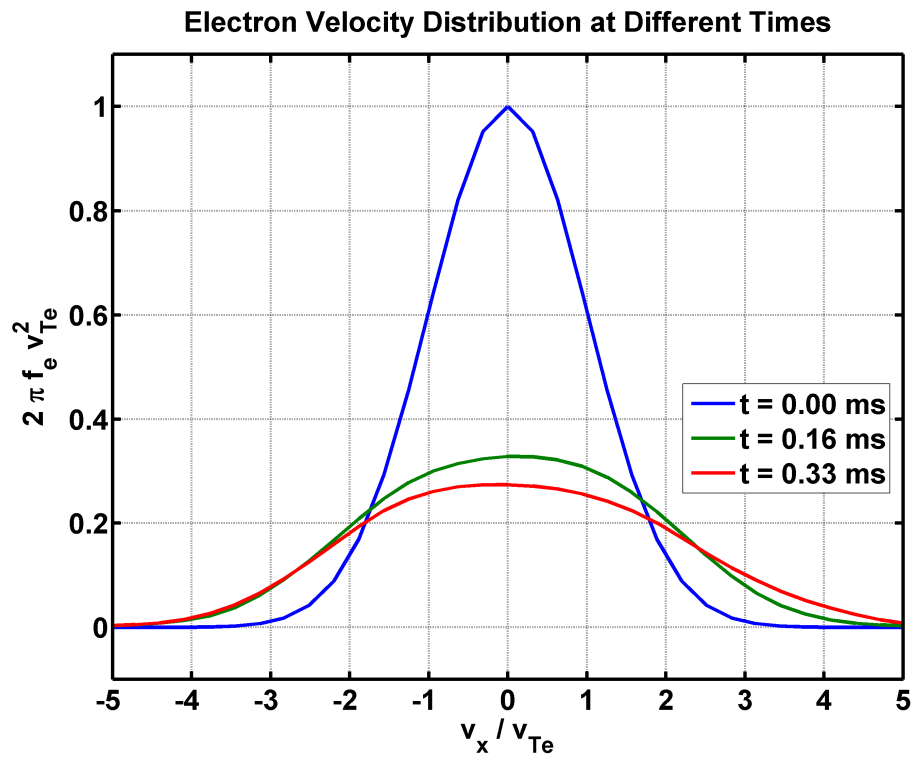


Figure 4.5: Profiles of the electron velocity distribution at different times. Initially, the velocity profile is Maxwellian, but as the electrons are heated, the distribution widens and becomes more flat-topped.

4.4.3 Observed High-Frequency and Low-Frequency Wave Modes

Inside of the striation, both high-frequency and low-frequency waves are excited by the external pump wave. To diagnose these, we investigate the temporal and spatial wave spectra of the simulation electric field data. We concentrate here on the frequencies covering the lower hybrid components $f < 100$ kHz and frequencies covering the upper hybrid components $3.3 < f < 3.6$ MHz. In the low-frequency spectrum in figure 4.6(a) there is a peak between 30 and 35 kHz, near the lower hybrid frequency $f_{LH} \approx 31$ kHz (see table 4.1). In the high-frequency frequency spectrum in figure 4.6(b), the pump wave is visible at $f_0 = 3.436$ MHz, and two downshifted peaks are visible at $f = 3.41$ and 3.38 MHz. The difference in frequency between adjacent peaks in the high-frequency spectrum corresponds to the lower hybrid frequency.

After separating the frequency spectrum, the high and low frequency components is inverse Fourier transformed back into space and time. The amplitude of the high and low frequency components are shown in figure 4.7. While both the high and low frequency waves appear to be mostly confined to the initially seeded density striation, there is noticeable leaking of high-frequency waves propagating away from the striation which we later identify as short wavelength electron Bernstein waves. Low-frequency electric fields are visible after about 0.05 ms, similar to the ion density fluctuations in figure 4.1

Plots of the wavenumber spectra of the low- and high-frequency components of the electric field are shown in figure 4.8. For the most part, the components occupy

distinct scales. The high-frequency components in figure 4.8(b) show a condensation at small wavenumber $k < 7\text{m}^{-1}$, while the low-frequency components in figure 4.8(a) peak at $k \approx 7\text{m}^{-1}$. This is typical for an inverse cascade of upper hybrid waves to smaller wavenumbers, downshifted in frequency, accompanied by lower hybrid waves at larger wavenumbers. There are also spectral components at large wavenumbers $k \approx 50 - 70\text{m}^{-1}$ in the low-frequency spectrum and $k \approx 40 - 60\text{m}^{-1}$ in the high-frequency spectrum, which we associate with short wavelength electron Bernstein waves interacting with lower hybrid waves.

The power spectrum of the electric field in wavenumber and frequency space is shown in figure 4.9 and is compared with numerical solutions of the dispersion relations for electron Bernstein and lower hybrid waves in figure 4.10. The pump wave is seen just below $f = 3.5$ MHz at $k = 0$. The immediately neighboring non-zero wavenumbers are upper hybrid waves, and the spectral components extending out to higher wavenumbers are associated with the second electron Bernstein mode. Similarly, the arched features near $k = 50 \text{ m}^{-1}$ and $f = 2.0$ MHz are associated with the first electron Bernstein mode. The electron Bernstein mode associated with the upper hybrid frequency has a resonance at the second cyclotron resonance, $f = 2f_{ce} = 2.9$ MHz, while the first electron Bernstein mode is associated with the first cyclotron resonance $f = f_{ce} = 1.45$ MHz at large wavenumbers. Components of the third Bernstein mode are visible for frequencies near $f = 4.5$ MHz. Lower hybrid waves are visible for $|k| < 100 \text{ m}^{-1}$ and $f < 100$ kHz. The excitations of Bernstein modes at large wavenumbers cover wide bands in $\omega - k$ space, which indicates that the plasma parameters change in time. The increase in the electron

temperature from $T_{e0} = 1500$ to 6000 K in the striation (see figures 4.3 and 4.4) affects the dispersion properties of the electron Bernstein modes.

The dispersion relation for electron Bernstein waves is given by [67]

$$1 + \frac{\omega_{pe}^2 \exp(-\lambda)}{\omega_{ce}^2 \sin(\pi\Omega)} \int_0^\pi \sin(\psi\Omega) \sin(\psi) \exp[-\lambda \cos(\psi)] d\psi = 0, \quad (4.10)$$

where $\lambda = k^2 v_{Te}^2 / \omega_{ce}^2$ and $\Omega = \omega / \omega_{ce}$. The low-frequency mode associated with lower hybrid waves is derived from the dispersion relation

$$1 + \chi_e + \chi_i = 0 \quad (4.11)$$

where the ion and electron susceptibilities are respectively given by

$$\chi_i = -\frac{\omega_{pi}^2}{\omega^2 - \omega_{ci}^2 - \gamma_i v_{Ti}^2 k^2} \quad (4.12)$$

and

$$\chi_e = -\frac{\omega_{pe}^2}{\omega^2 - \omega_{ce}^2 - \gamma_e v_{Te}^2 k^2}. \quad (4.13)$$

In the frequency range $\omega_{ci}^2 \ll \omega^2 \ll \omega_{ce}^2$, we obtain the low-frequency dispersion relation

$$\omega^2 = \gamma_i v_{Ti}^2 k^2 + \frac{\omega_{pi}^2 (\omega_{ce}^2 + \gamma_e v_{Te}^2 k^2)}{\omega_{pe}^2 + \omega_{ce}^2 + \gamma_e v_{Te}^2 k^2}, \quad (4.14)$$

where the adiabatic factors are $\gamma_i = 3$ and $\gamma_e = 1$. The electron and ion thermal effects lead to an increase of the frequency with wavenumber.

The three first electron Bernstein branches and the lower hybrid branch are plotted in figure 4.10 for different electron temperatures. We note from figure 4.10 that the electron Bernstein dispersion curves contract in wavenumber space for higher electron temperatures. Since the electron temperature is time-dependent in

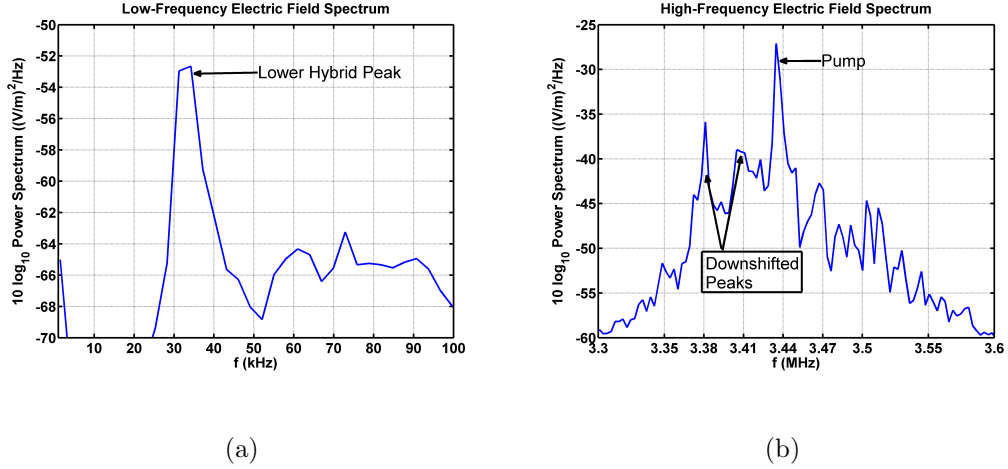


Figure 4.6: Frequency spectra of the electric field showing (a) the low frequency and (b) high frequency components.

the simulations, and the Fourier transform in space and time effectively averages over time and space, figure 4.9 shows signatures of electron Bernstein modes at different temperatures mapped into the same plot. By applying a Gaussian window in time and space before performing the Fourier transforms, and by shifting the center of the window in time, we obtain an approximate time dependence of the wave spectrum. A few snapshots are shown in figure 4.11 with time and space centers and standard deviations, σ_x and σ_t , given for each snapshot. At $t = 0.02$ ms, we see only the pump wave and a narrow spectrum of neighboring upper hybrid waves, and a similar band of low frequency lower hybrid waves. At $t = 0.04$ ms, electron Bernstein modes near the upper hybrid frequency are excited, but the principle components are the upper hybrid and lower hybrid waves. At $t = 0.08$ ms, the Bernstein modes have significantly increased in amplitude, and by $t = 0.30$ ms, they have clearly contracted in wavenumber space due to the increase of electron temperature.

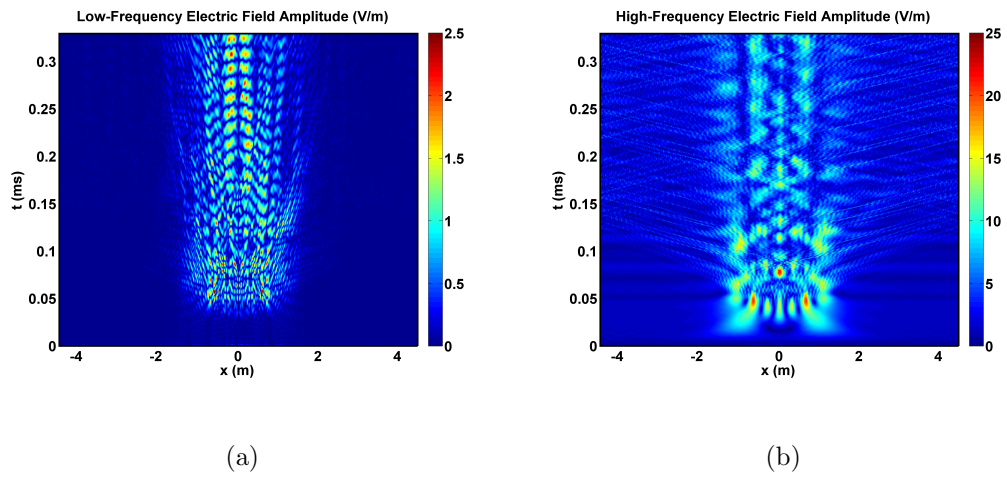


Figure 4.7: The amplitudes of (a) the low-frequency electric field, and (b) the high-frequency electric field.

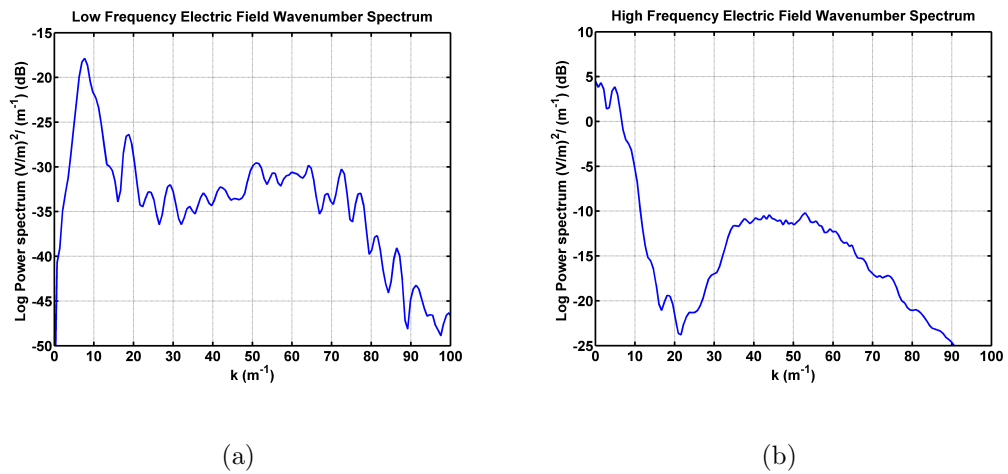


Figure 4.8: Electric field E_x wavenumber spectrum separated into (a) low-frequency and (b) high-frequency components.

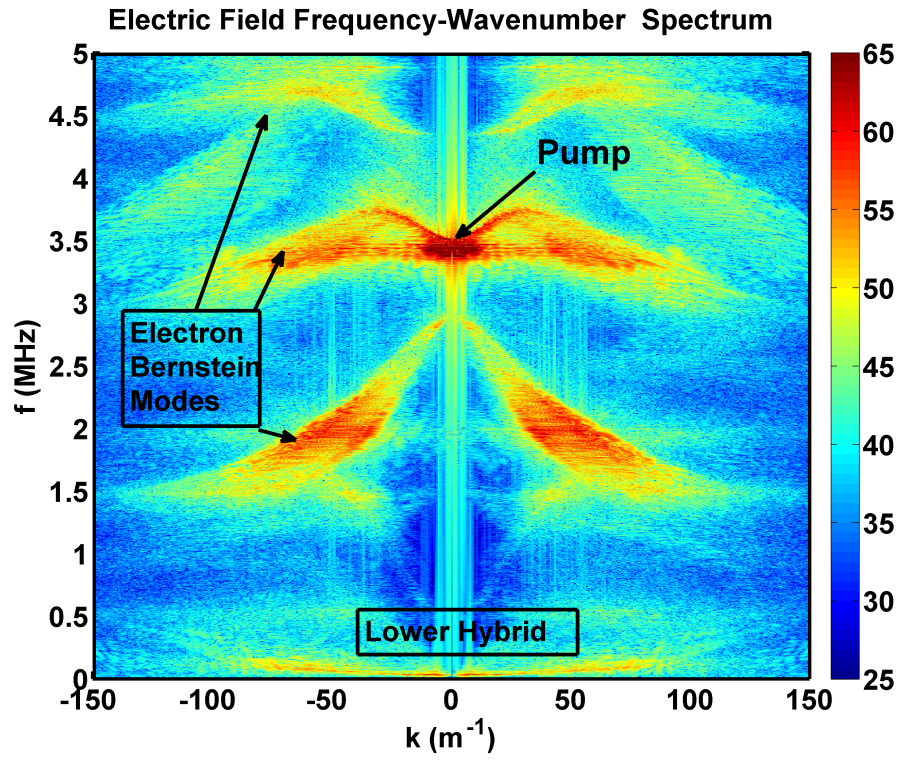
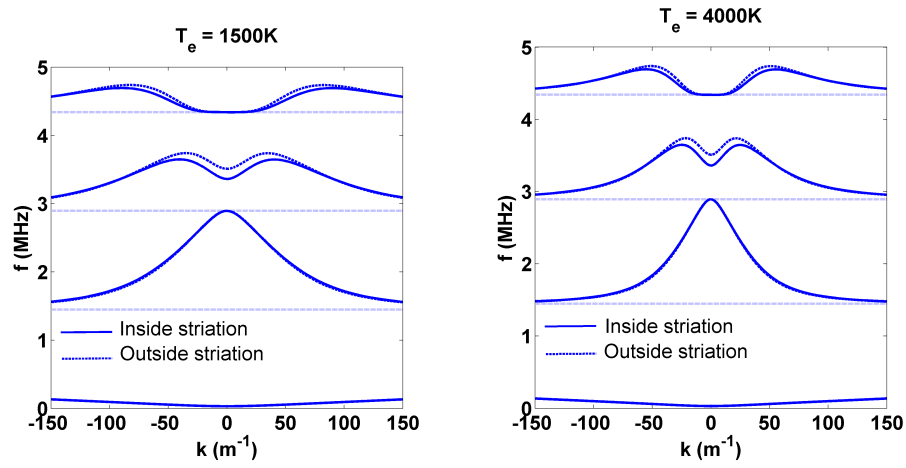
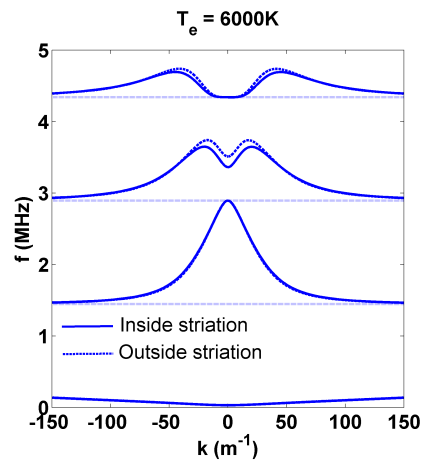


Figure 4.9: Frequency-wavenumber power spectrum of E_x ($10 \log_{10}$ scale). The pump wave is seen near $k = 0$ at $f = 3.44$ MHz. Electron Bernstein modes are visible near $k = \pm 50 \text{ m}^{-1}$ and $f = 2.0$ MHz. Lower hybrid waves are seen for $|k| < 100 \text{ m}^{-1}$ and $f < 100 \text{ kHz}$.



(a)

(b)



(c)

Figure 4.10: Electron Bernstein and lower hybrid dispersion curves for (a) 1500 K, (b) 4000 K, and (c) 6000K. In each figure, the first three branches of the electron Bernstein modes are shown, with resonances at the respective electron cyclotron harmonic at large wavenumbers.

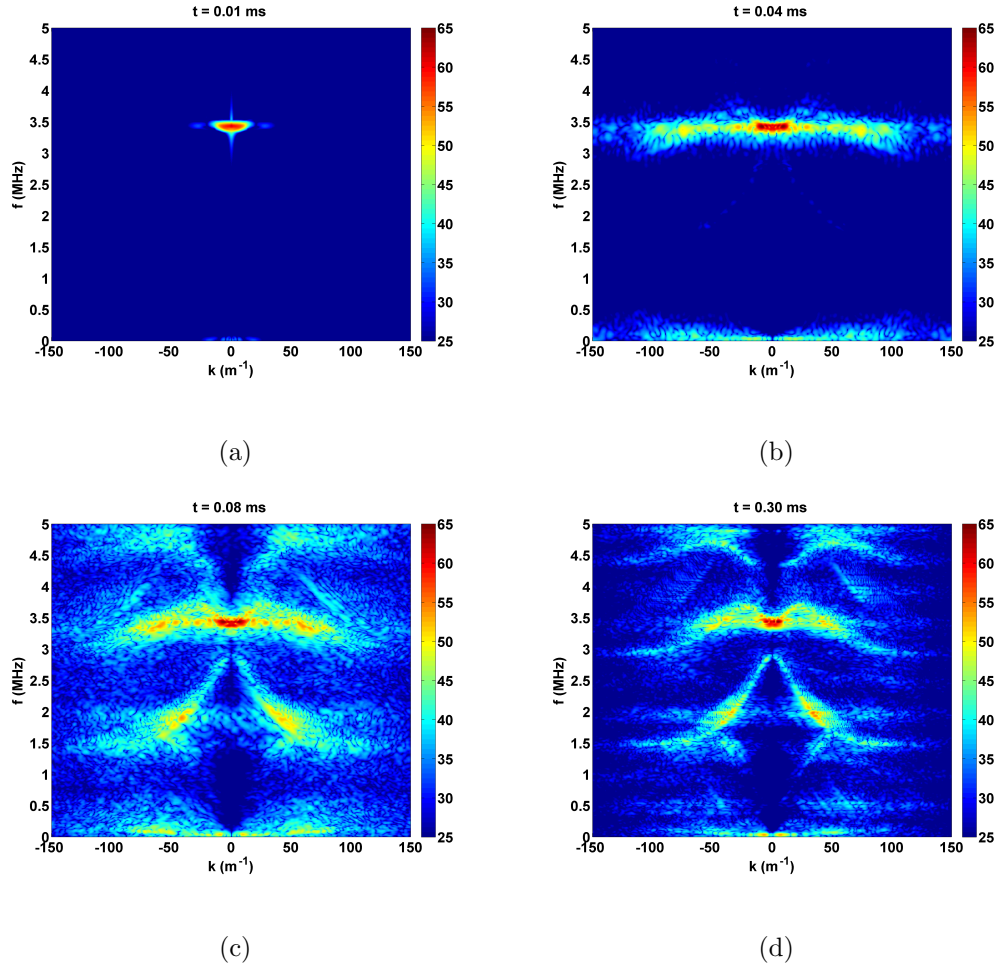


Figure 4.11: E_x Frequency-wavenumber plots with Gaussian windows to isolate the bottom of the seed density striation ($x = 0$) in space ($\sigma_x = 1$ m), and to cover principally ± 0.01 ms ($\sigma_t = 0.01$ ms) from their focus time. Shown are spectra at: (a) $t = 0.02$ ms, (b) $t = 0.04$ ms, (c) $t = 0.05$ ms, (d) $t = 0.30$ ms.

4.4.4 Parametric Decay of Upper Hybrid to Upper Hybrid and Lower Hybrid Waves

Linear mode conversion of the pump wave (E_0, ω_0) to upper hybrid waves takes place at the edge of the density cavity where the plasma density is 95% of the ambient density, so that $\omega_0 = 21.59 \times 10^6 \text{ s}^{-1}$ (see Table 4.1). The mode converted upper hybrid wave can propagate to the center of the striation and interact nonlinearly with lower hybrid waves in the form of a three-wave decay creating a daughter upper hybrid wave and a lower hybrid wave. Correcting for kinetic effects of finite ω_{ce}/ω_{pe} ratio, the dispersion relation for upper hybrid waves is [68]

$$\omega^2 = \omega_{UH}^2 + \frac{3v_{Te}^2 k^2 \omega_{pe}^2}{\omega^2 - 4\omega_{ce}^2}, \quad (4.15)$$

which can be derived from Eq. 4.10 for $v_{Te}k/\omega_{ce} \ll 1$. The bottom of the density cavity is homogenous to first order, so we can assume a constant density at 90% of the ambient density. For a given frequency $\omega = \omega_0$, the wavenumber $k = k_0$ can be obtained from

$$\omega_0^2 = 0.9\omega_{pe}^2 + \omega_{ce}^2 + \frac{3v_{Te}^2 k_0^2 0.9\omega_{pe}^2}{\omega_0^2 - 4\omega_{ce}^2}.$$

We consider three separate temperatures, the initial $T_{e0} = 1500 \text{ K}$, and two temperatures $T_e = 4000 \text{ K}$ and $T_e = 6000 \text{ K}$ observed later in the simulation. For each of these temperatures and using the parameter values in Table 4.1, the upper hybrid wavenumber k_0 and associated wavelength $\lambda_0 = 2\pi/k_0$ are given in table 4.2.

The lower hybrid frequency at the bottom of the striation at small wavenum-

bers is

$$\omega_{LH} \approx \frac{1}{\sqrt{(\omega_{ci}\omega_{ce})^{-1} + \omega_{pi}^{-2}/0.9}}, \quad (4.16)$$

giving $\omega_{LH} = 1.92 \times 10^5 \text{ s}^{-1}$ (30.48 kHz). The frequency difference between the driving frequency and the local upper hybrid frequency at the bottom of the cavity is

$$\begin{aligned} \Delta\omega &= \sqrt{0.95\omega_{pe}^2 + \omega_{ce}^2} - \sqrt{0.90\omega_{pe}^2 + \omega_{ce}^2}, \\ &= 4.73 \times 10^5 \text{ s}^{-1} = 75.26 \text{ kHz}. \end{aligned} \quad (4.17)$$

Hence, since $\Delta\omega/\omega_{LH} = 2.47$ there is sufficient room in frequency space for a double decay of upper hybrid waves to down-shifted daughter upper hybrid waves, with successive downshifts equal to the lower hybrid frequency.

The three-wave decay obeys the matching conditions

$$\omega_0 = \omega_1 + \omega_{LH}, \quad (4.18)$$

$$k_0 = k_1 + k_{LH}. \quad (4.19)$$

for the frequencies and wave vectors, when an upper hybrid wave, (ω_0, k_0) , decays into a daughter upper hybrid wave, (ω_1, k_1) and a lower hybrid wave, (ω_{LH}, k_{LH}) .

Using Eq. 4.18 to eliminate ω_1 in the upper hybrid dispersion relation for (ω_1, k_1)

$$(\omega_0 - \omega_{LH})^2 = 0.9\omega_{pe}^2 + \omega_{ce}^2 + \frac{3v_{Te}^2 k_1^2 0.9\omega_{pe}^2}{(\omega_0 - \omega_{LH})^2 - 4\omega_{ce}^2}, \quad (4.20)$$

from which the resulting wavenumbers k_1 and wavelengths $\lambda_1 = 2\pi/k_1$ are obtained and summarized in table 4.3.

The corresponding lower hybrid wavenumber is obtained from Eq. 4.19 as $k_{LH} = k_0 - k_1$. In the second decay, the new frequency matching condition will be

$$\omega_1 = \omega_2 + \omega_{LH},$$

which combined with Eq 4.18 gives

$$\omega_0 = \omega_2 + 2\omega_{LH}, \quad (4.21)$$

and the corresponding dispersion relation for (ω_2, k_2) becomes

$$(\omega_0 - 2\omega_{LH})^2 = 0.9\omega_{pe}^2 + \omega_{ce}^2 + \frac{3v_{Te}^2 k_2^2 0.9\omega_{pe}^2}{(\omega_0 - 2\omega_{LH})^2 - 4\omega_{ce}^2}, \quad (4.22)$$

together with $k_{LH} = k_1 - k_2$. These results are summarized in table 4.4.

Thus, through a three-wave parametric decay process in two steps, the upper hybrid waves cascades to daughter upper hybrid waves at smaller wavenumber and downshifted by the lower hybrid frequency in each step. This corresponds to the two downshifted peaks seen near 3.41 MHz and 3.38 MHz in figure 4.6. Similar results linking downshifted frequency peaks to the decay of trapped upper hybrid waves were found using fluid simulations by Mjølhus [69].

In addition to the three-wave decay scenarios discussed here, it should be noted that the modulational instability (a four-wave process) and strong turbulence [70] may contribute to the localization of wave energy. Some features of localized electron heating in figure 4.3 and localized high-frequency electric fields in figure 4.7(b) during the onset of turbulence indicate that upper hybrid wave collapse takes place. In figure 4.3 there are stationary pockets of heated electrons inside the striation that have the largest increase in temperatures, and in figure 4.7(b) there are pockets

of large amplitude electric field inside the striation that collapse in advance of the onset of fast electron heating.

4.4.5 Parametric Decay of Upper Hybrid to Electron Bernstein and Lower Hybrid Modes

In addition to upper hybrid waves at small wavenumbers, there are also excitations of electron Bernstein waves at large wavenumbers, visible in figures 4.9 and 4.11 at $k \approx 40 - 60 \text{ m}^{-1}$ and frequencies near 2 MHz and 3.4 MHz. These excitations are associated with the first and second electron Bernstein modes seen in figure 4.10. As seen in figure 4.9, an upper hybrid pump wave near 3.44 MHz can decay into frequency downshifted daughter waves on the same electron Bernstein branch at four different wavenumbers, near $\pm 50 \text{ m}^{-1}$ and $\pm 5 \text{ m}^{-1}$, and to lower hybrid waves at four different wavenumbers. We see regions of the frequency-wavenumber spectrum consistent with this decay channel in figure 4.9, and in particular figures 4.11(b) and 4.11(c). Additionally, the high-wavenumber decay modes described here can account for the lower hybrid wavenumber spectrum peaks near $k = 60 \text{ m}^{-1}$ seen in figure 4.8(a), which is not possible to explain by the single or double decay of an upper hybrid wave into upper hybrid and lower hybrid waves.

In figure 4.9, excitations of the first electron Bernstein mode has its maximum intensity near $f = 2 \text{ MHz}$ and $k = 40 \text{ m}^{-1}$. For the pump wave close to 3.44 MHz and with wavenumber $k < 10 \text{ m}^{-1}$, we note that the difference between the second and the first branches of the electron Bernstein modes intersects the first branch

T_e (K)	k_0 (m ⁻¹)	λ_0 (m)
1500	10.38	0.60
4000	6.36	0.99
6000	5.19	1.21

Table 4.2: Upper hybrid wavenumber and wavelength for different electron temperatures, representing the initial temperature 1500 K and higher temperature 4000 K and 6000 K observed later in the simulation.

of the electron Bernstein mode at about 1.7 MHz with $k \approx \pm 50 \text{ m}^{-1}$. Thus, a potential decay mode could be to two Bernstein modes of frequency 1.7 MHz, but with slightly asymmetric wavenumbers near $k = 50 \text{ m}^{-1}$ to satisfy $k_0 = k_{EB,1} + k_{EB,2}$. For a decay of the pump into one wave of 1.72 MHz and $k = 55 \text{ m}^{-1}$, the frequency of the third wave should be $3.44 - 1.72 = 1.72 \text{ MHz}$, while the resulting wavenumber is $7.01 - 55 = -47.99 \text{ m}^{-1}$. These decay products are clearly seen in figure 4.9 where their diffuseness is explained by the temperature dependence of the Bernstein mode dispersion curve shown in figure 4.10. Notably, unlike the first decay channel, figure 4.11 indicates that this mode becomes significantly excited only much later in the simulation, indicating a smaller growth-rate of the instability governing the decay of an upper hybrid wave to two electron Bernstein waves.

4.4.6 Stochastic Heating Mechanism

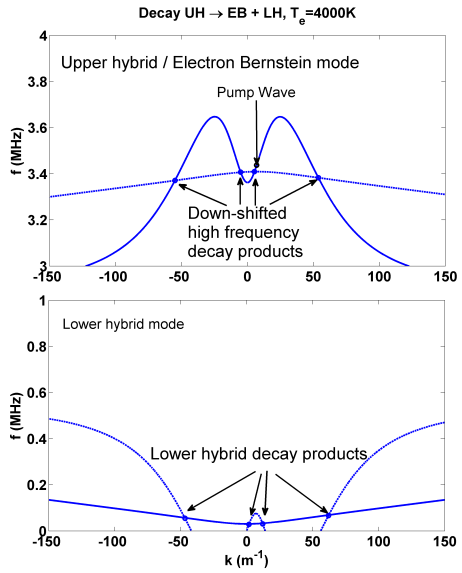
Here we discuss the stochastic heating of electrons by large amplitude electron Bernstein waves. It has been recognized that the acceleration of charged particles

T_e (K)	k_1 (m^{-1})	λ_1 (m)	k_{LH} (m^{-1})	λ_{LH} (m)
1500	-7.68	0.82	18.06	0.35
4000	-4.70	1.34	11.06	0.57
6000	-3.84	1.64	9.03	0.70

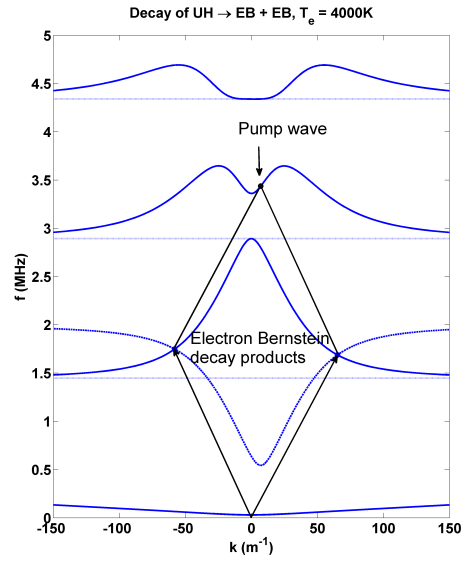
Table 4.3: Daughter upper hybrid, and lower hybrid wavenumber and wavelength for different electron temperatures, representing the initial temperature 1500 K and higher temperature 4000 K and 6000 K observed later in the simulation.

T_e (K)	k_2 (m^{-1})	λ_2 (m)	k_{LH} (m^{-1})	λ_{LH} (m)
1500	4.00	1.57	-11.69	0.54
4000	2.45	2.56	-7.16	0.88
6000	2.00	3.14	-5.84	1.08

Table 4.4: Double decay daughter upper hybrid and lower hybrid wavenumbers and wavelengths for different electron temperatures representing the initial temperature 1500 K and higher temperature 4000 K and 6000 K observed later in the simulation.



(a)



(b)

Figure 4.12: Decay scenarios of a pump upper hybrid wave to (a) either a down-shifted upper hybrid wave or electron Bernstein modes and a lower hybrid wave, and (b), to two electron Bernstein modes.

by electric field gradients perpendicular to a stationary magnetic field can lead to stochastic motion of the individual particles and a rapid heating of the plasma. The equations of motion for a charged particle in the presence of an electrostatic plane wave propagating across the ambient magnetic field can be cast into a dimensionless model problem of the form [59, 58, 60].

$$\frac{d^2v}{dt^2} + v = A \cos(v - \Omega t), \quad (4.23)$$

$$\frac{dx}{dt} = v, \quad (4.24)$$

for the particle's velocity v and position x , where $A = (mk^2\phi)/(qB_0^2)$ is a normalized wave amplitude, $\Omega = \omega/\omega_c$ is the ratio between the wave frequency and cyclotron frequency, and ϕ is the amplitude of the electrostatic potential. For small values of Ω and v , it was noted [60] that stochasticity sets in for $A > 1$. At this value, the particle displacement due to polarization drift becomes comparable to the wavelength of the electrostatic wave, and the drift approximation breaks down. An equivalent condition for stochastic electron and ion heating by large amplitude gradients in the electric field was given by Balikhin et al. [61] and Stasiewicz et al. [62] as

$$|A| = \left| \frac{m}{qB_0^2} \frac{\partial E_x}{\partial x} \right| > 1. \quad (4.25)$$

When this condition is fulfilled [61] the particle orbits, initially very close in phase space, diverge exponentially in time, leading to rapid heating of the particles.

Following the above ideas, we have plotted the normalized electric field gradient

$$A = \frac{m_e}{eB_0^2} \frac{\partial E_x}{\partial x}, \quad (4.26)$$

in figure 4.14. Zooming in on the center of the striation near $t \approx 0.05\text{ms}$, in figures 4.14(b) and 4.14(c), we find $|A| > 1$ which is also correlated with the characteristic turn-on time of both electron heating (figure 4.4(b)) and lower hybrid waves (figure 4.7) in the center of the striation. High-frequency waves escaping the striation are short wavelength electron Bernstein waves, seen in figures 4.14(a) and 4.14(b) for $t > 0.055$ ms. They contribute to the heating of the electrons outside the striation electrons at later times, seen in figure 4.4(a).

By using windowed Fourier transforms in the same manner as in figure 4.11, we can isolate which particular decay modes are associated with the stochastic heating. From figure 4.15, it is evident that the primary contributions to A during the fast heating comes from frequencies near the upper hybrid frequency at a broad spectrum of large wavenumbers. This indicates that the electron heating is due primarily to the decay of upper hybrid modes to short wavelength electron Bernstein waves where the large amplitude electron Bernstein waves lead to stochastic heating of the electrons.

To study the dependence of the electron heating on pump amplitude we have carried out simulations using a series of pump amplitudes between 1.00 V/m and 2.50 V/m. We found that over the course of our simulation time, the average temperature of electrons in the density striation depends non-linearly on the pump field. These results are summarized in figure 4.16. We find that a quadratic fit for the temperature scaling with the pump field yields good agreement.

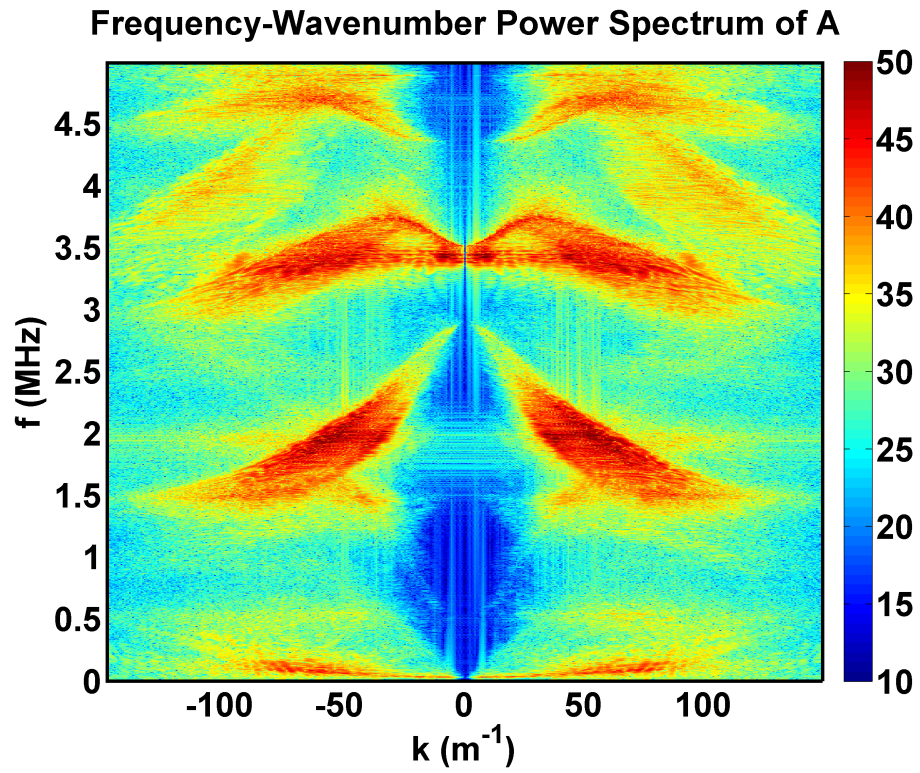
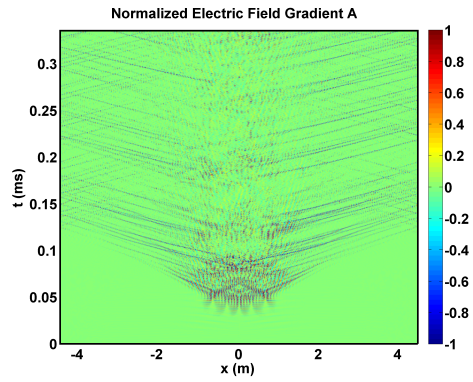
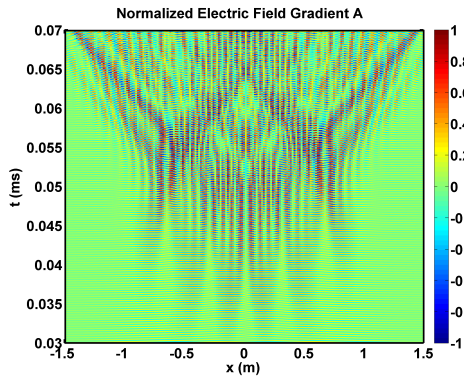


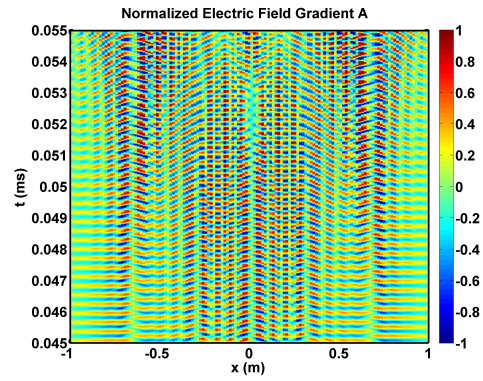
Figure 4.13: Frequency-wavenumber power spectrum of the normalized electric field gradient A ($10 \log_{10}$ scale). The pump wave is seen near $k = 10 \text{ m}^{-1}$ and $f = 3.44$ MHz. Electron Bernstein modes near $k = \pm 50 \text{ m}^{-1}$ and $f = 2.0$ MHz. Lower hybrid waves are visible for $|k| < 100 \text{ m}^{-1}$ and $f < 100 \text{ kHz}$.



(a)



(b)



(c)

Figure 4.14: (a) Colormap of the normalized electric field gradient A from Eq. 4.26.

Panels (b) and (c) show closeups of the initial phase of turbulence.

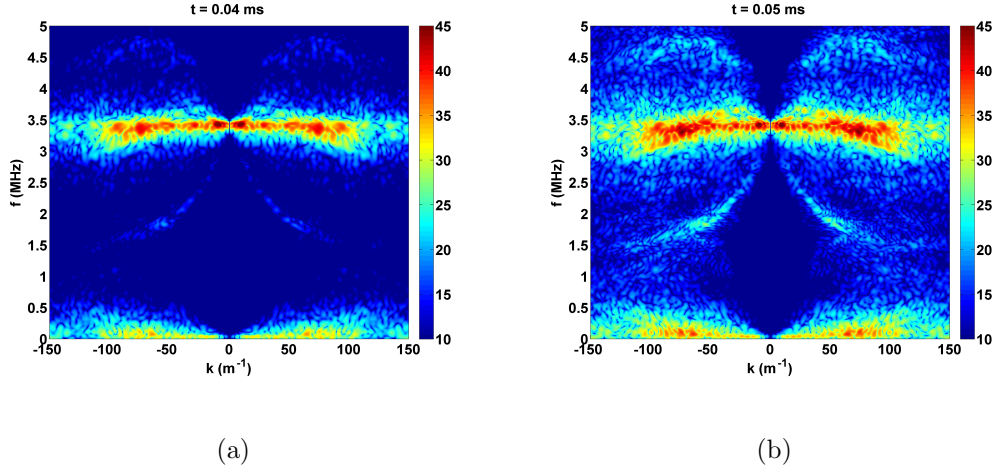


Figure 4.15: Windowed frequency-Wavenumber spectra of the normalized electric field gradient A from Eq.4.26, (a) immediately before heating burst ($t = 0.04$ ms), and (b) during heating burst ($t = 0.05$ ms).

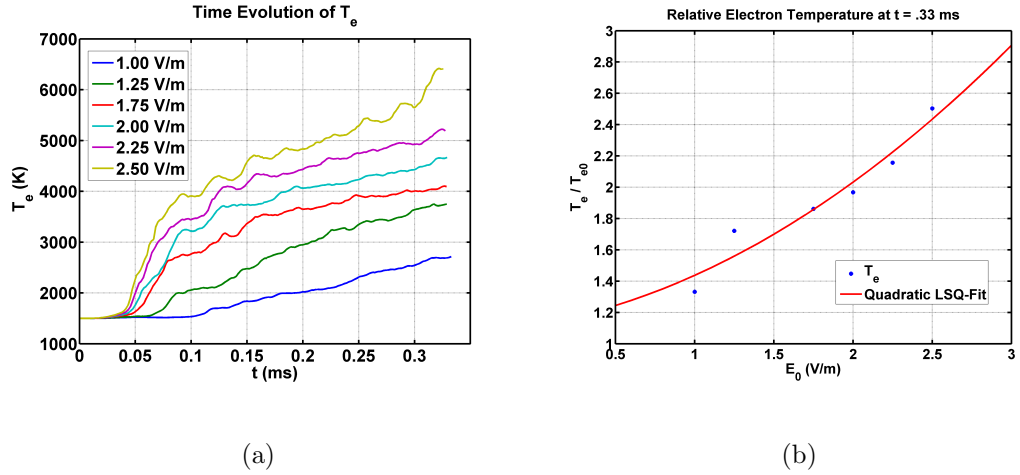


Figure 4.16: Scaling of the electron temperature averaged over space $-1.5 \text{ m} \leq x \leq 1.5 \text{ m}$. (a) Time dependence of T_e for different pump amplitudes and (b) the relative temperature at $t = 0.33$ ms as a function of the pump amplitudes, where the solid line shows the least-squares fit to a quadratic function.

4.4.7 Summary

We have presented the results of Vlasov simulations of ionospheric heating near the upper hybrid resonance layer and in the presence of a small-scale density striation. The pump wave mode-converts to upper hybrid waves trapped in the striation, which in turn decays to high-frequency upper hybrid and electron Bernstein waves and low-frequency lower hybrid waves. The upper hybrid and lower hybrid pairs are responsible for the inverse cascade to small wavenumbers, while the electron Bernstein modes produce high-frequency, large wavenumber components escaping the striation. As the amplitude of the electron Bernstein waves exceeds a threshold of stochasticity, they become the primary source of stochastic electron bulk heating. Further, we find that the average temperature inside the striations exceeds the thresholds proposed by Eliasson et al. [36] for the efficient acceleration of fast electrons by strong Langmuir turbulence in the formation of descending artificial ionospheric layers.

4.5 Resonant Heating

Here we present the results of continued Vlasov and test-particle simulations approaching the simultaneous upper hybrid resonance, and fourth electro gyroharmonic, with pump frequencies $\omega_0/\omega_{ce} = 3.80$ (5.50 MHz) and 4.01 (5.80 MHz).

4.5.1 Vlasov Simulation

Plots of the evolution of the ion density and electron temperature are shown in figure 4.17. For both pump frequencies, ions inside the striation are dominated by standing lower hybrid oscillations with slightly different onset times. For pumping below the gyroharmonic, lower hybrid oscillations maintain constant amplitude from 0.03 ms until the end of the simulation, while pumping above the gyroharmonic has a similar initial onset time, but does not reach full strength until 0.12 ms. In both cases, electrons inside the striation are heated significantly, but heating below the gyroharmonic starts at the edge of the striation and then fills inward and does not exceed about 5000 K. Above the gyroharmonic, heating starts at the center of the striation and turns into a more localized pocket with average kinetic energy exceeding 10000 K.

Plots of both the time evolution of the electric field, and the time averaged frequency-wavenumber spectrum are shown in figure 4.18. Although the pump wave is only 2.0 V/m, in both cases, trapped upper electrostatic upper hybrid oscillations of near 40 V/m evolve from the upper hybrid resonance, and are constrained to the striation. Qualitatively the spectra in figures 4.18(c) and 4.18(d) are similar. In both cases, the pump frequency is visible between 5.50-5.80 MHz and near $k = 0$. Upper hybrid waves extend out from the pump wave frequency to larger wavenumbers, to $k = 50$ for below gyroharmonic heating and only to $k = 20$ for heating above the gyroharmonic. The lower hybrid waves mirror this at ≈ 30 kHz. Bernstein waves that asymptotically approach $N\omega_{ce} = 1.5, 3.0, 4.5, 6.0$ MHz for large wavenumbers

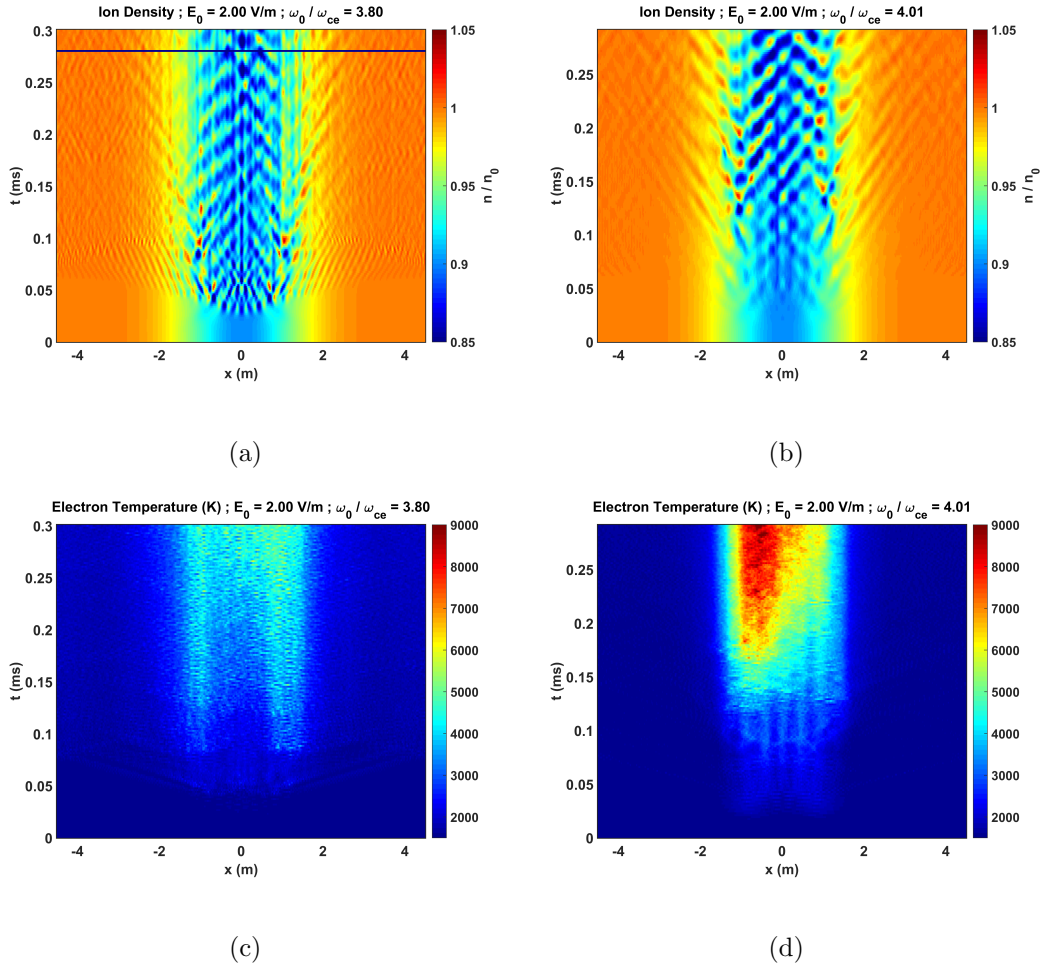


Figure 4.17: Evolution of ion density and electron temperature. Below the gyroharmonic in (a) and (c), above gyroharmonic in (b) and (d).

are present in both cases.

4.5.2 Test-Particle Simulation

Plots of the electron velocity distribution functions for test particles are shown in figure 4.19. For pumping below resonance, we observe bulk heating of the electrons, while for pumping above resonance, only the tail is accelerated. This is a significant difference that does not have an obvious correspondence in the electric

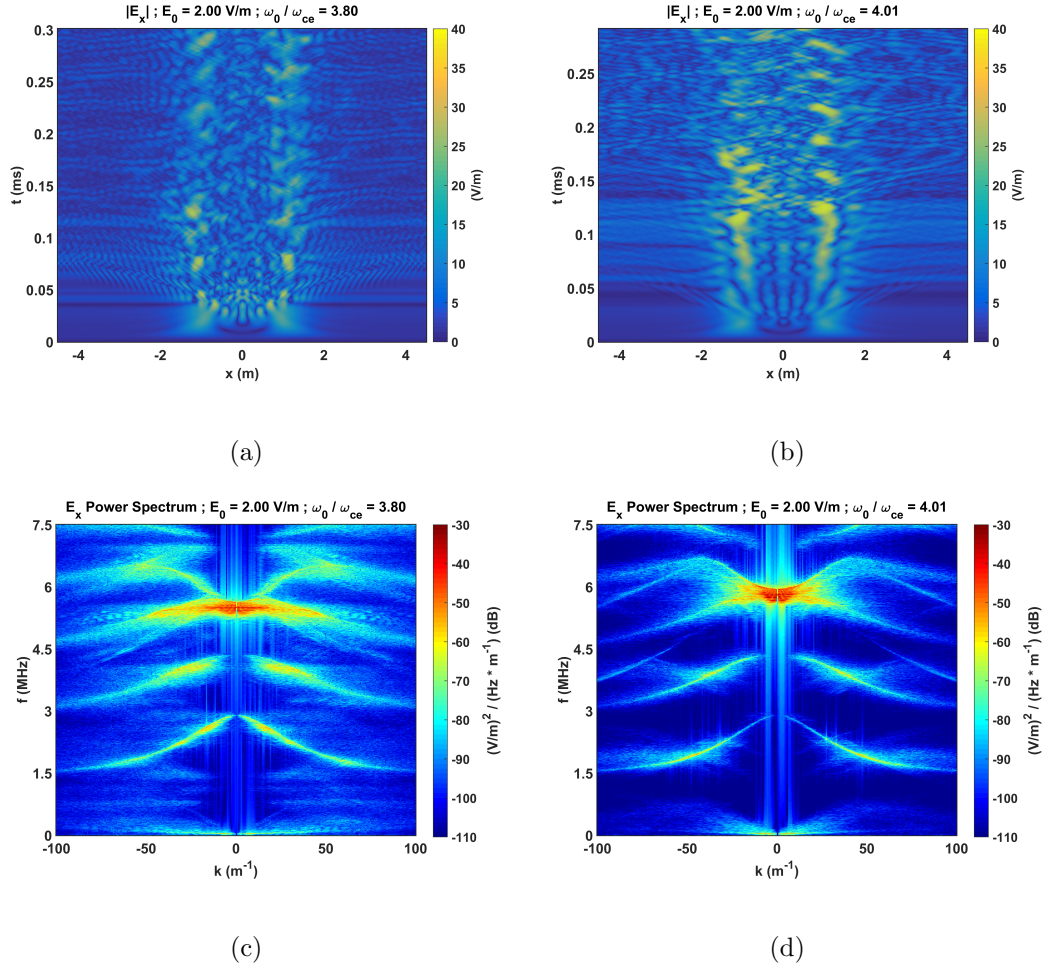


Figure 4.18: Evolution of electric field (a) below gyroharmonic, (c) above gyroharmonic. $\omega - k$ spectrum of electric field (b) below gyroharmonic, (d) above gyroharmonic.

field spectra shown in figure 4.18.

By filtering all but a single wave mode at a time, we can push particles to see the approximate effects of individual wave modes on the electron distribution functions. The results are shown in figure 4.20 where we include a trace for the initial and final v_{avg} distribution with all wave modes, as well as a final distribution with isolated lower hybrid (LH) waves, upper hybrid (UH) waves, and electron Bernstein modes (EBM). For pumping below resonance, the dominant contribution to the bulk heating comes from electron Bernstein waves, while for pumping above resonance the only contribution to the electron tail heating comes from upper hybrid waves.

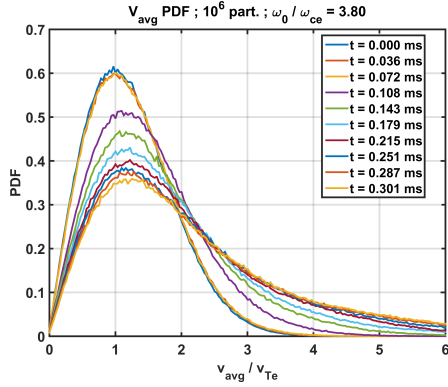
Although the electric field spectra seen in figure 4.18 are qualitatively similar for each of the pump frequencies, they produce distinct particle distribution functions. Figures 4.18(c) and 4.18(d) indicate the presence of upper hybrid waves and electron Bernstein waves in both simulations, but there is only bulk heating for the below resonance simulation, and only tail heating for the above resonance simulation.

By projecting into frequency space we can see many differences between the overall spectra. This projection is shown in figure 4.21, with the overall frequency spectra shown in figure 4.21(a), while a focus on the electron Bernstein wave spectra with labeled features is shown in figure 4.21(b) and a similar focus on the upper hybrid spectra is shown in figure 4.21(c). The region from 1.5 MHz to 3.0 MHz corresponds to the first electron Bernstein wave. For $\omega_0/\omega_{ce} = 3.80$, there are peaks near 1.8, 2.2, and 2.6 MHz, while for $\omega_0/\omega_{ce} = 4.01$, there are peaks only at 1.8 and 2.2 MHz. We can isolate the electric field due to each of these peaks and

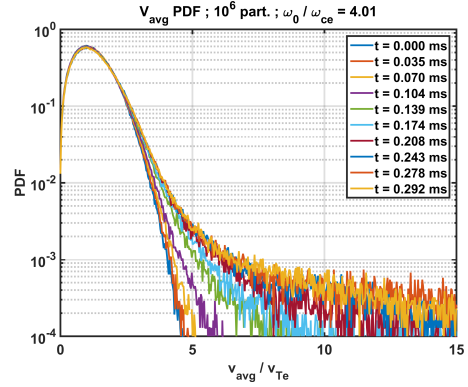
run the test-particle simulations to estimate the relative contribution of each peak to the final electron distribution function. The results are shown in figure 4.22(a) we find that the peak at 2.6 MHz, which is present in the below resonance heating, and absent in the above resonant heating, is the primary driver of bulk electron heating. We can do a similar analysis on the upper hybrid spectrum seen in figure 4.21(c). The region from about 5.4 MHz to 6 MHz comprises the bulk of the upper hybrid wave spectrum for each case. For each heating frequency, we have indicated both the pump frequency and a number of downshifted maxima or peaks (DM) mutually separated from the pump by the lower hybrid frequency. For the case of a pump near $\omega_0/\omega_{ce} = 4.01$, the pump and its associated DMs are between 10-40 dB greater than the spectra of the $\omega_0/\omega_{ce} = 3.80$ in the same frequency range. We can isolate the electric field due to each of these downshifted maxima and estimate their contribution to the final electron distribution function as before. The results are shown in figure 4.22(b). We find that the primary contributions to the long tail of the electron distribution comes from the first downshifted maximum, closest to the pump frequency, and secondarily, due to the pump itself. Both the pump and the first downshifted maxima bracket the fourth gyroharmonic $4\omega_{ce} = 5.79$ MHz.

4.5.3 Heating Wave Modes

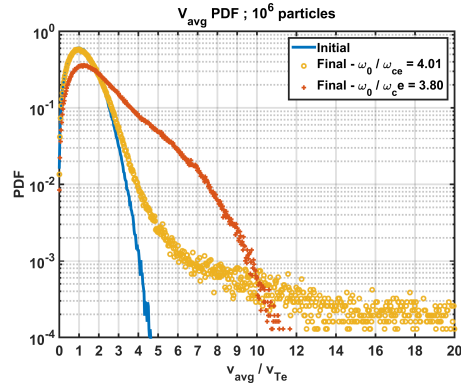
In the previous section, we have shown the effects of the electric fields on the distribution function of the electrons, and by extending this analysis to the particle phase and configuration spaces we can learn more about the heating mechanism. In



(a)

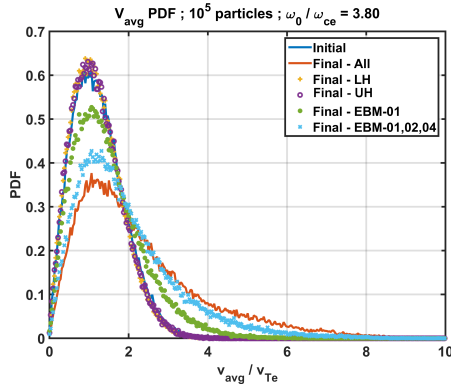


(b)

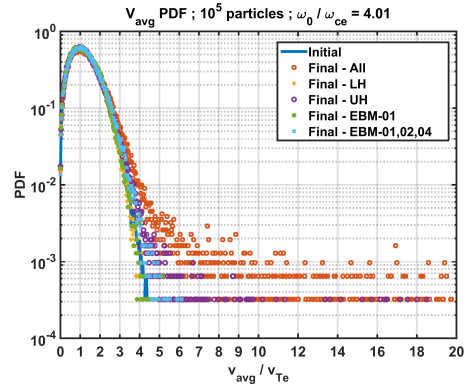


(c)

Figure 4.19: Evolution of average electron velocity distribution for $\omega_0/\omega_{ce} =$ (a) 3.80 on linear scale and (b) 4.01 on log scale to illustrate the long tail. (c) initial and final distributions from both pump frequencies on log-scale.

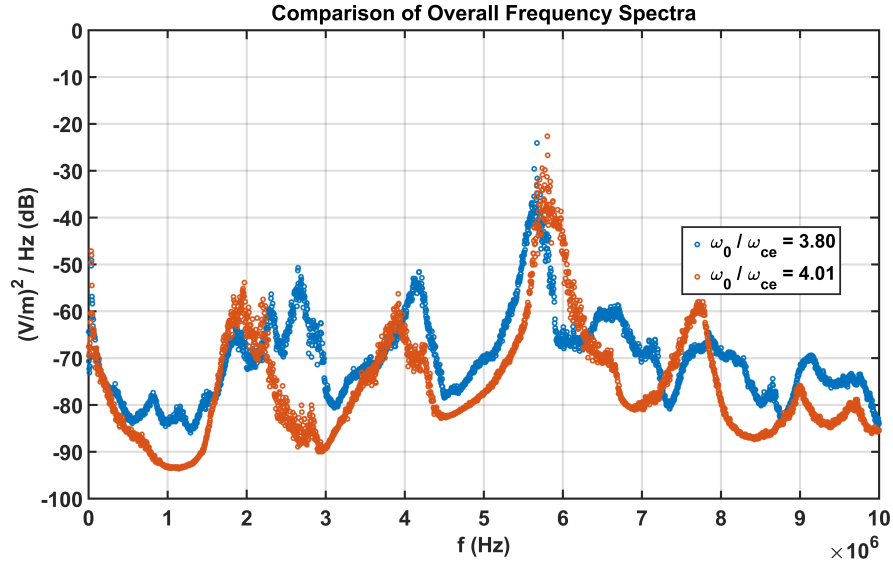


(a)

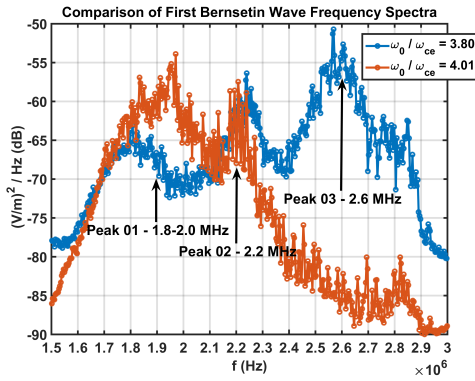


(b)

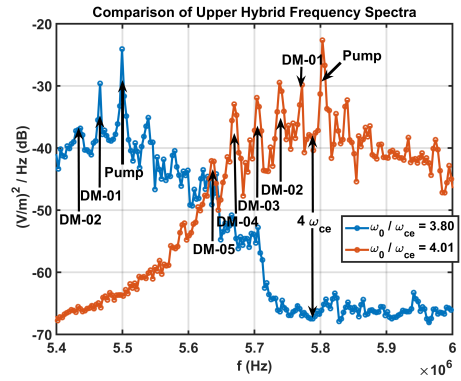
Figure 4.20: Evolution of average electron velocity distribution with initial and final distributions for all wave modes, as well as final distributions with individual wave modes for $\omega_0/\omega_{ce} =$ (a) 3.80, and (b) 4.01. Each plot includes traces with the initial distribution, final distribution with all wave modes, final distribution with only the lower hybrid (LH), upper hybrid (UH), first electron Bernstein mode (EBM-01) and higher order Bernstein modes.



(a)



(b)



(c)

Figure 4.21: Comparison of frequency spectra for the $\omega_0/\omega_{ce} = 3.80$ and 4.01 . The overall frequency range from 0-10 MHz is given in (a), while a zoom in on the 1.5-3.0 MHz, corresponding to the first electron Bernstein wave and 5.4-6.0 MHz, corresponding to the upper hybrid frequencies are seen in (b) and (c) respectively.

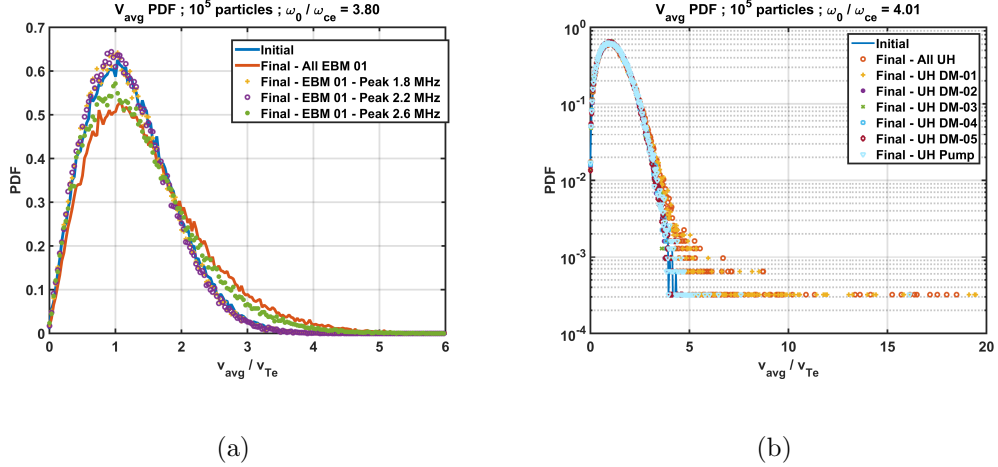


Figure 4.22: Test particle v_{avg} distributions for (a) $\omega_0/\omega_{ce} = 3.80$ showing that the primary contribution to the bulk heating from the electron Bernstein waves comes from the peak near 2.6 MHz, and (b) $\omega_0/\omega_{ce} = 4.01$ showing that the primary contribution to long-tail acceleration comes from upper hybrid waves near the pump and the first DM.

figure 4.23 we show the initial and final $x - v_{avg}$ phase space of electrons for each of the two pump waves we have considered above. In both cases, heated particles are primarily drawn from those inside the striation ($-1.5 < x < 1.5$). For the below resonant pump, particles initially occupying phase space from $-1.5 < x < 1.5$ and $0 < v_{avg} < 2v_{Te}$ have been pushed up into $2 < v_{avg} < 7v_{Te}$, while particles outside the striation or with initial velocity greater than about 3-5 v_{Te} experience little or no acceleration. For the pumping above resonance, it is a small number of already fast particles that are further accelerated. Particles with small initial velocities are ignored no matter where in the striation they are.

We can further focus our attention to a sample particle that is heated. In figure 4.24, we show $v_x - v_y$ phase space trajectories for a selected particle in 4.24(a) and

4.24(b), and then the time dependence of v_{avg} for those same particles in 4.24(c) and 4.24(d). These plots show the difference between the more steady bulk heating of an initially slow particle in the below resonance pump, and the discrete "kicks" received by an initially fast particle in the above resonance pump. Most interestingly, figures 4.24(c) and 4.24(d) give enough information to estimate an onset time that can be correlated with electric field data. For $\omega_0/\omega_{ce} = 3.80$, the onset of bulk heating comes after ≈ 0.07 ms, while for $\omega_0/\omega_{ce} = 4.01$, the resonant acceleration does not begin until $\approx 0.12 - 0.15$ ms.

In figure 4.25 we show the initial evolution of the electric field spectrum, by taking 2D Fourier transforms after applying a Gaussian window centered on the bottom of the striation, $x = 0$ m, with $\sigma_x = 1.0$ m, and centered on 0.00 ms for 4.25(a) and 4.25(b) time, and centered on 0.03 ms for 4.25(c) and 4.25(d) with $\sigma_t = 0.005$ ms in each case. At 0.03 ms, the below resonant pumping has developed a broad wavenumber spectrum of upper hybrid and lower hybrid waves, while the above resonant case has developed a very narrow upper and lower hybrid spectrum while simultaneously exciting all of the first four electron Bernstein waves. In figure 4.26, we see the further development of the electric field spectra in the neighborhood of the onset times noted from the test-particle simulations above. We employ the same Gaussian window, advancing the time center through the times of interest. In figures 4.26(a), 4.26(c), and 4.26(e), the first Bernstein wave is absent at 0.05 ms, but starts to develop at 0.07 ms, and is fully formed by 0.09 ms, consistent with the observed heating onset time of ≈ 0.07 , and also with the observation that the first Bernstein wave is a primary driver of bulk heating. In figures 4.26(b), 4.26(d),

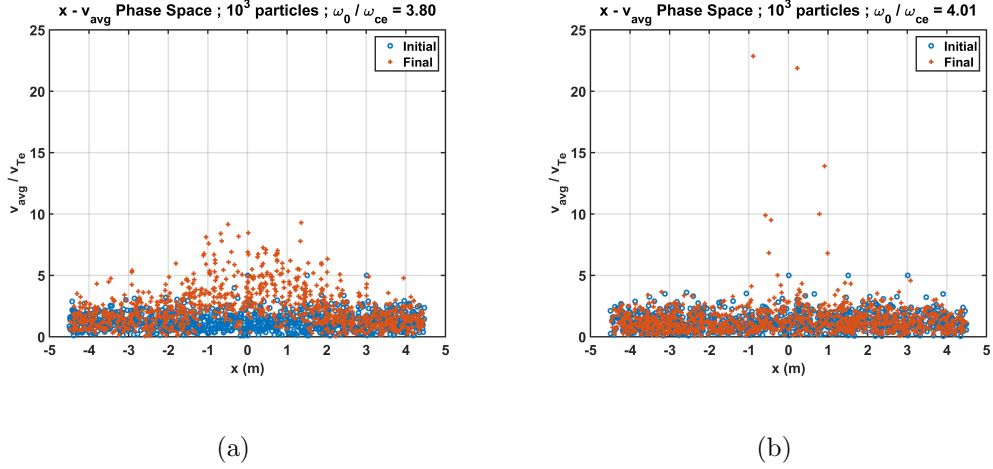


Figure 4.23: Initial and final $x - v_{avg}$ phase space for pump wave (a) below resonance, and (b) above resonance. In both cases, heated particles are drawn from within the striation ($-1.5 < x < 1, 5$) while particles outside the striation are mostly unperturbed.

and 4.26(f), the upper and lower hybrid spectra grow sharply in both amplitude and wavenumber from 0.09 ms, expanding the upper hybrid spectrum to nearly $k = 50 \text{ m}^{-1}$ at 0.15 ms, consistent with the observed heating onset in test particle simulations of $\approx 0.12 - 0.15$ ms, and also with the upper hybrid spectrum near $4 \omega_{ce}$ as the primary cause of tail heating.

The onset times from the test-particle simulations are also consistent with the onset of wave modes from the Vlasov simulations. In figure 4.17, the ion density fluctuations have distinct onset times, with stationary lower hybrid oscillations from about 0.03 ms onward for $\omega_0/\omega_{ce} = 3.80$, and some oscillations visible at 0.05 ms, but not fully developed until $\approx 0.12 - 0.15$ ms for $\omega_0/\omega_{ce} = 4.01$.

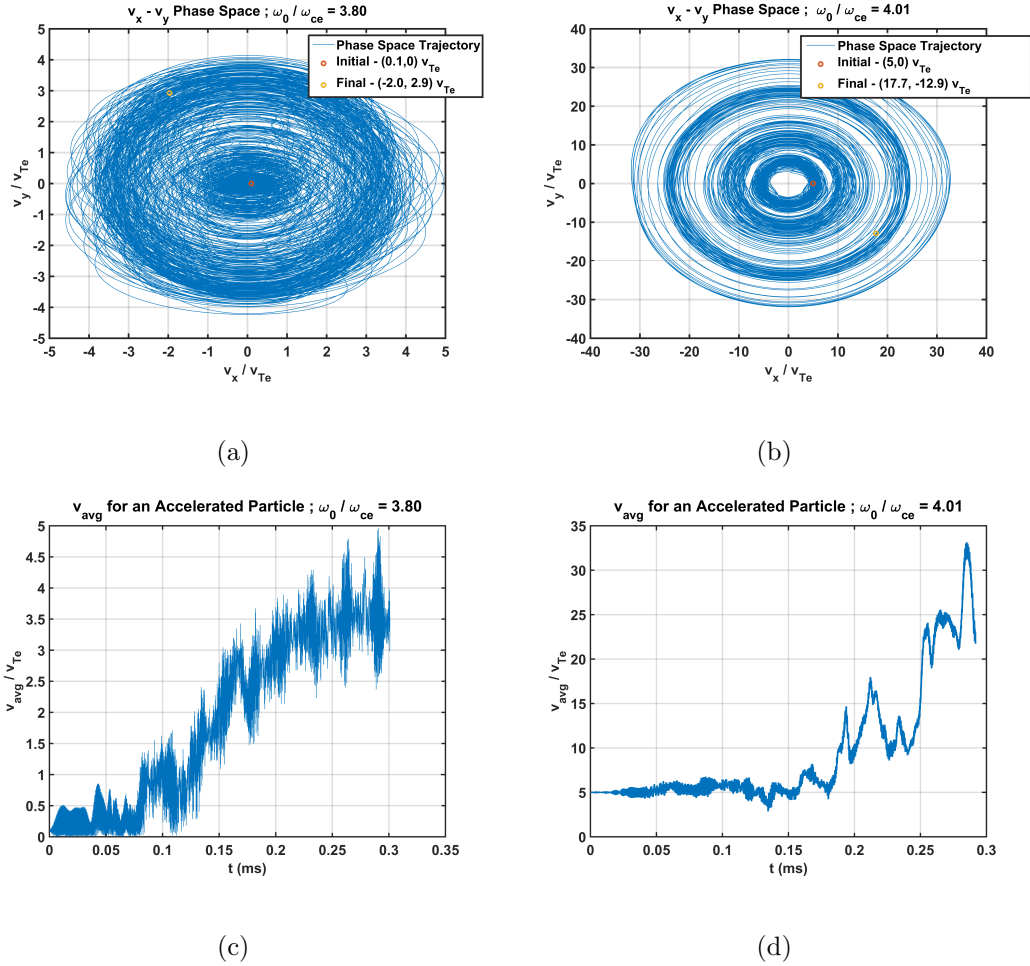


Figure 4.24: Phase space and v_{avg} time dependence for a sample heated particle in each pump wave. In (a) and (c) an initially cold particle on the edge of the striations in the below resonant pump, is steadily heated to several times v_{Te} after an onset time of ≈ 0.07 ms. In (b) and (d), an initially fast particle is resonantly accelerated to over $20 v_{Te}$ in discrete steps that occur after an onset time of ≈ 0.15 ms.

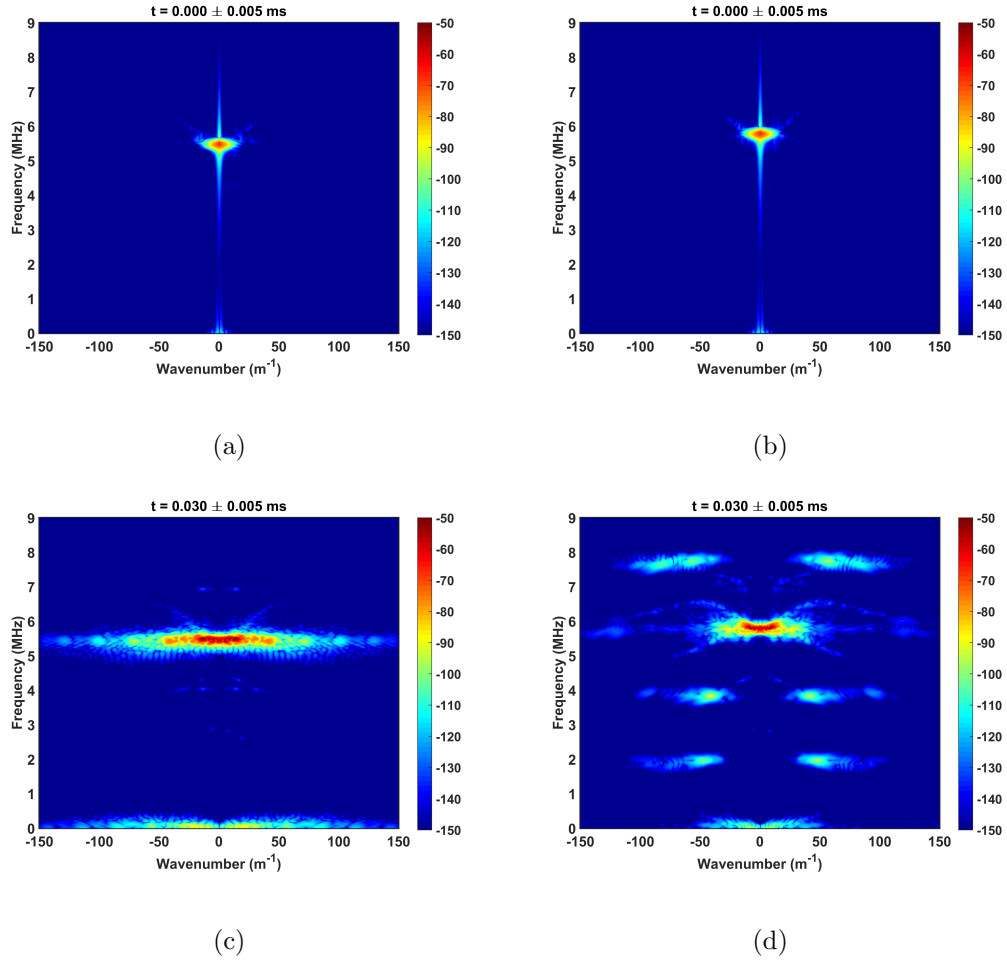


Figure 4.25: Frequency-Wavenumber spectra of electric field data from Vlasov simulations. Gaussian window centered $x = 0$ m, with $\sigma_x = 1.0$ m, $t = 0.00$ and 0.03 ms, and $\sigma_t = 0.005$ ms. (a) and (c) show the spectra for pump wave below resonance, while (b) (d) show the spectra for pump wave above resonance.

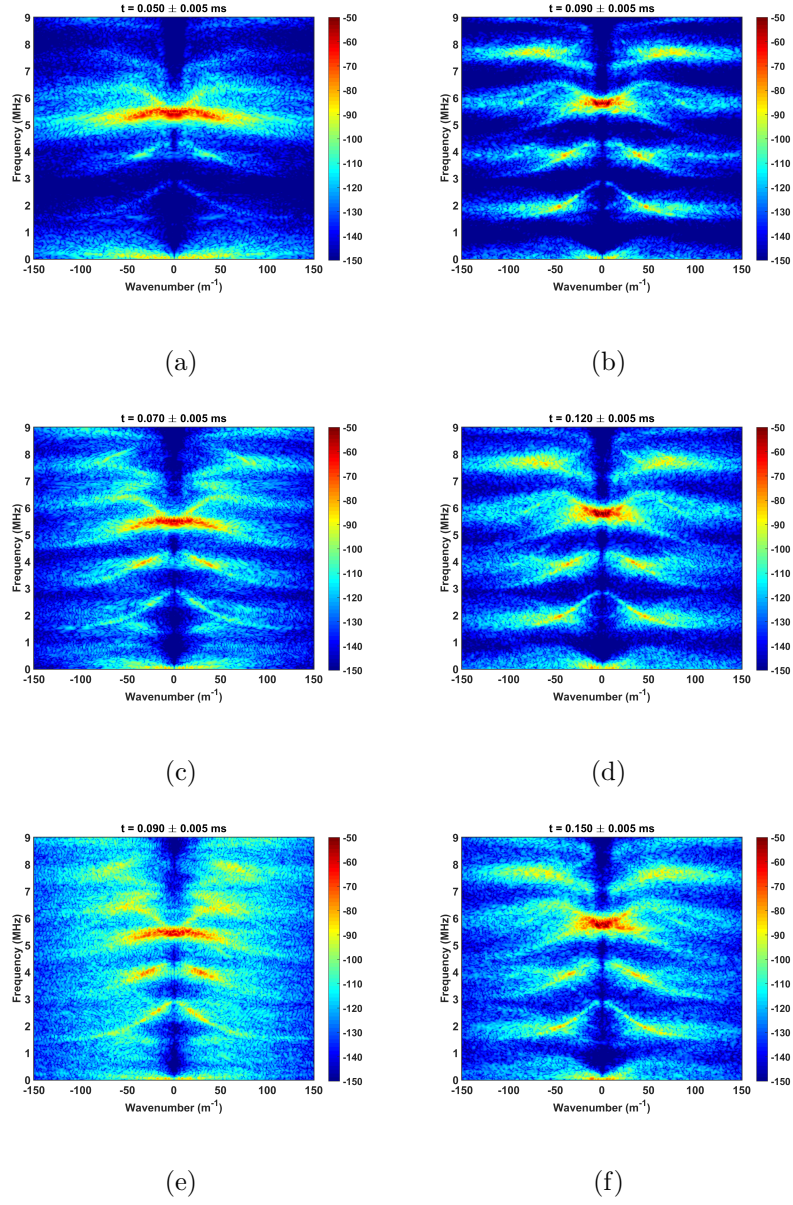


Figure 4.26: Frequency-Wavenumber spectra of electric field Gaussian window centered $x = 0$ m, with $\sigma_x = 1.0$ m, t is indicated in each figure, and $\sigma_t = 0.005$ ms. (a), (c), and (e) show the development of the first electron Bernstein wave near $t = 0.07$ ms for $\omega_0/\omega_{ce} = 3.80$. (b), (d), and (f) show the development of broader wavenumber spectrum and larger amplitude upper hybrid and lower hybrid waves near $t = 0.12$ ms for $\omega_0/\omega_{ce} = 4.01$.

4.5.4 Excitation of Electron Bernstein waves

We have identified the specific wave mode associated with bulk heating as the high frequency 2.6-2.7 MHz peak of the first electron Bernstein wave. In figure 4.27 , we show the frequency-wavenumber spectrum of the first electron Bernstein wave for both pump frequencies. To excite this wave, we consider the linear mode conversion of the pump wave (E_0, ω_0) to upper hybrid waves as the edge of the density cavity where $n = 0.95n_0$ and a subsequent three-wave decay obeying the matching condition

$$\omega_0 = \omega_1 + \omega_2, \quad (4.27)$$

$$k_0 = k_1 + k_2. \quad (4.28)$$

for frequency and wave number. A direct decay from a mode converted upper hybrid pump wave at $\omega_0 = 3.80\omega_{ce} = 5.50$ MHz to two electron Bernstein waves of frequency 2.6-2.7 MHz (see peak 03 from figure 4.21(b)) is prohibited by frequency matching. However, if the pump wave first decays to upper hybrid and lower hybrid waves, and then a daughter upper hybrid wave decays to two electron Bernstein waves, frequency matching could be satisfied, and this would also explain the observed onset time of electron Bernstein waves after the formation of a broad wavenumber spectrum of upper and lower hybrid turbulence.

Following the work previously developed in Najmi et al. [71], we consider a mode converted upper hybrid wave that propagates to the center of the striation and undergoes a three-wave decay to a daughter upper hybrid wave and a lower

hybrid wave. The frequency difference between the pump frequency and the local upper hybrid frequency at the bottom of the cavity is given by

$$\begin{aligned}\Delta\omega &= \sqrt{0.95\omega_{pe}^2 + \omega_{ce}^2} - \sqrt{0.90\omega_{pe}^2 + \omega_{ce}^2}, \\ &= 136.38 \text{ kHz.}\end{aligned}\tag{4.29}$$

The lower hybrid frequency (ω_{LH}) is given in section 4.2 as 32.64 kHz, and $\Delta\omega/\omega_{LH} = 4.18$, giving enough room in frequency space for the possibility of up to four successive decays of an upper hybrid wave to a downshifted upper hybrid wave, with a downshift equal to the lower hybrid frequency. To find the frequency and wavenumber of the daughter upper hybrid waves, we take the dispersion relation for upper hybrid waves given by [68]

$$\omega^2 = \omega_{UH}^2 + \frac{3v_{Te}^2 k^2 \omega_{pe}^2}{\omega^2 - 4\omega_{ce}^2},\tag{4.30}$$

and substitute both the frequency matching condition (Eq. 4.27), and the local upper hybrid frequency, assuming that the bottom of the density cavity is homogenous to first order. The N^{th} daughter upper hybrid wave ($\omega_0 - N\omega_{LH}, k_N$) has dispersion relation

$$(\omega_0 - N\omega_{LH})^2 = 0.9\omega_{pe}^2 + \omega_{ce}^2 + \frac{3v_{Te}^2 k_N^2 \omega_{pe}^2}{(\omega_0 - N\omega_{LH})^2 - 4\omega_{ce}^2},\tag{4.31}$$

For $N = 4$, we have $\omega_4 = 5.37$ MHz, $k_4 = 5.12 \text{ m}^{-1}$. The frequency ω_4 can satisfy the frequency matching condition for decay to two Bernstein waves with frequencies 2.6-2.7 MHz since $\omega_4/2 = 2.68$ MHz, and the wavenumber k_4 can satisfy the wavenumber matching condition for waves from $k = 15\text{-}20 \text{ m}^{-1}$ which are the observed ranges of the third peak of the first Bernstein wave seen in figure 4.27(a)

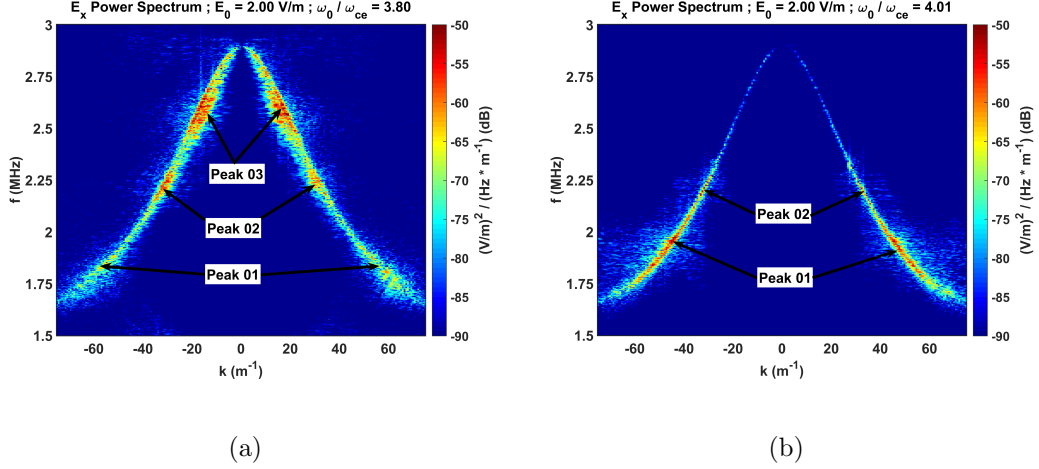


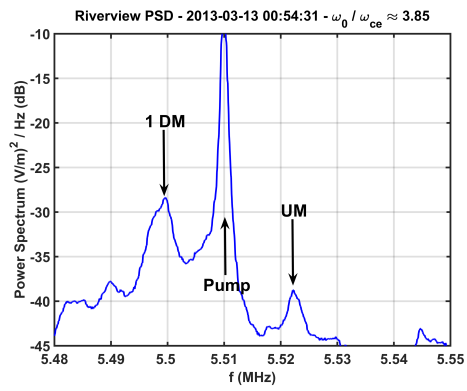
Figure 4.27: Frequency-Wavenumber plot for the first electron Bernstein wave (a) below resonance, and (b) above resonance. Peaks corresponding to figure 4.21(b) are indicated. Peak 03 of (a), previously associated with the bulk heating of electrons corresponds to a frequency of 2.6-2.7 MHz and a wavenumber of 15-20 m⁻¹.

For the case of $\omega_0/\omega_{ce} = 4.01$, we can use this same procedure to show that a decay is prohibited. $\Delta\omega/\omega_{LH} = 4.43$, $\omega_4 = 5.67$ MHz, which is prohibited by the frequency matching condition to decay to two electron Bernstein waves of 2.6-2.7 MHz.

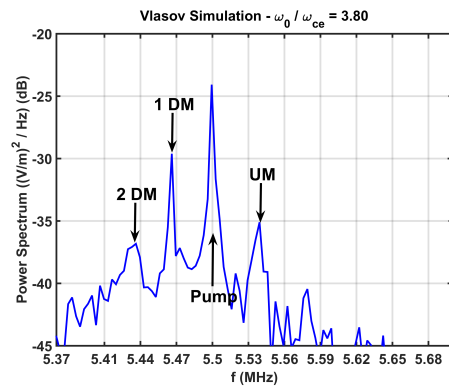
4.5.5 Comparison with Experiments

A significant motivation for exploring the mechanism of heating near the double resonance of the fourth gyroharmonic and the upper hybrid layer is that this frequency range has been explored by experiments that can ground our simulations. In previous work, [45] we performed heating at the HAARP facility stepping an O-mode pump wave from 300 kHz below, to 200 kHz above, the fourth gyroharmonic, while simultaneously remaining below the F_2 critical layer to be near the upper

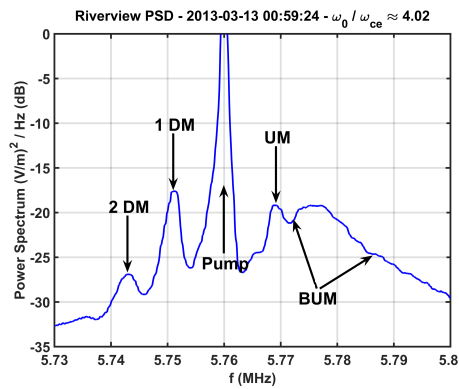
hybrid resonance. While there were no electric field measurements in the heated region, instruments operated by the Naval Research Laboratory (NRL) were able to detect Stimulated Electromagnetic Emissions (SEE) on the ground, approximately 200 km below the heated region. We show spectra obtained from the SEE measurements alongside electric field spectra from our Vlasov simulations at similar pump frequencies in figure 4.28, and these results correlate strongly with the simulations. As mentioned previously, in the F-region, the dominant ion species is atomic oxygen, which is 9 times heavier than the proton mass used in our simulations, and has a corresponding lower hybrid frequency of $1/\sqrt{9} = 1/3$ of our simulation value of ≈ 32 kHz. Therefore, while our simulations show a separation between the pump and the DMs of ≈ 32 kHz, the separation from the NRL data shows a separation of ≈ 10 kHz, and this discrepancy is expected. For the below resonance cases, compared in 4.28(a) and 4.28(b), there is a clear pump wave, a DM separated from the pump by the appropriate lower hybrid frequency, and an upshifted maximum (UM) that is upshifted by a similar amount. In the above resonance case, shown in figures 4.28(c) and 4.28(d) additional DMs are visible, and there is also a broad upshifted component associated with the fourth electron Bernstein wave. Previous SEE measurements have concentrated on the narrow range of 300-400 kHz around the pump frequency. In future experiments, we have proposed that the frequency range be expanded to 3-4 MHz to allow for the detection of electron Bernstein waves, which our simulations predict should be present in experiments where the pump wave is absorbed between the upper hybrid layer and the F_2 peak.



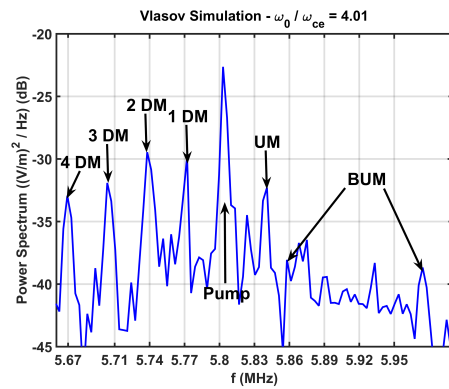
(a)



(b)



(c)



(d)

Figure 4.28: Comparison of SEE from (a) and (a) ground based detectors, with (b) and (d) simulation results for similar pump frequencies.

4.5.6 Strong Langmuir Turbulence

The original motivation for exploring heating near the upper hybrid layer, was to use this as an initial condition for strong Langmuir turbulence in the theory of formation of DAILs. Since we are able to obtain velocity distribution functions at various heating frequencies, we can use these distribution functions as inputs to strong Langmuir turbulence simulations such as those described in Eliasson et al. [36]. The most interesting comparison is between the thermal distributions used by the authors, and the non-Maxwellian long-tail distributions described by our Vlasov simulations of heating above the gyroharmonic. We present two comparisons, with strong Langmuir turbulence produced by an HF pump corresponding to 1.0 V/m and 2.0 V/m. These results are shown in figure 4.29 with velocities normalized to $v_{Te} = 1500K$, the same initial temperature of electrons in the Vlasov simulations presented above. For each pump field, we show four traces, the initial and final v_x distribution function corresponding to the Vlasov simulation, and to a thermal distribution of 4500 K which was previously studied by Eliasson et al. [36]. The threshold for ionization of neutrals in the F region is about 10 eV, which corresponds to 9-10 v_{Te} , and in both cases, a long tail develops that exceeds this threshold, with ten times more particles with velocities greater than $10v_{Te}$ with a pump field of 2.0 V/m as compared to 1.0 V/m. With a pump field of 1.0 V/m, the distribution obtained from Vlasov simulations produces more hot electrons, and at a higher cut-off ($40v_{Te}$ compared to $60v_{Te}$) as compared with the 4500 K Maxwellian distribution. For the pump field of 2.0 V/m, the Maxwellian produces more hot

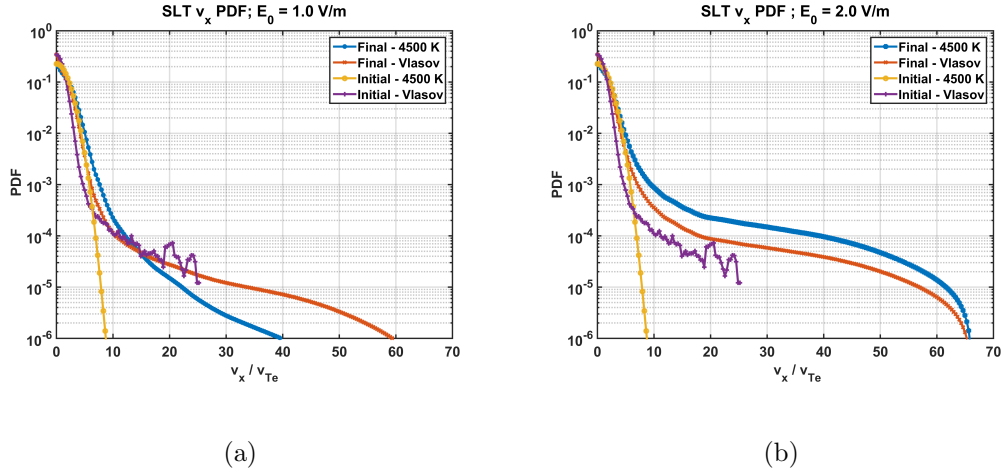


Figure 4.29: Electron velocity distribution functions normalized to v_{Te} corresponding to 1500 K for a strong Langmuir turbulence produced by a HAARP pump wave of (a) 1.0 V/m, (b) 2.0 V/m. Threshold for ionization is 9-10 v_{Te} .

electrons, but cut-offs are similar, close to $65v_{Te}$. Future DAIL production experiments could explore this further, we propose that heating close to and above the fourth gyroharmonic might be able to produce DAILS at lower heater ERPs, than heating between gyroharmonics, and should be comparable for higher ERPs.

4.6 Conclusions

We have presented the results of Vlasov and test-particle simulations and showed that there is heating of electrons inside density cavities that changes from a bulk heating when the pump frequency is below the a gyroharmonic, to a long tail acceleration when the pump frequency is above a gyroharmonic. We found that each type of heating is associated with a different set of waves. The bulk heating is driven by electron Bernstein waves near 2.6 MHz, and not directly by upper hybrid

waves, even though the Bernstein waves are nearly 20 dB lower amplitude. The tail acceleration is a resonant effect caused by upper hybrid waves if within 10-20 kHz of $4\omega_{ce}$. Our current simulations are in good agreement with experiments performed in similar parameter spaces, and we have provided predictions on the detection of broader band Stimulated Electromagnetic Emission for future experiments. We have applied the results of our Vlasov simulations to strong Langmuir turbulence in the formation of DAILs, and found that for lower heater ERPs, the long tail associated with heating above the gyroharmonic may produce DAILs where heating between gyroharmonics might be close to, or below the DAIL formation threshold.

Chapter 5: Conclusions

We have presented a number of novel results deriving from the artificial modification of the F region ionosphere near the upper hybrid layer. These include the first experimental observations of super small striations (SSS) excited by the High-Frequency Auroral Research Project (HAARP), the first detection of high-frequency (HF) waves from the HAARP transmitter over a distance of 16×10^3 km, the first simulations indicating that upper hybrid (UH) turbulence excites electron Bernstein waves associated with all gyroharmonics, and the first simulations that indicate that the resulting bulk electron heating is due primarily to electron Bernstein waves near the first gyroharmonic.

Chapter 2 presented the results of heating experiments at HAARP that resulted in the first detection of super-small striations (SSS). By combining a number of satellite and ground based diagnostics that included GPS flyover, ground-based stimulated electromagnetic emission (SEE) detectors, and HAARP's ionosonde, we were able to detect the effects of these striations, as well as observe a hysteresis effect for key SEE spectral features.

In chapter 3, we introduced a novel diagnostic, ground based receivers located 16 Mm away from HAARP at the Ukrainian Antarctic Station (UAS) in Verdansky.

These experiments resulted in the first detection of a signal from HAARP injected into the ionospheric waveguide by direct scattering off of dekameter scale density structures directly above HAARP. They also detected for the first time, a 90% saturation of SEE features at 50% of HAARP's maximum ERP. This threshold had been inaccessible to experiments at other facilities which were limited to 25% of HAARP's maximum ERP.

Chapter 4 described the results of Vlasov simulations of the upper hybrid layer. We found that in parameter ranges accessible to HAARP, bulk heating of electrons inside meter scale density structures was possible, and consistent with heating required by models of descending artificial ionized layer (DAIL) formation. Further simulations showed that the heating changes from a bulk heating when the pump frequency is below the fourth gyroharmonic, to a tail acceleration when the pump frequency is above the fourth gyroharmonic. Our test particle simulations allowed us to isolate the effects of specific wave modes, and we found that the bulk heating is driven by electron Bernstein waves particularly those near the first gyroharmonic, while the tail acceleration is caused by upper hybrid waves near the fourth gyroharmonic. Our current simulations are in good agreement with our previous experiments performed in similar parameter spaces, and we have provided predictions on the detection of broader band SEE for future experiments. Finally, we have applied the results of our Vlasov simulations as input to codes simulating strong Langmuir turbulence (SLT) and the formation of DAILs, and found that for lower heater ERPs, the long tail associated with heating above the gyroharmonic may produce DAILs where heating between gyroharmonics might be at or below

the DAIL formation threshold.

Bibliography

- [1] F.F. Chen. *Introduction to Plasma Physics*. Springer US, 1984. doi: 10.1007/978-1-4757-5595-4.
- [2] M. C. Kelley. *The Earth's Ionosphere: Plasma Physics and Electrodynamics*, volume 96. Academic Press, 2 edition, 2009.
- [3] W.G. Baker and D.F. Martyn. Electric Currents in the Ionosphere I. The Conductivity. *Phil. Trans. Royal Soc. London Series A. Math. Phys. Sci.*, 246 (913):281–294, Dec 1953. doi: 10.1098/rsta.1953.0016.
- [4] P.O. Pedersen. *The propagation of radio waves along the surface of the earth and in the atmosphere*. GAD, 1927.
- [5] S.J. Briczinski, P.A. Bernhardt, C.L. Siefring, S.M. Han, T.R. Pedersen, and W.A. Scales. Twisted beam see observations of ionospheric heating from haarp. *Earth, Moon, Planets*, 116(1):55–66, 2015. ISSN 0080-4630. doi: 10.1007/s11038-015-9460-3.
- [6] I. Lassen, H. *Zeitschrift fr Hochfrequenztechnik*, volume 28. 1926.
- [7] D. B. Muldrew. Characteristics of the coupled z mode at arecibo. *Radio Science*, 28(3):379–388, 1993. ISSN 1944-799X. doi: 10.1029/92RS00273.
- [8] B. Lundborg and B. Thide. Standing wave pattern of HF radio waves in the ionospheric reflection region: 2. applications. *Rad. Sci.*, 21(3):486–500, 1986. ISSN 1944-799X. doi: 10.1029/RS021i003p00486.
- [9] R. Cohen and J.D. Whitehead. Radio-reflectivity detection of artificial modification of the ionospheric f layer. *J. Geophys. Res.*, 75(31):6439–6445, 1970. doi: 10.1029/JA075i031p06439. URL <http://dx.doi.org/10.1029/JA075i031p06439>.
- [10] P. Stubbe, H. Kopka, T.B. Jones, and T. Robinson. Wide band attenuation of radio waves caused by powerful hf waves: Saturation and dependence on ionospheric variability. *J. Geophys. Res.*, 87(A3):1551–1555, 1982. doi: 10.1209/JA087iA03p01551.

- [11] T.B. Jones, T.R. Robinson, P. Stubbe, and H. Kopka. Frequency dependence of anomalous absorption caused by high power radio waves. *J. Atmos. Terr. Phys.*, 46(2):147–153, 1984.
- [12] M.C. Kelley, T.L. Arce, J. Salowey, M. Sulzer, W.T. Armstrong, M. Carter, and L. Duncan. Density depletions at the 10-m scale induced by the arcibo heater. *J. Geophys. Res.*, 100(17367), 1995. doi: 10.1029/95JA00063.
- [13] K.B. Dysthe, E. Mjølhus, H.L. Pecseli, and K. Rypdal. Thermal cavitons. *Phys. Scr.*, T2B(548), 1982. doi: 10.1088/0031-8949/1982/T2B/040.
- [14] A. V. Gurevich, K. P. Zybin, and A. V. Lukyanov. Stationary striations developed in the ionospheric modification. *Phys. Rev. Lett.*, 75:2622–2625, 1995. doi: 10.1103/PhysRevLett.75.2622.
- [15] M. T. Rietveld, M. J. Kosch, N. F. Blagoveshchenskaya, V. A. Kornienko, T. B. Leyser, and T. K. Yeoman. Ionospheric electron heating, optical emissions, and striations induced by powerful hf radio waves at high latitudes: Aspect angle dependence. *J. Geophys. Res. Space*, 108(A4), 2003. doi: 10.1029/2002JA009543.
- [16] F. Honary, N. Borisov, M. Beharrell, and A. Senior. Temporal development of the magnetic zenith effect. *J. Geophys. Res.*, 116:A06309, 2011. doi: 10.1029/2010JA016029.
- [17] G.D. Thome and D.W. Blood. First observations of rf backscatter from field-aligned irregularities produced by ionospheric heating. *Radio Sci.*, 9(49001): 917–921, 1974. doi: 10.1029/RS009i011p00917.
- [18] P.A. Fialer. Field-aligned scattering from a heated region of the ionosphere - observations at hf and vhf. *Radio Sci.*, 9:923–940, 1974. doi: 10.1209/RS009i011p00923.
- [19] J.D. Hansen, G.J. Morales, L.M. Duncan, and G. Dimonte. Large scale hf-induced ionospheric modification experiments. *J. Geophys. Res.*, 97(113), 1992. doi: 10.1209/91JA02403.
- [20] N. V. Bakhmet’eva, V. N. Bubukina, Y. A. Ignat’ev, G. S. Bochkarev, V. A. Eremenko, V. V. Kol’Tsov, I. V. Krasheninnikov, and Y. N. Cherkashin. Investigation by backscatter radar of artificial irregularities produced in ionospheric plasma heating experiments. *J. of Atmos. Solar-Terr. Phys.*, 59:2257–2263, December 1997. doi: 10.1016/S1364-6826(96)00120-4.
- [21] R. S. Dhillon and T. R. Robinson. Observations of time dependence and aspect sensitivity of regions of enhanced UHF backscatter associated with rf heating. *Annales Geophysicae*, 23(1):75–85, 2005. doi: 10.5194/angeo-23-75-2005. URL <http://www.ann-geophys.net/23/75/2005/>.

- [22] G. B. Carpenter. Vhf and uhf bistatic observations of a region of the ionosphere modified by a high power radio transmitter. *Radio Science*, 9(11):965–969, 1974. ISSN 1944-799X. doi: 10.1029/RS009i011p00965. URL <http://dx.doi.org/10.1029/RS009i011p00965>.
- [23] P. B. Rao and G. D. Thome. a model for rf scattering from field-aligned heater-induced irregularities. *Radio Science*, 9(11):987–996, 1974. ISSN 1944-799X. doi: 10.1029/RS009i011p00987. URL <http://dx.doi.org/10.1029/RS009i011p00987>.
- [24] A.V. Gurevich and K.P. Zybin. Strong field aligned scattering of {UHF} radio waves in ionospheric modification. *Physics Letters A*, 358(2):159 – 165, 2006. ISSN 0375-9601. doi: <http://dx.doi.org/10.1016/j.physleta.2006.05.064>. URL <http://www.sciencedirect.com/science/article/pii/S0375960106007109>.
- [25] G. Milikh, A. Gurevich, K. Zybin, and J. Secan. Perturbations of gps signals by the ionospheric irregularities generated due to hf-heating at triple of electron gyrofrequency. *Geophysical Research Letters*, 35(22):n/a–n/a, 2008. ISSN 1944-8007. doi: 10.1029/2008GL035527. URL <http://dx.doi.org/10.1029/2008GL035527>. L22102.
- [26] P. A. Bernhardt, C. A. Selcher, R. H. Lehmberg, S. Rodriguez, J. Thomason, M. McCarrick, and G. Frazer. Determination of the electron temperature in the modified ionosphere over haarp using the hf pumped stimulated brillouin scatter (sbs) emission lines. *Annales Geophysicae*, 27(12):4409–4427, 2009. doi: 10.5194/angeo-27-4409-2009. URL <http://www.ann-geophys.net/27/4409/2009/>.
- [27] P. A. Bernhardt, C. A. Selcher, and S. Kowtha. Electron and ion bernstein waves excited in the ionosphere by high power em waves at the second harmonic of the electron cyclotron frequency. *Geophysical Research Letters*, 38(19), 2011. ISSN 1944-8007. doi: 10.1029/2011GL049390. URL <http://dx.doi.org/10.1029/2011GL049390>. L19107.
- [28] B. Thidé, H. Kopka, and P. Stubbe. Observations of stimulated scattering of a strong high-frequency radio wave in the ionosphere. *Phys. Rev. Lett.*, 49: 1561–1564, Nov 1982. doi: 10.1103/PhysRevLett.49.1561. URL <http://link.aps.org/doi/10.1103/PhysRevLett.49.1561>.
- [29] W. Pelgrum, Y. Morton, F. van Graas, S. Gunawardena, M. Bakich, D. Chermey, S. Peng, J. Triplett, A. Vermuru, and P. Vikram. Measurement and analysis of artificially generated and natural ionosphere scintillation effects on GNSS signals. *Proc. 2011 Int. Tech. Meeting of The Inst. of Nav.*, pages 950–958, 2011.
- [30] A. V. Gurevich. Nonlinear effects in the ionosphere. *Phys.-Usp.*, 50:2622–2625, June 2007. doi: 10.1070/PU2007v050n11ABEH006212.

- [31] T. D. Carozzi, B. Thid, S. M. Grach, T. B. Leyser, M. Holz, G. P. Komrakov, V. L. Frolov, and E. N. Sergeev. Stimulated electromagnetic emissions during pump frequency sweep through fourth electron cyclotron harmonic. *Journal of Geophysical Research: Space Physics*, 107(A9):SIA 5–1–SIA 5–13, 2002. ISSN 2156-2202. doi: 10.1029/2001JA005082. URL <http://dx.doi.org/10.1029/2001JA005082>. 1253.
- [32] E. Sergeev, S. Grach, A. Shindin, E. Mishin, P. Bernhardt, S. Briczinski, B. Isham, M. Broughton, J. LaBelle, and B. Watkins. Artificial ionospheric layers during pump frequency stepping near the 4th gyroharmonic at haarp. *Phys. Rev. Lett.*, 110:065002, Feb 2013. doi: 10.1103/PhysRevLett.110.065002. URL <http://link.aps.org/doi/10.1103/PhysRevLett.110.065002>.
- [33] L. Norin, S. M. Grach, T. B. Leyser, B. Thid, E. N. Sergeev, and M. Berlin. Ionospheric plasma density irregularities measured by stimulated electromagnetic emission. *Journal of Geophysical Research: Space Physics*, 113(A9):n/a–n/a, 2008. ISSN 2156-2202. doi: 10.1029/2008JA013338. URL <http://dx.doi.org/10.1029/2008JA013338>. A09314.
- [34] A.V. Gurevich, N.D. Borisov, and G.M. Milikh. *Physics of Microwave Discharge: Artificial Ionoized Regions in the Atmosphere*. Gordon and Breach, 1997.
- [35] T. Pedersen, B. Gustavsson, E. Mishin, E. Kendall, T. Mills, H. C. Carlson, and A. L. Snyder. Creation of artificial ionospheric layers using high-power hf waves. *Geophysical Research Letters*, 37(2):n/a–n/a, 2010. ISSN 1944-8007. doi: 10.1029/2009GL041895. URL <http://dx.doi.org/10.1029/2009GL041895>. L02106.
- [36] B. Eliasson, X. Shao, G. Milikh, E.V. Mishin, and K. Papadopoulos. Numerical modeling of artificial ionospheric layers driven by high-power HF heating. *J. Geophys. Res.*, 117:A10321, 2012. doi: 10.1029/2012JA018105.
- [37] P. V. Ponomarenko, T. B. Leyser, and B. Thid. New electron gyroharmonic effects in hf scatter from pump-excited magnetic field-aligned ionospheric irregularities. *J. of Geophys. Res. Space Phys.*, 104(A5):10081–10087, 1999. ISSN 2156-2202. doi: 10.1029/1999JA900039. URL <http://dx.doi.org/10.1029/1999JA900039>.
- [38] B. Thidé, E. N. Sergeev, S. M. Grach, T. B. Leyser, and T. D. Carozzi. Competition between langmuir and upper-hybrid turbulence in a high-frequency-pumped ionosphere. *Phys. Rev. Lett.*, 95:255002, Dec 2005. doi: 10.1103/PhysRevLett.95.255002. URL <http://link.aps.org/doi/10.1103/PhysRevLett.95.255002>.
- [39] L. Norin, T. B. Leyser, E. Nordblad, B. Thidé, and M. McCarrick. Unprecedentedly strong and narrow electromagnetic emissions stimulated by high-frequency

- radio waves in the ionosphere. *Phys. Rev. Lett.*, 102:065003, Feb 2009. doi: 10.1103/PhysRevLett.102.065003. URL <http://link.aps.org/doi/10.1103/PhysRevLett.102.065003>.
- [40] T. B. Leyser, B. Thidé, H. Derblom, Å. Hedberg, B. Lundborg, P. Stubbe, H. Kopka, and M. T. Rietveld. Stimulated electromagnetic emission near electron cyclotron harmonics in the ionosphere. *Phys. Rev. Lett.*, 63:1145–1147, Sep 1989. doi: 10.1103/PhysRevLett.63.1145. URL <http://link.aps.org/doi/10.1103/PhysRevLett.63.1145>.
- [41] T. B. Leyser, B. Thid, M. Waldenvik, S. Goodman, V. L. Frolov, S. M. Grach, A. N. Karashtin, G. P. Komrakov, and D. S. Kotik. Spectral structure of stimulated electromagnetic emissions between electron cyclotron harmonics. *J. of Geophys. Res.: Space Phys.*, 98(A10):17597–17606, 1993. ISSN 2156-2202. doi: 10.1029/93JA01387. URL <http://dx.doi.org/10.1029/93JA01387>.
- [42] T. B. Leyser, B. Thid, M. Waldenvik, E. Veszelei, V. L. Frolov, S. M. Grach, and G. P. Komrakov. Downshifted maximum features in stimulated electromagnetic emission spectra. *J. of Geophys. Res. Space Phys.*, 99(A10):19555–19568, 1994. ISSN 2156-2202. doi: 10.1029/94JA01399. URL <http://dx.doi.org/10.1029/94JA01399>.
- [43] J. Huang and S. P. Kuo. A theoretical model for the broad upshifted maximum in the stimulated electromagnetic emission spectrum. *J. of Geophys. Res.: Space Phys.*, 99(A10):19569–19576, 1994. ISSN 2156-2202. doi: 10.1029/94JA01261. URL <http://dx.doi.org/10.1029/94JA01261>.
- [44] A. Mahmoudian, W. A. Scales, P. A. Bernhardt, B. Isham, E. Kendall, S. J. Briczinski, N. E. B. Fuentes, and O. Vega-Cancel. Electron gyroharmonic effects on ionospheric stimulated brillouin scatter. *Geophys. Res. Lett.*, 41(16):5710–5716, 2014. ISSN 1944-8007. doi: 10.1002/2014GL061050. URL <http://dx.doi.org/10.1002/2014GL061050>.
- [45] A. Najmi, G. Milikh, J. Secan, K. Chiang, M. Psiaki, P. Bernhardt, S. Briczinski, C. Siefing, C.L. Chang, and K. Papadopoulos. Generation and detection of super small striations by F region HF heating. *J. Geophys. Res. Space Phys.*, 119:6000–6010, 2014. doi: 10.1002/2014JA020038.
- [46] A. V. Zalizovski, S. B. Kashcheyev, Y. M. Yampolski, V. G. Galushko, V. Belyey, B. Isham, M. T. Rietveld, C. La Hoz, A. Brekke, N. F. Blagoveshchenskaya, and V. A. Kornienko. Self-scattering of a powerful hf radio wave on stimulated ionospheric turbulence. *Radio Sci.*, 44(3):n/a–n/a, 2009. ISSN 1944-799X. doi: 10.1029/2008RS004111. URL <http://dx.doi.org/10.1029/2008RS004111>. RS3010.
- [47] L.M. Erukhimov, S.N. Matyugin, and V.P. Uryadov. Radio-wave propagation in an ionospheric wave channel. *Radiophys. and Quan. Elec.*, 18(9):958–963,

1975. ISSN 0033-8443. doi: 10.1007/BF01038191. URL <http://dx.doi.org/10.1007/BF01038191>.
- [48] H. E. Whitney, J. Aarons, R. S. Allen, and D. R. Seemann. Estimation of the cumulative amplitude probability distribution function of ionospheric scintillations. *Radio Sci.*, 7(12):1095–1104, 1972. ISSN 1944-799X. doi: 10.1029/RS007i012p01095. URL <http://dx.doi.org/10.1029/RS007i012p01095>.
- [49] V. Frolov, S.A. Metelev, and E.N. Sergeev. Temporal behavior of artificial small-scale ionospheric irregularities: Review of experimental results. *J. Atmos. Solar-Terr. Physics*, 59(18):2317–2333, 1997.
- [50] P.V. Kotov, E.N. Sergeev, and S.M. Grach. Spectra of stimulated electromagnetic emission of the ionosphere upon sweeping of the pump wave frequency near gyroharmonics. i. experimental results. *Radiophys. and Quan. Elec.*, 51(6):417–430, 2008. ISSN 0033-8443. doi: 10.1007/s11141-008-9043-5. URL <http://dx.doi.org/10.1007/s11141-008-9043-5>.
- [51] L. S. Wagner, P. A. Bernhardt, J. A. Goldstein, C. A. Selcher, V. L. Frolov, and E. N. Sergeev. Effect of ionospheric self-conditioning and preconditioning on the broad upshifted maximum component of stimulated electromagnetic emission. *J. of Geophys. Res. Space Phys.*, 104(A2):2573–2590, 1999. ISSN 2156-2202. doi: 10.1029/1998JA900006. URL <http://dx.doi.org/10.1029/1998JA900006>.
- [52] K. G. Budden and H. G. Martin. The ionosphere as a whispering gallery. *Proc. of the Royal Soc. of London A: Math., Phys. and Eng. Sci.*, 265(1323):554–569, 1962. ISSN 0080-4630. doi: 10.1098/rspa.1962.0042.
- [53] Hsi-Tien Chang. The waveguide mode theory of whispering-gallery propagation in the f region of the ionosphere. *Radio Science*, 6(4):475–482, 1971. ISSN 1944-799X. doi: 10.1029/RS006i004p00475. URL <http://dx.doi.org/10.1029/RS006i004p00475>.
- [54] P.B. Rao and G.D. Thome. A model for RF scattering from field-aligned heater-induced irregularities. *Radio Sci.*, 9:987–996, 1974. doi: 10.1029/RS009i011p00987.
- [55] T.L. Franz, M.C. Kelley, and A.V. Gurevich. Radar backscattering from artificial field-aligned irregularities. *Radio Science*, 34(2):465–475, Mar-Apr 1999. doi: 10.1029/1998RS900035.
- [56] T. Pedersen, B. Gustavsson, E. Mishin, E. MacKenzie, H.C. Carlson, M. Starks, and T. Mills. Optical ring formation and ionization production in high-power HF heating experiments at HAARP. *Geophys. Res. Lett.*, 36:L18107, 2009. doi: 10.1029/2009GL040047.

- [57] E. Mishin and T. Pedersen. Ionizing wave via high-power HF acceleration. *Geophys. Res. Lett.*, 38:L01105, 2011. doi: 10.1029/2010/GL046045.
- [58] A. Fukuyama, H. Momota, and R. Itatani. Stochastic acceleration by an electrostatic wave near ion cyclotron harmonics. *Phys. Rev. Lett.*, 38(13):701–704, March 1977. doi: 10.1103/PhysRevLett.38.701.
- [59] C.F.F. Karney. Stochastic ion heating by a lower hybrid wave. *Phys. Fluids*, 21:1584–1599, 1978. doi: 10.1063/1.862406.
- [60] J.M. McChesney, R. A. Stern, and P.M. Bellan. Observations of fast stochastic ion heating by drift waves. *Phys. Rev. Lett.*, 59(13):1436–1439, 1987. doi: 10.1103/PhysRevLett.59.1436.
- [61] M. Balikhin, M. Gedalin, and A. Petrukovich. New mechanism for electron heating in shocks. *Phys. Rev. Lett.*, 70(9):1259–1262, March 1993. doi: 10.1103/PhysRevLett.70.1259.
- [62] K. Stasiewicz, R. Lundin, and G. Marklund. Stochastic ion heating by orbit chaotization on electrostatic waves and nonlinear structures. *Phys. Scr.*, 84: 60–63, 2000. doi: 10.1238/Physica.Topical.084a00060.
- [63] B. Eliasson. Numerical simulations of the Fourier transformed Vlasov-Maxwell system in higher dimensions - theory and applications. *Trans. Theor. Stat. Phys.*, 39(5):387–465, 2010. doi: 10.1080/00411450.2011.563711.
- [64] N.F. Blagoveshchenskaya, T.D. Borisova, T.K. Yeoman, and M.T. Rietveld. The effects of modifications of a high-latitude ionosphere by high-power HF radio waves part1. *Radiophys. Q. Elec.*, 53(9-10):512–531, Feb 2011. doi: 10.1007/s11141-011-9247-y.
- [65] N.F. Blagoveshchenskaya, T.D. Borisova, V.A. Kornienko, M.T. Rietveld, T.K. Yeoman, D.M. Wright, M. Rother, H. Luhr, E.V. Mishin, C. Roth, V.L. Frolov, M. Parrot, and J.L. Rauch. The effects of modifications of a high-latitude ionosphere by high-power HF radio waves part2. *Radiophys. Q. Elec.*, 54(2): 89–101, Feb 2011. doi: 10.1007/s11141-011-9273-9.
- [66] D. Beeman. Some multistep methods for use in molecular dynamics calculations. *J. of Comp. Phys.*, 20(2):130 – 139, 1976. ISSN 0021-9991. doi: [http://dx.doi.org/10.1016/0021-9991\(76\)90059-0](http://dx.doi.org/10.1016/0021-9991(76)90059-0).
- [67] F.W. Crawford and J.A. Tataronis. Absolute instabilities of perpendicularly propagating cyclotron harmonic plasma waves. *J. Appl. Phys.*, 36:2930–2934, 1965. doi: 10.1063/1.1714609.
- [68] D.G. Lominadze. *Cyclotron Waves in Plasmas*. Oxford Pergamon Press, 1981.

- [69] E. Mjølhus. Theoretical model for long time stimulated electromagnetic emission generation in ionospheric radio modification experiments. *J. Geophys. Res. Space*, 103(A7):14711–14729, 1998. doi: 10.1029/98JA00927.
- [70] A.G. Litvak, V.I. Petrukhina, A.M. Sergeev, and G.M. Zhislin. Dynamics of one-dimensional upper-hybrid turbulence in a magnetized plasma. *Phys. Lett. A*, 94(2):85 – 88, 1983. doi: 10.1016/0375-9601(83)90213-X.
- [71] A. Najmi, B. Eliasson, X. Shao, G. Milikh, S. Sharma, and K. Papadopoulos. Theoretical studies of fast stochastic electron heating near the upper hybrid layer. *Submitted - Radio Science*, 2015.